A Detailed Study of the Pulsar Wind Nebula HESS J0835–455 (Vela X) in TeV γ-Rays

Detaillierte Analyse der
TeV-Gammastrahlung des Pulsarwindnebels
HESS J0835–455 (Vela X)

Der Naturwissenschaftlichen Fakultät
der Friedrich-Alexander-Universität Erlangen-Nürnberg
zur Erlangung des Doktorgrades Dr. rer. nat.

vorgelegt von
Bernhard Glück
aus Mainz

Als Dissertation genehmigt von der Naturwissenschaftlichen Fakultät der Friedrich-Alexander-Universität Erlangen-Nürnberg

Tag der mündlichen Prüfung: 24. Februar 2011

Vorsitzender der Promotionkommission:	Prof. Dr. Rainer Fink
Erstberichterstatter:	Prof. Dr. Christian Stegmann
Zweitberichterstatter:	Prof. Dr. Jörn Wilms

Abstract

Pulsar Wind Nebulae are interstellar bubbles filled with relativistic plasma and claimed to be the most frequent sources of Tera-Electron-Volts γ-ray sources in our Galaxy. HESS J0835–455 is the TeV counterpart of the Pulsar Wind Nebula Vela X first detected with a radio telescope. It has been observed with the High Energy Stereoscopic System (H.E.S.S.) from 2003 to 2009. H.E.S.S. is an array of four Imaging Atmospheric Cherenkov Telescopes, such instruments detecting the Cherenkov light which is generated in air showers induced by γ-ray photons. The Cherenkov telescope technique exhibits a high background level introduced by the air showers of charged cosmic rays. Detailed studies of the properties of the H.E.S.S. background will be presented. The influence of the atmosphere on the background rates is an extraordinary problem in the analysis of the Vela X data, as the so-called OnOff (blank sky) background model is applied. A new technique is proposed to counterbalance misestimations of the background level due to fluctuations in the optical density and refraction of the atmosphere. In this work, the results of the TeV analysis of Vela X are reported. They support a leptonic scenario for the plasma inside the Pulsar Wind Nebula.

Zusammenfassung

Pulsarwindnebel sind interstellare Volumina, die mit einem Plasma aus relativistischen Teilchen gefüllt sind. Es wird vermutet, dass sie die häufigste Quelle von Teraelektronenvolt-Gammastrahlung in unserer Galaxie sind. HESS J0835–455 ist das TeV-Pendant des ursprünglich mit einem Radioteleskop detektierten Pulsarwindnebels Vela X. Dieser wurde mit dem High Energy Stereoscopic System (H.E.S.S.) zwischen 2003 und 2009 beobachtet. H.E.S.S. ist eine Anlage aus vier abbildenden atmosphärischen Tscherenkow-Teleskopen. Solche Teleskope detektieren Tscherenkow-Licht aus Luftschauern, welche durch die Photonen der Gammastrahlung erzeugt werden. Die Messungen mit Tscherenkow-Teleskopen enthalten einen hohen Anteil an Untergrundereignissen, die durch die Luftschauer geladener kosmischer Strahlung erzeugt werden. Eine ausführliche Studie der Eigenschaften des H.E.S.S. Untergrundes wird vorgestellt. Da der Untergrund mit dem sogenannten “OnOff”-Model abgeschätzt wird, ist der Einfluss der Atmosphäre auf die Rate der Untergrundereignisse eine wichtige Aufgabenstellung der Analyse der Beobachtungsdaten von Vela X. Eine neue Methode wird vorgeschlagen, um Fehleinschätzungen der Untergrundrate auf Grund von atmosphärischen Schwankungen in der optischen Dichte und Lichtbrechung auszugleichen. Die Ergebnisse der TeV-Datenanalyse für Vela X werden vorgestellt. Diese unterstützen die Interpretation, dass sich das Plasma des Pulsarwindnebels aus Elektronen und Positronen zusammensetzt.

Contents

List of Figures

List of Tables

Chapter 1

Introduction

The High Energy Spectroscopic System (H.E.S.S.) experiment is both a particle detector and an astronomical observatory for γ-rays in the energy range between 100 GeV and 100 TeV. H.E.S.S. is running four Cherenkov telescopes. Together with the atmosphere, the telescopes are calorimeters for single highly energetic particles reaching the Earth's atmosphere from outer space. The atmosphere is part of the detector as it provides the target material for the primary highly energetic particles to deposit their energy in air shower cascades of secondary particles. The telescopes collect Cherenkov light emitted by the atmospheric medium polarized by charged shower particles in about 1000 spatially resolved channels per telescope. Each channel covers a distinct solid angle on the sky, so that a reconstruction of the shower development and the type of the primary particle can be applied. From the astronomical point of view, the main task of the H.E.S.S. telescopes is to observe γ-rays from astronomical objects. The reason why the astronomical observations are restricted to γ-rays is that charged particles accelerated somewhere in an object of our Galaxy or even somewhere beyond in the Universe are deflected by magnetic fields so that they cannot be traced back to their origin.

Figure 1.1: The photograph shows one of the H.E.S.S. telescopes with its mirrors mounted on the support structure and its imaging light detector holded by four arms.

At the moment, the organization of experiments using Cherenkov telescopes is in transition from closed experiments in astro-particle physics to astronomical observatories. While at the time of construction of the H.E.S.S. experiment about a dozen TeV γ-ray sources were known, the understanding of the detector and the systematics of the measured γ-ray flux was an outstanding challenge. As of today, recent experiments have discovered almost 100 sources and the data taking process as well as most of the analysis of data

from Cherenkov telescopes are handled with standard procedures. On the other hand, the rating of the TeV signal in a context of the whole wavelength spectrum (radio, IR, optical, UV, X-rays and GeV γ-rays) has evolved to be one of the key aspects of many recent publications by the groups of Cherenkov telescopes experiments.

This work resides at the transition between both fields. The main background for the H.E.S.S. telescopes is generated by charged cosmic rays. Systematic studies on the Cherenkov light profiles of these background events are performed to improve the background subtraction from the γ-ray signal. In particular, the influence of varying atmospheric conditions on the background rates is determined and a standard analysis frame work for H.E.S.S. data is adapted to correct this influence. The astronomical task of this thesis is the analysis of the TeV γ-ray data from Vela X which is part of a group of astronomical objects in the western part of the constellation Vela. The group is associated with an ancient supernova event. This Chapter will start with a presentation of the Vela supernova objects. A general introduction to pulsar wind nebulae and the interpretation of Vela X as a pulsar wind nebula are given in Sections 1.2 and 1.3. A summary of the open questions connected to the TeV emission of Vela X can be found in Section 1.4.

A standard approach, first suggested by A. M. Hillas, is applied to reconstruct the γ-ray events. In Chapter 2 and 3, the H.E.S.S. experiment, the quality requirements on observational data and the analysis technique are introduced. As mentioned before, the flux of cosmic rays consisting mainly of protons produces events in the Cherenkov telescopes that are similar to γ-rays. The available data set for Vela X taken with the H.E.S.S. telescopes does not allow to apply the common strategies to extract the amount of background form the same observational data. As an alternative the OnOff background model[1] will be used. The OnOff model requires a good comprehension of the monitoriable but uncontrollable atmospheric conditions as part of the γ-ray detector. Systematic studies concerning the influence of atmospheric conditions on the background were performed and are presented in Chapter 4. Technical tools to handle and present the γ-ray flux after the subtraction of the background are discussed in Chapter 5. The final analysis results for the TeV γ-ray source Vela X follow in Chapter 6.

[1] In the data analysis of satellite missions, the OnOff approach is called blank sky background.

1.1 Overview of the Vela Field of View

A popular theory of the origin of the γ-rays from Vela X is, that a wind of particles is accelerated by the central pulsar and is injected as a shocked plasma (usually assumed to consist of electrons and positrons[2]) into an interstellar bubble. The energy driving this wind arises from the braking of the rotational motion of the pulsar. The plasma-filled interstellar bubble is a relatively new concept, while the term appellation "nebula" originates from a descriptive view of the observations of these objects. Vela X is extended in the order of several degrees which means that current instruments can spatially resolve Vela X. This work will start with an overview of observations of Vela X and the whole supernova remnant that is associated with the Vela Pulsar.

Figure 1.2 shows a photon flux map of γ-rays above 750 GeV. The map is based on the complete H.E.S.S. data set on the TeV source Vela X and some additional observations pointed to positions in the east. The data analysis was restricted to a field of view with a radius of 2°, which is much smaller than the extension of the map. A detailed description of how this map will be given in Section 5.3. The map contains two bright and extended sources. The pulsar wind nebula (PWN) Vela X is the western object on the right side of the map. Here, a quick view based on the flux map will give a first description on the morphology of Vela X. In the later discussion of the analysis results (Chapter 6), more accurate approaches to evaluate the morphological structure of Vela X will be presented. The flux estimate for Vela X yields a size that is larger than 1° in radius, where its center is at RA = $08^h35^m00^s$, Dec = $-45°36'00''$ (J2000). Using the commonly accepted distance estimate for the pulsar (PSR B0833-45) of 287 pc (see Sec. 1.3 or [39]), the radius corresponds to > 5 pc. Based on the proposed color scale a main emission region in the green flux range can be identified featuring a flux level of $\sim 10 \cdot 10^{-12}$ cm^{-2}s^{-1}deg^{-2}, while in the middle of Vela X along an axis in north-south direction a maximum flux above $\sim 15 \cdot 10^{-12}$ cm^{-2}s^{-1}deg^{-2} (yellow to red) is measured. Even though a discovery of such a TeV substructure can hardly be claimed given statistical uncertainties (see Sec. 6.4), at the same location a feature can be found in X-rays and radio data. A second noticeable issue is a ring of slightly shimmering γ-rays flux in the order of $2 \cdot 10^{-12}$ cm^{-2}s^{-1}deg^{-2} (dark gray) around Vela X. As this flux level is superimposed by fluctuations of the flux estimate, the shimmering flux is only identifiable by the absence of negative flux (light gray). The emission from this ring extension is examined in Section 6.2. The second source on the sky map is the supernova remnant (SNR) Vela Junior. The H.E.S.S. data taken directly on Vela Junior has been discussed in detail together with a comparison with radio and X-ray observations in Reference [10]. The three-dimensional morphology of the source can be modeled by a sphere, which is projected to our two-dimensional view of the sky. The thickness of the sphere's edge is estimated to be 22.5 % of the SNR's radius which can be

[2]In this work, positrons will not be treated separately, whenever the plasma of PWNe is described. Instead either only electrons are mentioned or the plasma is named leptonic, although muons and taus are not claimed to be part of such a leptonic plasma. The same inexactness also applies to the description of air showers in the atmosphere.

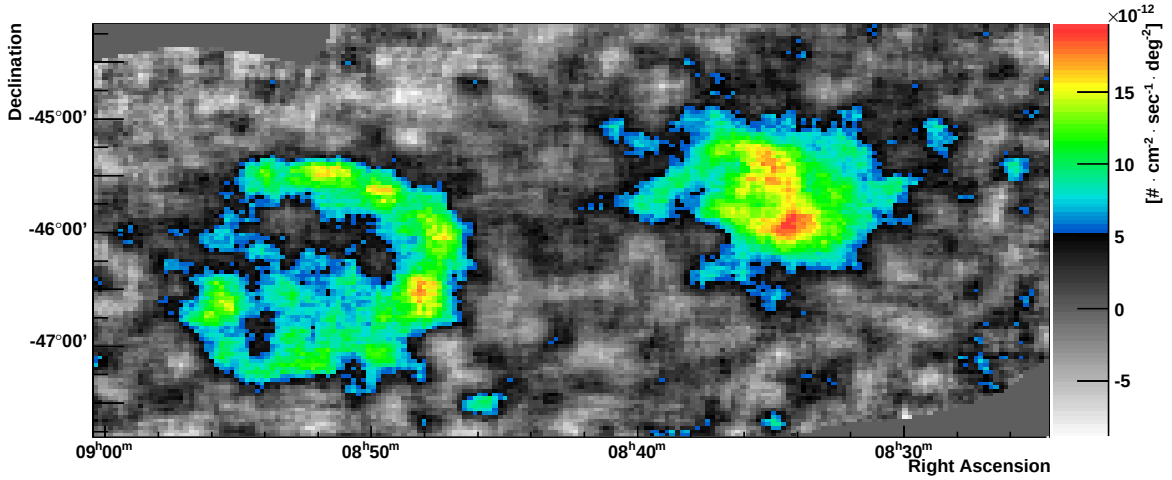

Figure 1.2: The sky map shows the γ-ray photon flux as surface flux above 0.75 TeV in the Region of Vela X and Vela Junior. A detailed discussion on this map can be found in Section 5.3.

also seen in the TeV flux map (Fig. 1.2). In the discussion in Reference [10], the distance of Vela Junior remains unclear. The given range is 200 pc to 2 kpc.

Figure 1.3 includes two count maps from the ROSAT satellite[3]. A third overview map illustrates the different objects which are discussed here (Fig. 1.3(b)). The sky maps are separated in the X-ray energy at 1.3 keV (Fig. 1.3(a) below 1.3 keV and Fig. 1.3(c) above 1.3 keV). This energy separation was established to claim the detection of Vela Junior (RX J0852.0–4622) [17]. The high-energy map is supposed to contain almost no thermal emission from the Vela SNR, so that further objects can be easily seen. These sources are the Vela pulsar in the center of the map, another SNR Puppis A in the north-west of the Vela SNR and two further point sources 1.5 deg in the north of the Vela Pulsar. A detailed discussion of the pulsar will be given in Section 1.3. Here, it should be pointed out that the pulsar is located in the north of the nebula rather than in its center. A discussion of the nebula's displacement can be found in Section 1.3.1. The most important object for the further discussion is the so-called jet-like X-ray feature. Starting outwards from the pulsar's position a feature propagates 0.75° in southern direction. In their discovery publication [87], C. B. Markwardt and H. Ögelman have interpreted the feature as a jet which fills a "Cocoon" around the jet and its head. At the position of the feature the putative TeV substructure in the middle of Vela X mentioned before is located. Also at the same position, an elongated feature is found in the radio data (see below, Fig. 1.4(b)). A short review on the nature of this jet-like X-ray feature will be given in Section 1.3.2. An additional property of the > 1.3 keV map is a background excess in the region defined by the gray box in Figure 1.3(b). The background might stem from the Vela SNR, although its origin will not be investigated in this thesis. The great structure in the low-energy map (Fig. 1.3(a)) filling the whole region is the supernova remnant (Vela SNR) ascribed

[3] http://www.mpe.mpg.de/xray/wave/rosat/index.php

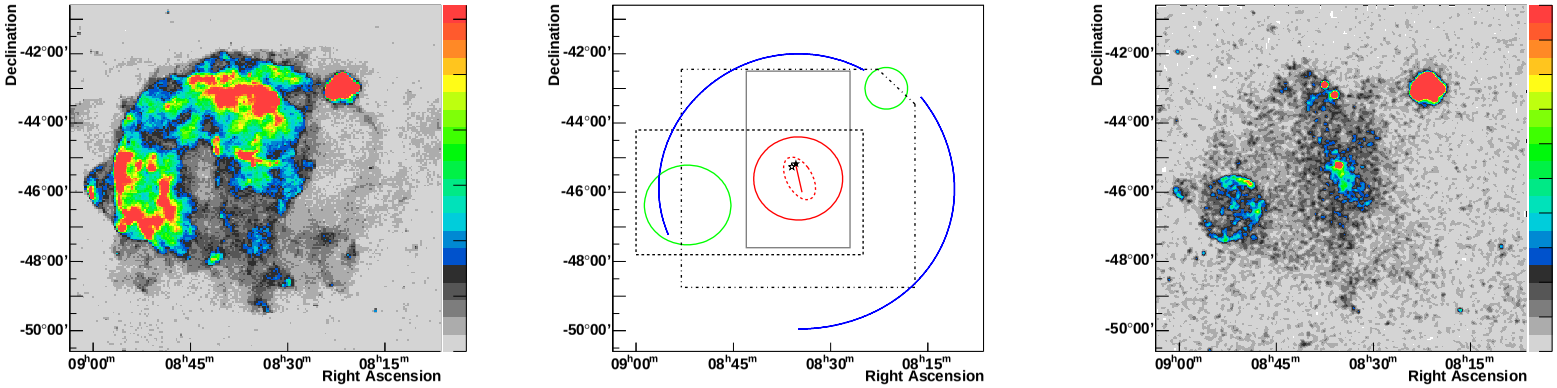

(a) < 1.3 keV (b) overview map (c) > 1.3 keV

Figure 1.3: The sky maps a) and c) show X-rays above and below 1.3 keV observed with the ROSAT satellite. The equivalent maps were presented in [17]. b) In the overview map, the Vela Pulsar is marked as filled star, the direction of the jet-like feature (see text) as a red line, the X-ray "Cocoon" around the feature as red broken line, the PWN Vela X as a red circle (radius 1.2°), the SNRs Vela Junior and Puppis A as green circles and the edge of the Vela SNR as blue segments. The gray box shows a region with enhanced X-ray level in the range of > 1.3 keV. The dashed black box indicates the sector where the TeV flux is shown in Figure 1.2 and the dash-dotted black box defines the perimeter of the radio map in Figure 1.4(a). The open star gives the estimated birth position of the Vela Pulsar under the assumption the Vela supernova explosion took place 11 ka ago (see Section 1.3).

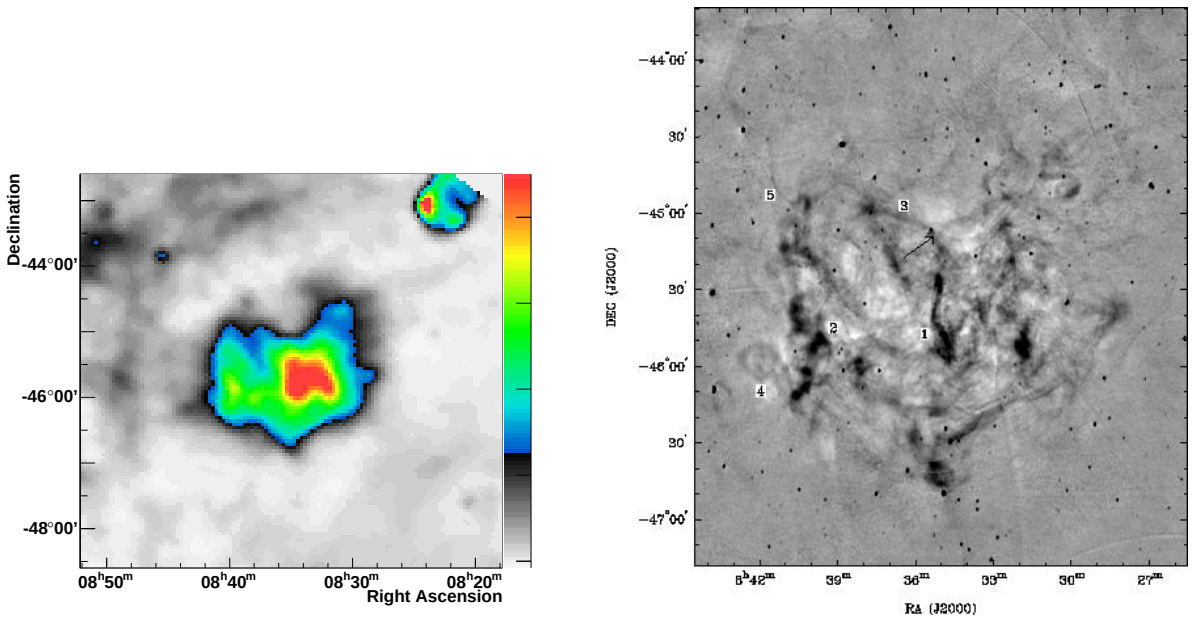

(a) Vela X at 2.4 GHz (b) Vela X at 843 MHz

Figure 1.4: a) The sky map includes a radio measurement of Vela X at 2.4 GHz. The sky map was generated from data of a scan of the southern galactic plane [45]. b) The high-resolution radio observation at 843 MHz was performed with MOST. A network of filaments distributed over Vela X can be seen. The sky map has been taken from [29].

to the same supernova explosion which also created the Vela Pulsar. The argument for this association was given by B. Aschenbach et al. [18]: Beyond the SNR several bow-shape fragments can be identified and their arrangement points towards the pulsar birth position. The Vela SNR does not fill a complete ring of 360° like Vela Junior does. An explanation for the asymmetry is that the interstellar medium (ISM) is more dense in the north-eastern parts of the SNR and thinner in the south-east. The edge of the Vela SNR is indicated in the sketch by blue circle arcs. The northern arc starting at the position of Vela Junior and ending at Puppis A has a radius of 3.75° (18.8 pc) around the pulsar position. It is quite hard to recognize the second arc in the west and south of the SNR. The arc radius was determined to be 4.2° (21.0 pc) by integrating the X-ray counts within an oversampling radius of $r_o = 0.07°$ at each position in the map. A further discussion regarding the implications of the asymmetry for the included PWN Vela X can be found in Section 1.3.1.

Vela X was originally discovered in 1958 as one of three radio signals by H. Rishbeth [98]. Rishbeth already guessed that Vela X stands out in comparison to the other two objects (Vela Y, Vela Z), as its radio spectrum tends to be more flat. In the last 50 years, several radio measurement on Vela X were performed – a list can be found in Reference [15]. The radio data from a scan of the galactic plane with the Parkes telescope at 2.4 GHz will be compared to the TeV flux later (Sec. 6.4.4). The essential sectors of the scan

data around Vela X are shown in Figure 1.4(a). The size of Vela X in radio is in the same order as in the TeV map. That is an important result presented in this work, as the former interpretations of the TeV morphology associated the TeV nebula with the X-ray jet and a surrounding "Cocoon" [6]. The second radio map in Figure 1.4(b) was obtained in a long term campaign of the Vela SNR region with the Molonglo Observatory Synthesis Telescope (MOST) at 843 MHz [29]. Regarding the energy flux contained in the whole photon spectrum (Fig. 1.9 and Sec. 1.3.3), the expected flux from the PWN Vela X at 843 MHz is small. Instead of a signal from the nebula, the Vela X region is filled with a network of filaments of a length up to 1°. The width of the filaments is found to be smaller than 0.2°. Again, a strong filament can be seen in the middle of Vela X at the position of the X-ray feature, suggesting that the filament might be related.

1.2 From a Supernova to a Pulsar Wind Nebula

The pulsars which are the power sources of pulsar wind nebulae are the compact cores remaining in the center[4] after stars exploded in supernovae. A short introduction to supernovae and their remnant shells will be presented first, before the mechanism of pulsars and pulsar winds are discussed. The Section ends with an overview of the particle processes within pulsar wind nebulae that will emit the TeV γ-rays detected by the IACTs.

In the evolution of a star the energy seen as the star light arises from nuclear fusion of light elements to heavier ones. The daughter nuclides of the fusion processes arrange themselves within the star according to their atomic mass. On the surface of the star, the unprocessed hydrogen can be found, followed towards the center by helium, carbon, nitrogen, oxygen and silicon. The heaviest product of the fusion processes, iron, is collected in a central core. As iron is the most stable element, it cannot release further energy in fusion processes. When the iron core accumulates more mass and thus eventually the radiation pressure is no longer strong enough to counter the gravitation, the core will collapse to a compact object within a time scale of milliseconds. In a simplified view, it can be assumed that protons and electrons are converted into neutrons and neutrinos. The neutrinos escape from the core and the energy gained in the core collapse explosion blows away the outer shells around the collapsing core. As the remaining compact object might consist mainly of neutrons which can be packed very densely, the object is called a neutron star. Historically, these neutron stars were observed via periodic radio pulses. Today's common belief is that these pulsars can be explained by the theoretical concept of neutron stars.

A lower and an upper bound for the mass of the stars that eventually can end up as a neutron star can be set as follows. If the mass of the progenitor star is lower than 4 solar masses ($M_\odot$), the gravitational potential is not strong enough to force the electrons and protons forming neutron and neutrinos – in the simplified view – and the star will

[4] A possible birth kick of the core will be discussed in Section 1.3.

collapse into a white dwarf without exploding in a supernova. The cores of progenitor stars with masses above 10 $M_\odot$ are supposed to collapse to black holes. Commonly, the mass of neutron stars is given between 1.3 to 1.4 $M_\odot$ (e.g. Fig. 15.19 in [82]).

1.2.1 The Evolutionary Phases of a Supernova Remnant

The shell-type supernova remnant (SNR) is formed out of the ejected material of the progenitor star and its explosion is driven by the pressure released in the core collapse. The explosion is expected to be almost symmetric and to release a kinetic energy of typically $E_{SNR} = 10^{51}$ erg. The evolution of the shell (formally the radius of the shell R) is determined by the released amount of mass M_0, the total energy E_{SNR} (respectively the outflow velocity v_0) and the density of the interstellar medium (ISM) ρ_0. A schematic system for the development of SNRs can be found e.g. in Reference [104]:

Free expansion In the first phase the swept-up mass of the ISM is small against the original mass of shell from the progenitor star. This allows the SNR to expand freely into the ISM. The transition to the next phase (called Sedov-Taylor phase), occurs when the expanding shell reaches a radius that defines a sphere including the same mass as the initial shell:

$$M_0 = \frac{4\pi}{3} \cdot \rho_0 \cdot R \tag{1.1}$$

Sedov-Taylor phase The second phase is defined under the presumption that the radiation losses of the shell are negligible. Hence, the integrated kinetic energy is conserved, but distributed over a larger amount of swept-up mass, so that the expansion velocity of the shell decreases. A typical value for the expansion velocity is several 10^5 m/s. The transition to the next phase is reached when half of the initial energy was lost through radiation processes:

$$\frac{1}{2} E_{SNR} = \int_0^t \left(\frac{\mathrm{d}E}{\mathrm{dt}} \right)_{rad} \cdot \mathrm{dt} \tag{1.2}$$

Snowplow stage The mass of the swept-up material increases, so that the shock velocity decreases and the energy losses by radiative cooling have taken away a relevant fraction of the initial energy of the particles and therefore also a significant fraction of the total kinetic energy of the shell. The end of the snowplow stage is achieved when the velocity of the SNR shell falls to the level of typical ISM velocities at 10^4 m/s.

Beside the time evolution of the SNR, the spherical composition around the central pulsar of the SNR and the PWN inside is illustrated in Figure 1.5. The image shows the SNR in the stage of free expansion. The boundaries of the shell-type SNR are defined

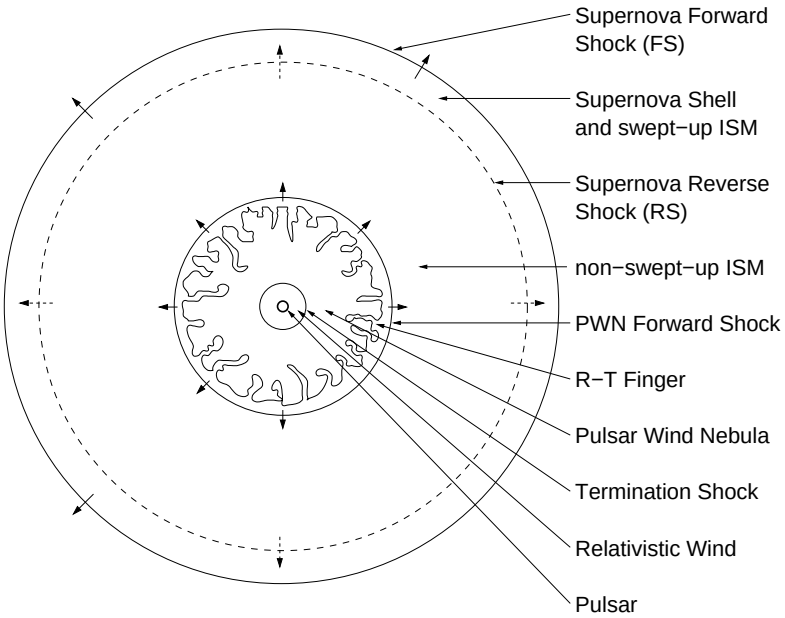

Figure 1.5: The sketch shows free expanding PWN into the cleared space within the shell of a SNR. The surface of the PWN is crowded with grown fingers of Rayleigh-Taylor instabilities. A homogeneous ISM enables a symmetric expansion of the SNR blast wave. The outer rings are the forward and reverse shock of the SNR blast wave, that carries away most of the mass of the progenitor star and the ISM of the passed volume. The SNR is in the stage of free expansion. The sketch was adapted from [68].

by the forward shock (FS) and the reverse shock (RS), with the accelerated swept-up material and initial shell material from the exploded star is accumulated in between both. The interior inside of the shell is cool, neutral ISM, which was not pushed by the shock. In the center of the SNR, the pulsar, the pulsar wind and the nebula are located. When the SNR enters the Sedov-Taylor phase, the deceleration of the FS by the swept-up mass becomes relevant. If pressure equilibrium is assumed between the initial shell material from the progenitor star and the swept-up mass from the ISM, the RS (inner boundary of the shell) moves inwards relative to the movement of the FS [90]. This expansion becomes so strong that the RS will change its direction and returns to the center of the SNR. For the particular scenario of Vela X, the return of the RS and its interaction with the PWN is an important argument in the interpretation of Vela X.

1.2.2 The Pulsar Wind and the Pulsar Wind Nebula

The energy which is required to power a PWN originates from the spin-down of a central pulsar included in the PWN bubble. In the following, the process of injecting plasma into the nebula at a termination shock of a relativistic wind is sketched. The discussion starts with the mechanics of the pulsar's spin.

The Mechanics of the Pulsar

Radio pulsars are astronomical objects from which a periodical radio signal is observed. The pulsars are supposed to be the remaining cores of core collapse supernova explosions. The periods of known pulsars range from ∼10 ms to ∼10 s. Beside the period P of the pulsar, for some objects also the first and second temporal derivatives ($\dot{P}$, respectively $\ddot{P}$) of the period are observable. That is, a slowdown mechanism takes effect on the pulsar. Hence, the fastest rotation, respectively the lowest period P_0, is found at the time of birth. To describe the deceleration of the pulsar rotation, a braking index n is defined as:

$$\dot{\Omega} = -K \cdot \Omega^n \tag{1.3}$$

where the period is replaced by the angular velocity $\Omega = 2\pi/P$ and K is a constant. The second derivative of the angular velocity is:

$$\ddot{\Omega} = -n \cdot K \cdot \Omega^{(n-1)} \cdot \dot{\Omega} \tag{1.4}$$

The quotient of the first and second derivative can be solved for the braking index:

$$n = \frac{\Omega \cdot \ddot{\Omega}}{\dot{\Omega}^2} \tag{1.5}$$

A nice example for the measurement of the braking is the Crab pulsar (also known as PSR B0531+21). The Crab PWN together with the pulsar is a very popular source. The reasons are that the signal of both the pulsar and of the pulsar wind is strong over a wide range of wavelengths (from radio to TeV) and that the date of the supernova is very well known from several observation around the world in the year 1054 [34]. In 1987 an angular velocity of $\Omega = 188.5\ \mathrm{s}^{-1}$ ($P = 33.3$ ms), $\dot{\Omega} = 2.381 \cdot 10^{-9}\ \mathrm{s}^{-2}$ and $\ddot{\Omega} = 7.591 \cdot 10^{-20}\ \mathrm{s}^{-3}$ has been measured for the Crab pulsar [85]. This results in a braking index of $n = 2.524$.

For many pulsars the real age is unknown. However, a measurement of the braking index should allow to estimate the age. This can be achieved by integrating Eqn. 1.3:

$$\int_{t_0}^{t} \mathrm{dt} = -\frac{1}{K} \cdot \int_{\Omega_0}^{\Omega} \frac{1}{\Omega^{-n}}\ \mathrm{d}\Omega \tag{1.6}$$

The result is:

$$t - t_0 = \frac{1}{K \cdot (n-1)} \cdot \left(\Omega^{-n+1} - \Omega_0^{-n+1}\right) \tag{1.7}$$

If one assumes that the initial angular velocity Ω_0 was much larger than the current angular velocity Ω, the relation for the time of birth is simplified. The resulting estimate of the age of the pulsar is called characteristic age τ. With Eqn. 1.3 one gets:

$$\tau = -\frac{\Omega}{(n-1) \cdot \dot{\Omega}} \tag{1.8}$$

Using the measurement given above, the characteristic age of the Crab is ∼1700 a. Often, the characteristic age is derived with a braking index of $n = 3$ (magnetic dipole radiation, see below) regardless of the actual measured braking. Assuming a braking index of $n = 3$ for the Crab pulsar the characteristic age yields ∼1200 a.

Energy Outflow as Magnetic Flux

Electromagnetic radiation of the pulsar a mechanism for the spin-down process is suggested. If the pulsar possesses a magnetic moment which is not aligned parallel to the pulsar's spin, a magnetic energy flux proportional to the square of the perpendicular component B_r^2 of the pulsar's magnetic field can explain the spin-down of the pulsar (see e.g. [94]). Let α be the angle between the magnetic moment and the spin axis, R_0 the radius of the neutron star and B_0 the field strength at the poles of the magnetic dipole. The far-field expansion of the radial component expressed in polar coordinates of the magnetic dipole is (radial coordinate r, polar angle to the spin axis θ, pulsar at the origin):

$$B_r = \frac{1}{r^2} \cdot \frac{\Omega}{c} \cdot R_0^3 \cdot B_0 \cdot \sin\alpha \cdot \sin\theta \cdot \sin\left(\omega\left(\frac{r}{c} - t\right) + \phi\right) \tag{1.9}$$

From this far-field expansion, we see that the strongest magnetic flux can be found in the equatorial plane of the pulsar's rotation. The flux beyond the plane is suppressed with the square of the sine of the polar angle. Expressing the magnetic dipole moment as $p_\perp$ perpendicular to the rotation axis, i.e. assuming a homogeneous magnetization of an ideal sphere is assumed, the pulsar radiate with the power:

$$\frac{\mathrm{d}E_m}{\mathrm{dt}} = \frac{\mu_0 \cdot \Omega^4 \cdot p_\perp^2}{6\pi \cdot c^3} \tag{1.10}$$

If it is assumed that all of the energy released by the spin-down of the rotation goes completely into magnetic dipole radiation, the energy balance for the pulsar reads:

$$\frac{\mathrm{d}E_r}{\mathrm{dt}} = \frac{\mathrm{d}E_m}{\mathrm{dt}} \tag{1.11}$$

which yields:

$$I \cdot \Omega \cdot \dot{\Omega} = \frac{\mu_0 \cdot \Omega^4 \cdot p_\perp^2}{6\pi \cdot c^3} \tag{1.12}$$

where I is the moment of inertia of the pulsar. For the magnetic dipole a braking index of $n = 3$ can be extracted from the last equation. If one assumes a mass of 1.4 $M_\odot$ to be distributed within a homogeneous sphere and given that the radius of pulsars is about 10 km, the moment of inertia amounts to $1.1 \cdot 10^{38}$ kg m^2. A standard value for the initial period of a pulsar is 20 ms, so that the initial rotation energy is $E_0 = 5.5 \cdot 10^{49}$ erg.

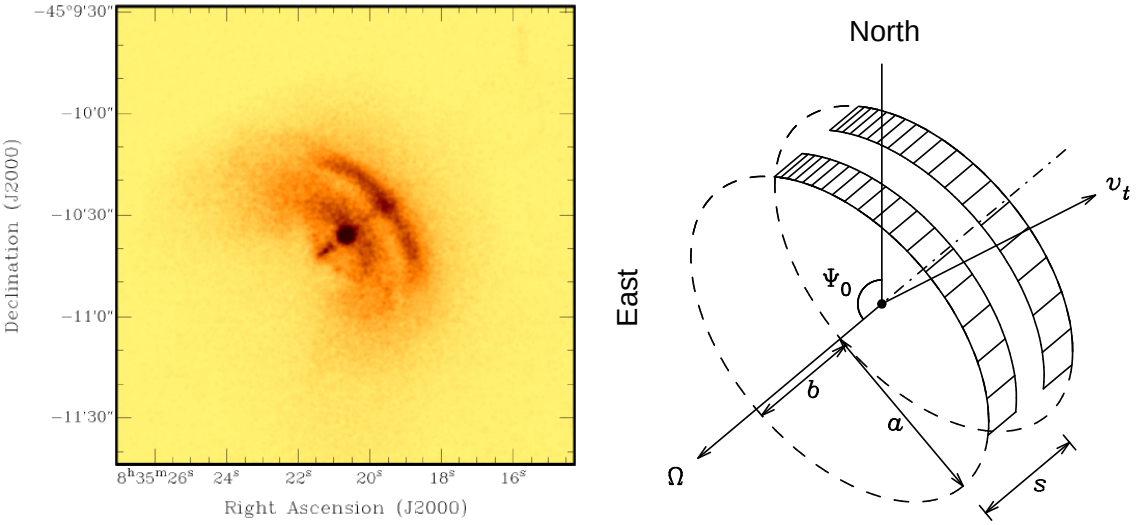

(a) termination shock of the relativistic wind (b) model for the double torii

Figure 1.6: a) The X-ray sky map shows a high-resolution image of the point-like Vela Pulsar and the synchrotron emission from the wind's termination shock, generating a double torii structure. b) A model to align the double torii in the high-resolution image is sketched in the diagram. Both figures are taken from [58].

The Relativistic Pulsar Wind

The remaining transport mechanism from the pulsar to the pulsar wind nebula is one of today's open problems (e.g. [50] and references therein). To sum up the discussion, it is generally accepted that there is a relativistic wind outgoing from the pulsar that carries away the spin-down power. It is unclear, however, if the energy flux is realized as magnetic flux or as kinetic energy of wind particles. One relevant parameter is the magnetization σ which is defined as the ratio of Poynting flux and kinetic flux:

$$\sigma = \frac{B^2}{4\pi} \cdot \frac{1}{\rho \cdot \Gamma \cdot c^2} \tag{1.13}$$

where ρ is the particle area density of the wind and Γ is the Lorentz factor of the particles in the wind. Assuming that there is nothing disrupting the wind beyond its creation by the pulsar, the magnetization parameter should be constant as both B^2 and ρ are expected to decrease with the square of the distance to the pulsar [16]. That is, the magnetization σ is conserved while the wind propagates away from the pulsar. An estimation of σ can be done as follows. The velocity of the wind particles is relatively low as there is no synchrotron emission detected from the wind directly beyond the pulsar. On the other hand, the magnetic field strength is comparatively large near the surface of the pulsar, so that the magnetization in the propagating wind is assumed to be large ($\sigma \gg 1$).

The Wind's Termination Shock

In a certain distance from the pulsar a termination of the wind can be observed as a compact synchrotron nebula. This termination shock releases high-energy particles into the surrounding nebula. The magnetic field strength in the PWN is estimated to be in the order of some μG while a highly energized plasma is present in the nebula, so that the magnetization downstream the termination shock is small ($\sigma \ll 1$). For the Vela Pulsar a compact synchrotron nebula was detected in the early 1970s with the UHURU satellite[5] [70]. Meanwhile a high-resolution sky map has been published with the data from the Chandra mission[6]. In the Chandra image (see Fig. 1.6), the compact nebula is resolved into the pulsar, a jet with a counter-jet and a double torii structure. The torii are located in the equatorial plane of the pulsar rotation which is in agreement with the preference of the magnetic energy flux in this plane. The radius of the torii is about 0.006° (0.03 pc) around the pulsar. Helfand et al. argue that the termination shock is located at the position where the upstream pressure in the wind is in equilibrium with the pressure of the outflowing nebula plasma, which infers a magnetization of $\sigma \approx 1$.

An acceleration process for particles at the termination shock is proposed as follows. Particles from the wind which have passed the shock from the upstream to the downstream area can be elastically scattered (conserving their kinetic energy) and reach the upstream area again. The backscattered particles are then accelerated to the upstream bulk velocity β_w in their motion component parallel to the wind. Each time a particle completes such a cycle, it gains an amount ΔE of energy. The mean probability for the particles to engage a further cycle after completing a cycle is P_r (the escape probability is $1 - P_r$) and the spectral particle density of the escaping plasma is a power law (e.g. see [2, 19]):

$$\frac{\mathrm{d}N_p}{\mathrm{dE}} \quad \propto \quad E^{-\alpha} \tag{1.14}$$

The power-law index α is given by P_r and the mean relative energy gain of all passed cycles (Eqn. 1 of [2]), in which E_c is the initial particle energy of a single cycle:

$$\alpha \quad = \quad 1 + \frac{\ln\left(1/P_r\right)}{\ln\left\langle 1 + \Delta E/E_c \right\rangle_c} \tag{1.15}$$

In case of an ideal non-relativistic gas with an adiabatic constant of $\frac{5}{3}$ (ratio of the specific heats), an index of $\alpha = 2$ is found. For relativistic shocks, the values of the index range between $\alpha = 2.2$ and $\alpha = 2.3$. Achterberg et al. [2] for example obtained $\alpha = 2.23$ ($1 + \Delta E/E_c = 1.97$, $P_r = 0.44$) from a semi-analytical approach for the case that particles are scattered on both sides of the shock and $\alpha = 2.31$ ($1 + \Delta E/E_c = 1.65$, $P_r = 0.52$), if the particles are deflected by the magnetic field in the upstream region. In the PWN, the bulk velocity of the upstream plasma at the termination shock is assumed to be relativistic while there is no relativistic motion of the shock front or the nebula relative to us seen in

[5] http://heasarc.gsfc.nasa.gov/docs/uhuru/uhuru.html

[6] see http://www.nasa.gov/mission_pages/chandra/main/index.html or Reference [103]

the observations of the torii structure. Although the downstream particles in the nebula's plasma are relativistic, the downstream bulk velocity is non relativistic.

In the discussion below, the power law (Eqn. 1.14) with an index of $\alpha = 2.0$ will be used as plasma injection spectrum in the nebula. For an explanation of radio and MeV/GeV signals from PWNe observations, a second more descriptive power-law component is introduced (e.g. [38, 106]). A. Spitkovsky has proposed, based on long-term particle-in-cell simulations, that the second component follows a Maxwellian shape and the high-energy component is a power-law tail of the Maxwellian [100].

1.2.3 The Evolutionary Phases of a Pulsar Wind Nebula

Similar to the classification of the SNR shell development, different phases in the development of the PWN can be found. There are several models for the evolution of PWN (see e.g. [95, 97] and Section 1.3.3). Here, the argumentation will follow the recent semi-analytical description presented in [51]. In the first phase, the nebula expands freely into the cleared interior of the SNR, as the pressure inside the nebula is large against the counter-pressure of the interior medium. Consequently, this phase is usually referred as the "free expansion phase", similar to the first phase of the shell-type SNR. One should be careful to avoid mixing up both terms. The second phase starts when the PWN strikes the reverse shock of the SNR. Typical time scales for the return of the RS to the PWN are some thousand years. After the collision, the reverse shock will compress the PWN, while inside the PWN a strong pressure arises from the ongoing injection of the shocked pulsar wind plasma into the nebula. Caused by the compression, the magnetic field strength inside the PWN increases from some μG to several hundred μG, so that the synchrotron luminosity from the nebula plasma is also increased. As a consequence the pressure within the PWN will accelerate the PWN outwards against the RS and the PWN will expand. In the further evolution of the PWN additional phases of reexpansion and compression can follow. Depending on the initial conditions used in the model, especially the pulsar's proper motion, the pulsar will leave the original ("relic") PWN and start a new PWN.

1.2.4 Rayleigh-Taylor Instabilities

In the high-resolution radio image of the Vela X nebula (Fig. 1.4(b)) a group of longitudinal filaments is visible. One suggested explanation for their origin is that the filaments have grown out of perturbations at the interface between the PWN and the cold ISM inside the supernova shell (free expansion phase), respectively the reverse shock. A well-arranged review on Rayleigh-Taylor (RT) instabilities in magnetic fluids is given in [69]. The RT instabilities can develop, if a thin medium is accelerated against a thicker one. For a wave-like perturbation with the wavelength λ, the fraction of growing instabilities n can

be derived analytically to (e.g. [69]):

$$n^2 = g \cdot \frac{2\pi}{\lambda} \cdot \frac{\rho_2 - \rho_1}{\rho_2 + \rho_1} - \frac{2\pi}{\lambda} \cdot \frac{B^2 \cdot \cos^2\theta}{\rho_2 + \rho_1} \tag{1.16}$$

where ρ_1 is the density of the thin nebula plasma and ρ_2 the density of the thicker SNR shell medium behind the reverse shock. The constant g is named "effective gravitation constant" in analogy to two fluids in a gravitational field. g is determined by the pressure gradient between the PWN and the RS. B is the magnetic field strength in the PWN next to the interface and θ is the angle between the magnetic field lines and the direction of the perturbation on the interface. If a magnetic field component tangential to the surface exists, the field will preserve small perturbations to grow. A minimum wavelength of λ_C for instabilities can be derived from Eqn. 1.16 with $n = 0$:

$$\lambda_C = \frac{B^2 \cdot \cos^2\theta}{g \cdot (\rho_2 - \rho_1)} \tag{1.17}$$

The perturbation length with the highest probability for the growth of RT instabilities is ($\mathrm{d}n/\mathrm{d}\lambda = 0$):

$$\lambda_{max} = 2 \cdot \frac{B^2 \cdot \cos^2\theta}{g \cdot (\rho_2 - \rho_1)} = 2 \cdot \lambda_C \tag{1.18}$$

J. Gelfand, P. Slane and W. Zhang gave a recent model for the development of PWN in interaction with the RS [51]. They argued that the conditions for the growth of RT instabilities are fulfilled in the first parts of the PWNe free expansion phase and in the reexpansion phase after the RS has returned.

1.2.5 Teraelectronvolt γ-Rays from a Leptonic Plasma

In Figure 1.2, the particle flux of the γ-ray events with energies between 750 GeV and 65 TeV from the PWN Vela X are presented. To reach such high energies, acceleration processes for single particles are required. As discussed previously, the termination shock of the relativistic pulsar wind releases highly accelerated electrons into the nebula. The TeV photons from the PWN Vela X are supposed to be generated from seed photons that are upscattered by these highly energetic electrons in an Inverse Compton (IC) process. The electron population which is required for the IC process also explains the presence of X-ray emission which, in this scenario, is generated by synchrotron radiation.

Inverse Compton Scattering

Compton Scattering is known for example from the absorption process of X-rays in material, where the incoming X-ray photon transfers its energy to an electron in an inelastic

collision. In the Inverse Compton Scattering, the electron is highly relativistic and a fraction of its energy is transferred to a scattered seed photon. The typical seed photons which are available in PWNe are the cosmic microwave background (CMB) and possibly IR emission from star dust as well as star light. When viewed in the rest frame of the electron, the photon exhibits a high transformed energy. The resting electron is upscattered like in the normal Compton process. Transferred back to our observer frame, the photon has gained, in extreme cases, several hundred TeV.

Two quantities are of interest. The first is the spectrum of the γ-ray flux $\mathrm{d}N_\gamma\left(E_\gamma, t\right)$ per energy range of the upscattered photons $\mathrm{d}E_\gamma$ and time dt produced by an electron plasma and the second, important for evolution of the electron plasma, is the cooling rate τ_{IC} of the electrons. Both depend on the cross section σ_{KN} for the Compton scattering of a photon and an electron. The cross section is given by the Klein-Nishina formula (e.g. [81]):

$$\sigma_{KN} = \pi \cdot r_e^2 \cdot \frac{1}{\epsilon} \cdot \left\{ \left[1 - \frac{2 \cdot (\epsilon + 1)}{\epsilon^2} \right] \ln\left(2\epsilon + 1\right) + \frac{1}{2} + \frac{4}{\epsilon} - \frac{1}{2\left(2\epsilon + 1\right)^2} \right\} \quad (1.19)$$

where r_e is the classical electron radius and ϵ is the product of the upscattered photon energy E_γ and the electron energy Γ (Lorentz factor) both expressed in units of $m_e c^2$. The cross section can be simplified for $\epsilon \ll 1$ to the Thomson cross section σ_T:

$$\lim_{\epsilon \to 0} \sigma_{KN} = \frac{8\pi}{3} \cdot r_e^2 \quad (1.20)$$

The limit implies that in the observer frame, the electron exhibits a comparatively high energy or the initial energy of the seed photon is relatively high (e.g. star light instead of a photon of the cosmic microwave background). A solution for the γ-ray flux is given by G. R. Blumenthal and R. Gould (Eqn. 2.65 in [28]) assuming a blackbody distribution for the seed photons and a power law with the index α for the electron population:

$$\frac{\mathrm{d}N_\gamma\left(E_\gamma, t\right)}{\mathrm{d}E_\gamma \cdot \mathrm{dt}} \propto \left(E_\gamma\right)^{-\frac{\alpha+1}{2}} \quad (1.21)$$

With the photon energy density u_γ, the cooling rate in the Thomson limit is (Eqn. 2.18 in [28]):

$$\tau_{IC} = \frac{4}{3} \cdot \sigma_T \cdot c \cdot \Gamma^2 \cdot u_\gamma \quad (1.22)$$

The opposite case of the Thomson limit is the Klein-Nishina limit with $\epsilon \gg 1$. In this limit, the cross section is:

$$\lim_{\epsilon \to \infty} \sigma_{KN} = \frac{8\pi}{3} \cdot r_e^2 \cdot \frac{1}{\epsilon} \cdot \left(\ln 2\epsilon + \frac{1}{2} \right) \quad (1.23)$$

The electron energies where the Klein-Nishina limit has to be considered are estimated as 300 TeV for the CMB ($kT = 0.25 \cdot 10^{-3}$ eV), 10 TeV for the IR emission from star dust

($kT = 20 \cdot 10^{-3}$ eV) and 300 GeV for visible star light ($kT = 1.5$ eV) in [61]. The γ-ray flux follows a power law with an index $\alpha + 1$ (instead of $\frac{\alpha+1}{2}$ in the Thomson limit):

$$\frac{\mathrm{d}N_\gamma\left(E_\gamma, t\right)}{\mathrm{d}E_\gamma \cdot \mathrm{d}t} \quad \propto \quad \left(E_\gamma\right)^{-(\alpha+1)} \tag{1.24}$$

The cooling time in the Klein-Nishana limit can be expressed with the τ_{IC} given in Eqn. 1.22 multiplied with a correction factor (Eqn. 2.28 in [28]):

$$\tau_{IC} \quad = \quad \frac{4}{3} \cdot \sigma_T \cdot c \cdot \Gamma^2 \cdot u_\gamma \cdot \frac{1}{\left(1 + E_{Ph} \cdot \Gamma\right)^{1.5}} \tag{1.25}$$

where E_{Ph} is the energy of the seed photon field.

In today's computer-powered models, the Inverse Compton process is not restricted to analytical solutions of one of these limits. Instead, a numerical integration over the seed photon distribution and the lepton plasma is carried out to derive the spectral distribution of the γ-ray flux from Inverse Compton scattering. A possibility for understanding the TeV γ-rays without setting up an implementation for the numerical integration is the formula for the mean energy of the upscattered γ-rays $\langle E_\gamma \rangle$ in the Thomson limit (Eqn. 2.24 in [28]):

$$\langle E_\gamma \rangle \quad = \quad \frac{4}{3} \cdot \Gamma^2 \cdot \langle E_{Ph} \rangle \tag{1.26}$$

whereas γ is still the Lorentz factor for the scattering electron and $\langle E_{Ph} \rangle$ is the mean energy of the seed photon field. For a given blackbody spectrum as photon field, $\langle E_{Ph} \rangle$ is a constant:

$$\langle E_{Ph} \rangle \quad = \quad 2.7 \cdot kT \tag{1.27}$$

Synchrotron Radiation

Electrons that are accelerated by a magnetic field perpendicular to their direction of motion and to the direction of the magnetic field will radiate synchrotron light. The radiation process can be understood as Inverse Compton scattering of virtual photons generated by the magnetic field of the electrons. If the angle between an electron's direction of motion and the magnetic field is ϑ and the speed of the electron is β (measured in units of the speed of light), then the energy loss of the electron due to synchrotron emission is (e.g. Eqn. 2.21 in [28]):

$$\frac{\mathrm{d}E}{\mathrm{d}t} \quad = \quad -\frac{2 \cdot r_e^2}{3c^3} \cdot \Gamma^2 \cdot \beta^2 \cdot B^2 \sin^2 \vartheta \tag{1.28}$$

The resulting cooling time for an electron plasma with an isotropic pitch angle ϑ is:

$$\tau_{syn} \quad = \quad \frac{4}{3} \cdot \sigma_T \cdot c \cdot \Gamma^2 \cdot \frac{B^2}{8\pi} \tag{1.29}$$

The synchrotron cooling is similar to the cooling time of the Inverse Compton scattering in the Thomson limit (Eqn. 1.22), although the energy density of the seed photon field is replaced by the energy of the magnetic field. The similarity of the energy loss rate to the IC process allows to estimate the magnetic field strength from the ratio of the integrated X-ray flux f_X to the integrated TeV flux f_{TeV}:

$$\frac{f_X}{f_{TeV}} \propto B^2 \tag{1.30}$$

1.3 The Pulsar Wind Nebula Vela X

In the previous Sections, the mechanism to fill a pulsar wind nebula with a plasma of accelerated particles using the pulsar's spin down power has been outlined. In this Section, the situation for Vela X is discussed and the observation results (Sec. 1.1) are interpreted in this context. These are the TeV substructure / the X-ray feature, the displacement of the pulsar wind nebula relative from the pulsar and the consequence regarding the spectral energy distribution (SED) for the electromagnetic flux from radio to TeV.

The timing of the pulsar as the engine of Vela X was described by Lyne et al. [84]. They found a period $P = 89.3$ ms and $\dot{P} = 1.25 \cdot 10^{-13}$ s^{+1} s^{-1}. Considering the standard assumption for the moment of inertia, the recent spin-down power of the pulsar is:

$$L = 5.6 \cdot 10^{36} \text{ erg s}^{-1} \tag{1.31}$$

The pulsar is known to exhibit "glitches" which are sudden increases in the rotation rate. Lyne et al. proposed a method to remove the glitches from the time structure of the pulsar and found a braking index of $n = 1.4$. Using Eqn. 1.8, it yields an age of $\tau = 57 \cdot 10^3$ a. However, the commonly stated characteristic age for the Vela Pulsar is $\tau = 11 \cdot 10^3$ a, derived under the assumption that the young pulsar exhibits a much larger braking index of $n = 3$. In comparison with other pulsars and in particular with the pulsars powering a detected pulsar wind nebula, Vela is classified as a middle aged pulsar.

Caraveo et al. [33] measured the distance to the Vela Pulsar to 294^{-50}_{+76} pc in parallax observations with the Hubble Space telescope[7]. As a side-product of the measurement, a velocity of 65 km/s (ΔRA $= 10.0 \cdot 10^{-6}$ deg a^{-1} and ΔDec $= 7.8 \cdot 10^{-6}$ deg a^{-1}) relative to the local environment on the two-dimensional sky was found. Using the geometry of the toroidal structure of the termination shock (Fig. 1.6), a three-dimensional velocity can be derived to 81 km/s. The velocity of the Vela Pulsar is relatively small compared to the mean three-dimensional velocity for pulsars of 450 km/s found by A. G. Lyne and D. R. Lorimer [83]. One has to note, that the set of 99 pulsar used for the estimation of the mean velocity is not representative. On the other hand, for the evolution of the pulsar wind nebula of a middle aged pulsar, it can be important that the pulsar has not left the original PWN

[7] http://hubble.nasa.gov

bubble defined by the interaction with the RS. That said, the Vela Pulsar is not a typical representative for a velocity measurement. A second recent measurement of the distance to the Vela Pulsar yields 287^{-17}_{+19} pc and has been performed also on the parallax of the Vela Pulsar with radio observations [39]. It is commonly assumed that the momentum seen as proper motion of the pulsar is transferred during or shortly after the core collapse supernova explosion and that later the velocity of the pulsar keeps undisturbed. The measured motion from the parallax measurements allows to estimate the birth position of the pulsar (the site of the supernova) depending on the pulsar's age. Using the recent position RA = $08^h35^m21^s$, Dec = $-45°10'35''$ (J2000) and neglecting the motion of the local environment (including the SNR shell) relative to the Earth, the birth position for τ_c = 11 ka is RA = $08^h35^m59^s$, Dec = $-45°15'43''$ (J2000). For an age of 20 ka, the birth position is RA = $08^h36^m31^s$, Dec = $-45°19'59''$ (J2000) and RA = $08^h38^m17^s$, Dec = $-45°34'05''$ (J2000) for 50 ka. In Figure 1.3(b), the expected birth position for an age of 11 ka is indicated with an open star.

1.3.1 Displacement of the Nebula to the Pulsar

In the large-scale maps observed in different wavelengths (Radio: Fig. 1.4(b), X-rays: Fig. 1.3(c), TeV γ-rays: Fig. 1.2), the Vela Pulsar is displaced from the center pulsar wind nebula by almost 1°. From the simple idea that the pulsar fills the PWN with a high-energy particle plasma, one expects that the PWN forms a symmetric sphere, maybe slightly deformed to an ellipsoid perpendicular to the rotation axis. As the pulsar's proper motion is relatively small, the displacement cannot be explained by the pulsar's motion. J. M. Blondin et al. proposed that the reason for the asymmetry of the PWN with respect to the pulsar is induced by an asymmetry in the density of the surrounding ISM [27]. The solution of S.E.S. Ferreira and O.C. de Jager will be referred in the following discussion [46], where the supernova shock is simulated with a hydrodynamic model including kinetic calculations for the magnetic fields. The authors discussed the application of their model to the Vela SNR.

In Figure 1.7 the situation which is supposed to describe Vela X some thousand years after the supernova explosion is sketched. Compared to the symmetric case presented before (Fig. 1.5), the supernova shock front moves against a dense ISM in the north (drawn as gray area). In X-rays radii of 3.75° (18.8 pc) for the north-eastern and 4.2° (21.0 pc) for the south-western parts of the SNR are found (Fig. 1.3). An atomic hydrogen density of 1–2 particles per cm^3 was determined for the northern parts of the SNR [41], while for the southern ISM a density of 0.1 particles per cm^3 is assumed [46]. In the simulations of S.E.S. Ferreira and O.C. de Jager, the transition between the thin and the dense ISM is a sharp step. The denser ISM causes the forward shock to propagate slower than in the thin medium, and likewise the reverse shock will return earlier than from the direction of the thin medium. When the northern RS reaches the freely expanding PWN, it pushes the PWN plasma to the south. Neglecting the exists of the PWN, the return time for the

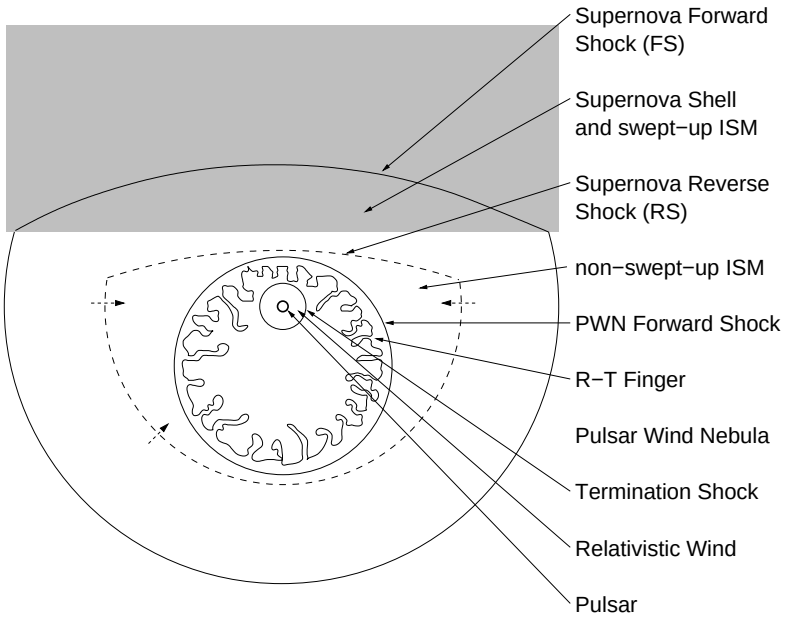

Figure 1.7: The expansion of the supernova shell in two different ISM is sketched here. The denser medium is drawn as gray area at the top of the sketch. The reverse shock of the SNR shell already has turned back towards the center of the SNR. It pushed the PWN in southern direction (bottom of the sketch) until the southern RS on the opposite side of the SNR also reached the PWN.

RS from the north to the position of the pulsar is about 4000 a. At the same time the southern RS has reached the pushed PWN bubble on the opposite site.

For the development during the next 7000 a (assuming an age of $\tau_c = 11$ ka) until today, it has been suggested that the position and volume of the PWN are stable. In order to achieve a scenario consistent with the leptonic scenario of de Jager et al. discussed below (Sec. 1.3.3), the authors postulate stable conditions. The scenario requires the stable conditions for accumulated high-energy leptons over several thousand years. S.E.S. Ferreira and O.C. de Jager neglected in their work the interaction of the reverse shock with the PWN. Amongst others, they leave the question open, how the characteristics of the PWN plasma change when the RS reaches the PWN and if there is a continuous interaction between the hot SNR shell material and the PWN plasma. The argumentation of S.E.S. Ferreira and O.C. de Jager is that the adiabatic compression after the crash with the RS is compensated by the subsequent adiabatic expansion.

1.3.2 The Nature of the Jet-like Feature

One of most prominent features within the Vela nebula is the jet-like X-ray structure seen by the ROSAT satellite (Fig. 1.3(c)). As for the origin of the structure, several interpretations were suggested. The interpretation is important in understanding the observations

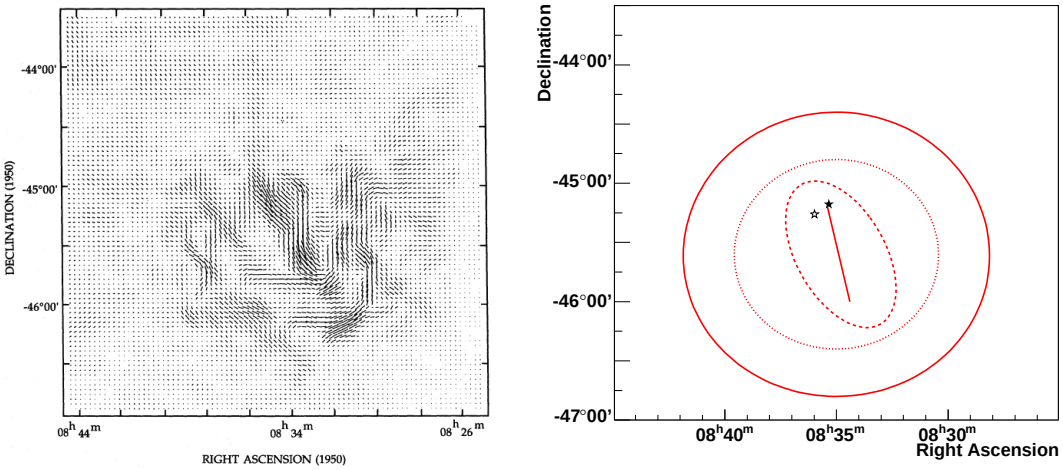

(a) magnetic field (b) overview map

Figure 1.8: a) The map of the projected magnetic field in the Vela X region was derived from the differences in Faraday rotation between the polarization directions in three radio frequencies [91]. b) The overview map shows the same field of view as the map of the projected magnetic field including the same objects as Figure 1.3: the Vela Pulsar is marked as filled star, the estimated birth position of the Vela Pulsar as open star (11 ka), the direction of the jet-like feature as red line, the X-ray "Cocoon" around the feature as red broken line and the PWN Vela X as red circle (solid line: radius 1.2°, dotted line: radius 0.8°).

of Vela X in different wavelengths. The various alternative interpretations are presented in the following.

The first interpretation announced together with the discovery of the structure is that the pulsar injects high-energy particles into a jet that propagates about 1° southwards and is terminated in a "Cocoon". An estimate for the velocity of the jet constituents is ∼1100 km s^{-1}, while the mass flux received in the jet's head is 10^{-5} $M_\odot$ per year [47]. To allow such a high flux over the life of the pulsar ($\tau = 11 \cdot 10^3$ a), it is required that the pulsar introduces much faster particles which then swept-up mass on its way southwards to the head [88]. A caveat of this jet interpretation is the asymmetry. The question why there is no counter-jet propagating to the north remains open.

V. Gvaramadze suggested that the X-ray feature is part of the SNR shell [52]. The suggestion is based on a comparison with the filamentary structures spread over the whole SNR, e.g. a radio arc connecting Vela X and Vela Junior in the north of both sources. Thereby the X-ray feature is by chance between the observer and the Vela Pulsar. In consequence, the X-ray feature and the radio arc are supposed to be a Rayleigh-Taylor instability of the SNR shell. This should not be mixed up with RT instabilities at the interface between the PWN and the RS.

The preferred interpretation in this thesis is that the magnetic field strength is inhomogeneous within the PWN, whereby a compressed magnetic field is arranged along the

X-ray feature. In Figure 1.8, a measurement of the magnetic field is shown. The field has been estimated from polarized radio measurements at 8.4 GHz, 5 GHz and 2.7 GHz comparing the Faraday rotation [91]. A strong magnetic field has been found along the X-ray feature. It has been suggested that a finger rising from a RT instability between the PWN and the RS puncture the PWN almost in its center on a length of several parsec. The magnetic field lines within the PWN rearranged parallel to the finger. A further interesting suggestion is that the structure of the magnetic field was originally determined by the termination shock and then survived the displacement of the PWN, a moderate contraction and the reexpansion.

Unfortunately, no final conclusion regarding the nature of the X-ray feature has been reached so far. The association as a part of the SNR is commonly rejected. A thermal component was found for the feature in the ROSAT observation with a temperature of 3–4 keV, while the temperature of filaments in the SNR is 0.1–0.2 keV [88]. The orientation of the double torii structure in the high-resolution image taken Chandra satellite from the termination region (Fig. 1.6) contradicts the orientation of the feature. Therefore today, the interpretation as jet directly powered by the pulsar is also obsolete.

1.3.3 Modeling Vela X for a Leptonic Scenario

At the termination shock, the pulsar's relativistic wind is converted into a plasma that is accumulated in the PWN bubble. The standard assumption is that the plasma consists of electrons and positrons, typically referred to "leptonic model". Recent models integrate the particles introduced at the termination shock over the lifetime of the pulsar and simulate the development of the accumulated leptons in the PWN. The models are typically restricted to one zone, like the recent presentation from Zhang, Chen and Fang (ZCF) [106]. The term "one-zone model" means that only one (leptonic) plasma is regarded with a spatially constant plasma density and effective magnetic field strength. Within the model, the change of the number of plasma leptons N_e can be expressed as:

$$\frac{\mathrm{d}N_e\left(E_e,t\right)}{\mathrm{dE}_e\cdot\mathrm{dt}} = Q\left(E_e,t\right)-\sum_i\frac{\mathrm{d}N_e\left(E_e,t\right)}{\mathrm{dE}_e\cdot\tau_i\left(E_e\right)} \tag{1.32}$$

Q is the injection of the leptonic plasma by the wind termination into the nebula (Eqn. 1.14). τ_i is the lifetime for leptons at the energy E_e to remain in the plasma, whereas the index i denominates different processes. In the specific model (ZCF) the processes are synchrotron radiation (Eqn. 1.29) and escape losses. The solution of the differential Eqn. 1.32 for the accumulated leptons from the birth of the system to a certain point in time T (e.g. the characteristic age) is:

$$\frac{\mathrm{d}N_e\left(E_e,t\right)}{\mathrm{dE}_e} = \int_0^T Q\left(E_e,t\right)\cdot\exp\left(-\frac{T-t}{\tau_{eff}\left(E_e\right)}\right)\cdot\mathrm{dt} \tag{1.33}$$

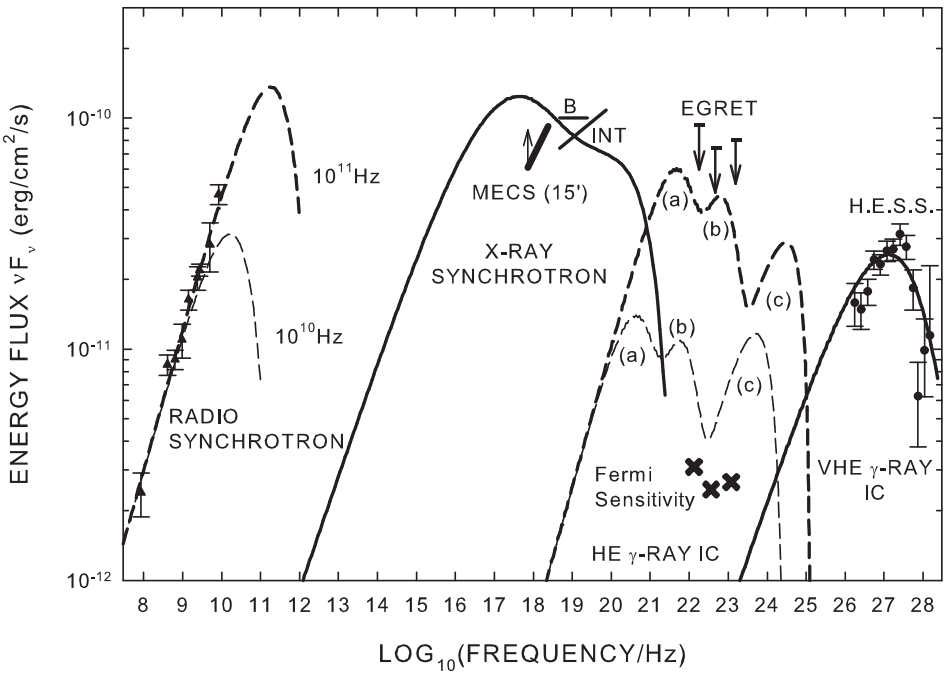

Figure 1.9: The SED for the energy flux from Vela X includes measurements across almost the complete energy range. Data points are given in the radio and TeV range (H.E.S.S.). The results of X-rays observations (B, INT) and the lower limit (MECS) are drawn as lines. In the GeV range upper limits (EGRET) are indicated with arrows. The solid thick line displays a model for a leptonic plasma component that explains the TeV γ-rays and X-rays as IC and synchrotron photons. The dashed lines originate from a second leptonic component, while the think and thin line differs in the intensity of the leptons in the PWN. The SED was taken over from [38]. Details on the model and references on the data points are given in the text and in [38].

where τ_{eff} is reciprocal sum of the τ_i. The integral is calculated numerically.

A specified leptonic model for Vela X has been developed by de Jager, Slane and LaMassa [38] using the same approach for time development of the leptonic plasma as ZCF. In contrast to ZCF, the radiation losses τ_{eff} also include the Inverse Compton process. That is necessary as the intensity of the IC seed photons from star light is rather strong. Hence the leptons can transfer a relevant fraction of their energy E_e within the Klein-Nishina regime (Eqn. 1.23) to these seed photons. The model explains the spectral energy distribution (SED) for the observation in the TeV γ-rays with the IC emission of the same leptons that also produces the X-rays as synchrotron radiation. Similarly, the radio spectrum is the synchrotron radiation of a second population of leptons which will generate IC γ-rays in the GeV range. In Figure 1.9, the SED including the model and measurements for four photon flux peaks. The H.E.S.S. data points were been taken from observations between 2003 and 2005, which have been published in 2006 [6]. In Section 6.3, the results based on recent observational data will be presented. To support the associated synchrotron

peak in the X-ray range, a lower limit on the flux from the MECS and the flux from the PDS instrument on the BeppoSax satellite [86]. Additionally, the result from the Integral satellite[8] is given. The Integral flux shows a rising trend while the model on the spectral shape in the integral range is flat. Unfortunately the line in the SED shows the Integral flux as combined flux from the pulsar (pulsed) and the PWN (unpulsed). An estimate only for the unpulsed PWN flux is in good agreement with the model [59].

The radio data points were taken from [15] and [53], Within these References evaluates the integrated flux density from archival data between 1958 and 1995. At the time when the SED was created, it was unclear at which frequency the maximal radio/microwave flux can be found. The problem of estimating the model parameters for the radio / GeV component can also be solved by measuring the GeV flux level. As consequence de Jager et al. gave two models (thick and thin line in Fig. 1.9), where the conversion efficiency for the pulsar spin-down luminosity to the second component is $\eta = 0.45$ or $\eta = 0.35$, respectively. The GeV flux is estimated using upper limits derived from EGRET observations [37]. Meanwhile the results from current satellite missions FERMI [1] and AGILE [96] are available. The results confirm the $\eta = 0.45$ model (thick line). However, there is a disagreement in the flux measurement of the spectral shape between AGILE and FERMI. The AGILE spectrum (100 MeV to 3 GeV) shows an increasing flux to higher energy while Fermi (200 MeV to 20 GeV) shows a falling flux in this range.

Leptonic one-zone models are commonly preferred to describe PWNe. The version of the model endorsed here is important in the following discussion. In particular, de Jager et al. especially used the morphological argument that the TeV emission region of nebula is consistent with the X-rays "Cocoon" around the X-ray feature. It will be shown in Chapter 6 that the PWN plasma responsible for the TeV emission can be found throughout the whole nebula as seen in radio. Although this breaks the morphological argument, the synchrotron / IC association of X-rays and TeV photons is still possible. An important point of the leptonic model is that the power required for the second component is in the order of the spin down luminosity, so that no further explanation is needed for the balance of initial pulsar energy contributed between the pulsar wind outflow and the remaining rotation. That is, the TeV / X-ray component and therefore also the TeV flux observed from Vela X does not contribute to the problem of the energy balance.

1.3.4 An Alternative Hadronic Scenario

In hadronic scenarios for PWNe, it is assumed that at the termination shock of the relativistic wind injects a hadronic component into the PWN. The hadrons collide inelastically with the remaining gas of the ISM in the PWN. Thereby neutral pions are generated, which again decay into two γ-rays (98.798 %, [92]). Apart from the hadronic component, an injection of a population of "primary" electrons into the nebula is assumed. The electrons are suggested to generate the X-ray signal of the nebula. In the hadronic particle

[8] http://sci.esa.int/science-e/www/area/index.cfm?fareaid=21

interactions, also electrons as secondary particles are produced, e.g. in the decay of charged pions. The electrons from this second component are used to explain the radio nebula.

A hadronic scenario for Vela X has been given by D. Horns et al. [66], where a combination of ions and electrons compose the PWN. The argumentation bases upon simple estimate of the energy balance of the pulsar's spin-down luminosity. Assuming a magnetic field strength of 10 μG and a radius of 4 pc (0.8°) for the extension of Vela X almost all (70 % for protons, 100 % for heavier ions) ions injected over the lifetime of Vela X remain in the nebula. If one takes the extended size of Vela X of 6 pc (1.2°) into account, also 100 % of the protons have remained in the PWN. On the other hand, the luminosity seen from the PWN in the TeV energy range from 550 GeV to 65 TeV was reported to be $L_\gamma = 10^{33}$ erg s^{-1} [6] at a distance of ∼290 pc. The average time it takes for a proton to produce a π^0 in a collision with protons from the ISM has been derived from Monte Carlo simulations as $t_{pp} = 2.5 \cdot 10^8$ a, at an ISM density n of 0.6 particles per cm^3. The total energy W_p of the proton plasma in the PWN required to generate the observed TeV luminosity via π^0 decay can be estimated roughly as:

$$\begin{aligned} W_p &= 164.4 \cdot L_\gamma \cdot t_{pp} \\ &= 1.1 \cdot 10^{49}\ \text{erg} \cdot \left(\frac{L_\gamma}{10^{33}\ \text{erg/s}}\right) \cdot \left(\frac{n}{0.6\ \text{cm}^3}\right) \end{aligned} \tag{1.34}$$

The estimated total energy W_p is in the order of the assumed initial rotation energy $E_0 = 4 \cdot 10^{49}$ erg.

1.4 Prospects of γ-ray Observations on Vela X

The concept of pulsar wind nebulae has been introduced both as a general idea and applied to the particular example of Vela X. Thereby, a pulsar wind nebula is a particle plasma – commonly assumed to consist of leptons – that fills a bubble volume cleared by a preceding supernova explosion. The nebula is powered the pulsar by an injection of new high-energy particles. The time evolution of the nebula plasma is simulated for mean states over the whole volume in so-called one-zone models. The important processes for a leptonic plasma are the cooling through synchrotron radiation, loss of particles escaping from the nebula and adiabatic changes due to expansion or compression of the nebula. Inverse Compton processes are used to explain the γ-ray luminosity in the TeV range. However, it becomes apparent that the pulsar wind nebulae should not be regarded as isolated objects but rather in the context of a supernova remnant including the interaction with the reverse shock of the supernova shell.

For Vela X in particular, our knowledge stems from observations in radio, X-rays, GeV and TeV γ-rays. The Vela Pulsar with its characteristic age of 11 ka is typically referred to a middle-aged pulsar, which leads to the assumption that the reverse shock has already returned. The observed displacement of the nebula from the pulsar supports the assumption of return of the shock. As Vela X hosts the nearest middle-aged pulsar

driving a spatially resolvable nebula, it is considered as a classical example for studies on pulsar wind nebulae. One should keep in mind that this classical use of Vela X might have biased the development of pulsar wind nebula models in general as presented above, so that effects seen in other objects – like the spectral dependency of the TeV signal in HESS J1825 (see Sec. 6.3.4) – are not considered.

This thesis comprises a reanalysis of the TeV γ-ray observations performed with the H.E.S.S. telescopes between 2003 and 2009. Data since 2006 have not yet been need for a publication by the H.E.S.S. collaboration. The reanalysis can be found in Chapter 6, and some open problems regarding Vela X, which the H.E.S.S. observations may help to solve, are revisited:

Extension of the Vela X nebula The extension of Vela X differs between the observations in radio bands (typically $3^\circ \times 2^\circ$), X-rays ($45' \times 12'$ for the jet-like feature [87]) and γ-rays (radius of 0.8° [6]). Here, the preferred interpretation is that there is only one nebula volume and the different extensions can be explained by an inhomogeneous plasma and magnetic field density. The TeV flux assumed to originate from Inverse Compton Scattering or even from π^0 decays probe the plasma density distribution of the nebula. On the other hand, the synchrotron emission seen in X-rays depends on the local magnetic field strength.

Nature of the jet In the image establishing the first detection of Vela X by H.E.S.S. the TeV nebula follows the "Cocoon-like" X-ray corona around the feature, but the feature itself has not been detected (e.g. Figs. 1 and 2 in [6]). A counterpart of the X-ray feature in TeV γ-rays would limit the constraints for the origin of the feature.

TeV spectrum of Vela X The spectral energy flux distribution clearly exhibits a maximum in the TeV range (see e.g. Fig. 1.9). A detailed description of the maximum allows to test models for the particle plasma and the assumed γ-ray emitting process. The new H.E.S.S. data will contribute improving the measurement of the spectral shape.

Additional spectral component above 50 TeV An additional problem regarding the TeV flux is, in which way the spectrum develops at high energies. The 2006 H.E.S.S. differential γ-particle spectrum follows a power law with exponential cutoff. However, the flux estimate of the last bin at $\sim$50 TeV exceeds the power-law expectation by about twice the error estimation. If such a flux in this 50 TeV bin and maybe beyond this last bin can be confirmed, a discussion either on newly injected leptons or on an additional, but weaker high-energy hadron component could be started.

Energy dependent morphology The pulsar continuously injects particles into the nebula plasma. If the injection is strong compared to the already existing plasma, a measurement of the spectral shape of the TeV γ-ray flux at the pulsar position allows to study the newly injected plasma in comparison with the remaining TeV spectrum for the PWN.

Chapter 2

The Imaging Atmospheric Cherenkov Telescope Technique

If a high-energy particle reaches the Earth's atmosphere, it will interact with the molecules of the air. Thereby secondary particles are generated and the energy and momentum of the primary particle are distributed to the secondary particles. The process is repeated for the secondary particles, such that a particle cascade – a so-called air shower – develops. Commonly there are three types of detection principles for air showers (referred by e.g. [92]). The first one uses detectors on the ground that directly detect the shower particles. Fluorescence telescopes used by the second principle. When air showers penetrate through the atmosphere (see below), the N_2 molecules along the shower path are excited, which thus subsequently relax to the ground state partially by the emission of fluorescence photons. This light is then detected in the fluorescence telescopes. The third principle is based on the Imaging Atmospheric Cherenkov Telescopes (IACTs) technique which detects the Cherenkov light emitted by the charged particles in an air shower.

Here the showers, where the generation of secondary particles stops and the particles are absorbed by the atmosphere before they hit the ground, are of interests. These showers are detected with the IACTs. The air showers can be divided into two types pure electromagnetic and hadronic ones. In case of an electromagnetic showers, the primary particles are either γ-rays or electrons[1] and in case of hadronic showers, the primary particle is a hadron. The air showers induced by γ-rays in the energy range between 100 GeV to 100 TeV are the objects in astronomical observations, while hadronic air showers generates background for these observations.

[1]Positrons will not be separately accounted in the description of air showers, each time it would be appropriate.

2.1 Cherenkov Light from Charged Particles

A charged particle that moves through a medium polarizes the medium locally around its instantaneous position. If the speed of the particle is faster then the phase velocity of the light in the medium, the depolarization will take longer than the particle needs to leave the locally polarized region. Along the particles path an electromagnetic wave is formed. The waves along the path constructively interfere and light is emitted. This effect is known as Cherenkov effect and the emitted light is called Cherenkov light. The geometry of the cone is sketched in Figure 2.1(b). With the speed of the particle β (expressed in units of the speed of light c) and the phase velocity $\frac{1}{n}$ of the light in the medium with the refraction index n, the opening angle θ_C of the cone is given by:

$$\cos\theta_C = \frac{1}{n} \cdot \frac{1}{\beta} \tag{2.1}$$

The opening is called Cherenkov angle. θ_C reaches a maximum in dependence of the refraction index, if β is almost 1. Transferring this limit $n \cdot \beta > 1$ to a minimum energy for a charged particle to emit Cherenkov light, one gets:

$$E_{min} = \frac{m \cdot c^2}{\sqrt{1 - \frac{1}{n^2}}} \tag{2.2}$$

θ_C in the Cherenkov limit ($\beta \to 1$) and the minimum energy can be derived for the electrons that emits the light in the air showers. The showers develop several thousand meters above the sea level, where the refraction index of the atmosphere is $n = 1.0001$. The minimum energy is $E_{min} = 36.1$ MeV and the maximal opening angle yields $\theta_C = 0.8°$.

A second issue, where the Cherenkov effect occurs, are muons generated in the air showers. If a single muon passes near by a telescope, the intensity of the Cherenkov light seen by telescope is in the same order as the intensity from air showers. With a refraction index of $n = 1.00024$ (at a height of $h \approx 1800$ m), the minimal energy is 4.8 GeV and the Cherenkov angle is $\theta_C = 1.26°$. The muons which reach the ground have typically energies above the minimal energy (for the muon spectrum on the ground see Fig. 24.4 of [92]), so that the light cones are seen as rings in the camera images. In Section 3.1.3, these well-defined ring images are used for calibrating the telescopes optical efficiency. For the record, the number of Cherenkov photons emitted per path length and within the wavelength λ_1 and λ_2 is given by:

$$\frac{\mathrm{d}N}{\mathrm{dx}} = 2\pi\alpha z^2 \int_{\lambda_1}^{\lambda_2} \left(1 - \frac{1}{(\beta n(\lambda))^2}\right) \frac{1}{\lambda^2} \mathrm{d}\lambda \tag{2.3}$$

where α is the fine structure constant and z the charge number of the charged particle.

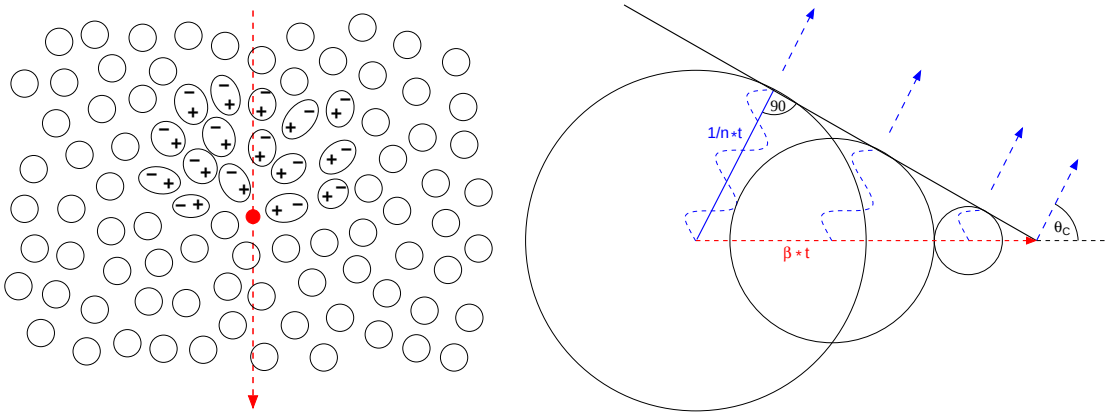

(a) polarization of the medium (b) construction of the Cherenkov angle

Figure 2.1: a) The plot illustrates the polarization of a medium by a charged particle moving faster than the phase velocity of light. The polarization arises from atomic or molecular electric dipoles (in the sketch oriented towards the path of the negatively charged passing particle). b) The path which the charged particle of speed β covers in the time t is drawn as a red arrow. The electromagnetic wave is displayed with the blue broken lines outgoing from the positions that the particle crossed at t, $\frac{3}{5}t$ and $\frac{1}{5}t$. The constructed wave front is the thick black line. A realistic Cherenkov angle θ_C in the atmosphere is definitely smaller than drawn in the sketch, as $1/n$ and β are both close to 1.

2.2 Electromagnetic Air Showers

In 1936, H. Bethe and W. Heitler described the interaction processes for the stopping of fast electrons in matter [26]. In their discussion, they refere to laboratory experiments for dense matter like lead cheats. The authors gave three elementary processes relevant for stopping: a) Bremsstrahlung of electrons passing an atomic nucleus, b) ionization of the passed matter and c) pair production of electrons and positrons from high-energy photons. Later Heitler applied the stopping model on very high energetic (VHE, 100 GeV) γ-rays in the atmosphere. The simple idea of the model for electromagnetic air showers is, that the secondary e^- / e^+ are emitting photons via Bremsstrahlung and that the photons annihilate in a pairs of e^- / e^+. The energy per particle decreases in each particle generation, until the particle cascade is stopped when the electrons lose their energy by ionizing the passed matter.

Bremsstrahlung occurs, if a charged particles passes the Coulomb field of a nucleus which is then accelerated and emits photons. The radiation length is defined as the integrated area density an electron passes along its path before it lost $1/e$ of its energy as Bremsstrahlung. For the atmosphere, the radiation length is $\lambda_r = 36.62$ g cm^{-2} [92]. The air shower model assumes that only single Bremsstrahlung processes are relevant, where the electron passes the nucleus nearby and emits a single photon with a photon energy in the order of half of its initial energy.

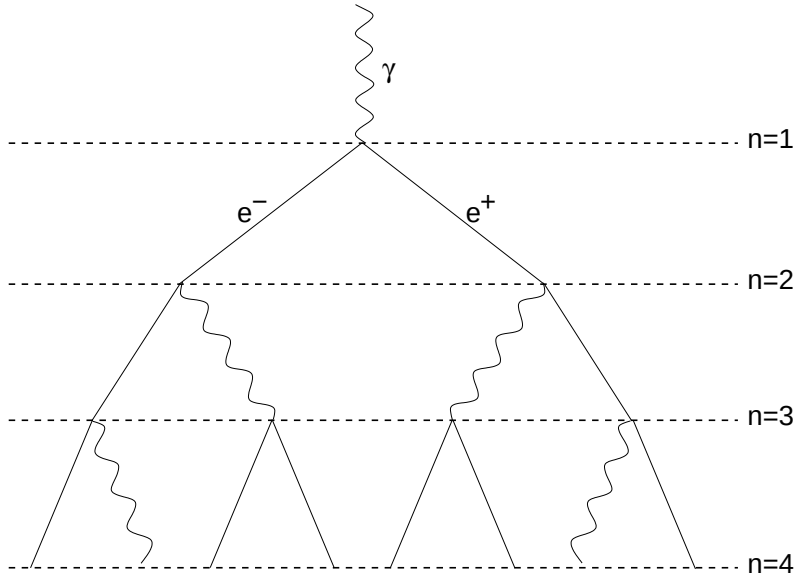

(a) electromagnetic air shower

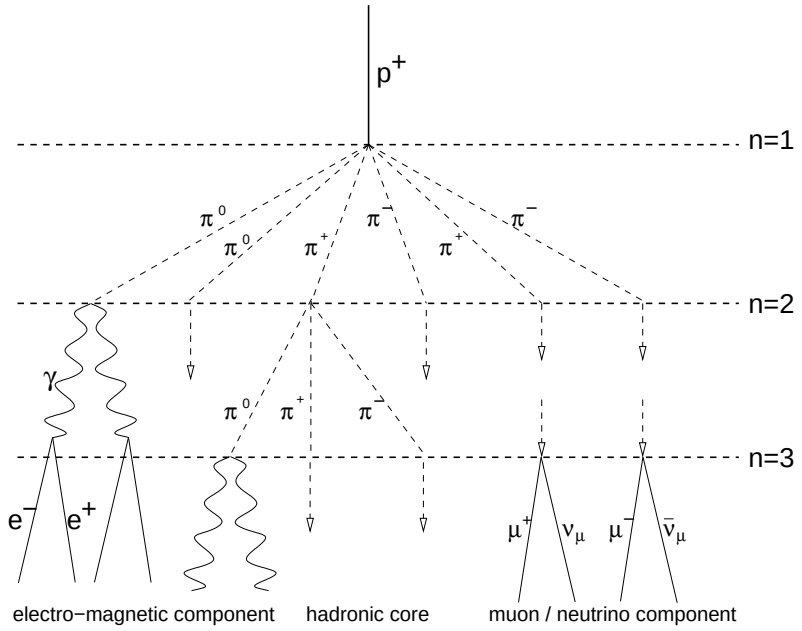

(b) hadronic air shower

Figure 2.2: a) The sketch shows the development of an electromagnetic air shower using the Heitler model in the first three particle generation. b) The scheme for hadronic air showers follows the Matthew model that considers only pions as final state particles for hadronic interactions. An electromagnetic component is released from the hadronic core via π^0 particles. The air shower stops when charged $\pi^{\pm}$ decay into muons / neutrinos rather than interacting in collisions with molecules of the atmosphere.

The second process for electrons that determines the development of the air showers is ionization of the passed matter along the electron's path. The ionization is decriben by the Bethe equation (see e.g. Chapter 27 in [92]). Here, the discussion is restricted to the critical energy E_c^γ at which the energy loss due to Bremsstrahlung is as large as for the Ionization. Below the critical energy the shower dies out and deposits its energy via ionization in the atmosphere. E_c^γ is in the order of 85 MeV [89].

The pair production is a similar process as the Bremsstrahlung. Thereby a photon decays into an electron and a positron closely by the Coulomb field of a nucleus. Neglecting the lepton masses, the extension of the nucleus and the screening of the Coulomb field by the electrons bound in the target atom, the cross section and therefore also the radiation length λ_{pp} for the pair production of e^-/e^+ by a photon is the same as the cross section for Bremsstrahlung by a lepton. If screening is considered, the radiation length of the pair production is slightly larger than the one of the Bremsstrahlung $\lambda_{pp} = \frac{9}{7}\lambda_r$ (see e.g. Section 1.4 in [32] in addition to [26]).

For applying the Heitler model to electromagnetic air showers, it is assumed here, that λ_r is equal to λ_{pp}. Bremsstrahlung and pair production processes occur exactly after the electron / photon has passed the path length of $\lambda_r / \ln(2)$. A third presumption is, that the initial energy of the primary is distributed uniformly on both secondary particles. In Figure 2.2(a) an electromagnetic shower is sketched. Each particle in the last generation before the shower stops, possess the critical energy. So that there are in sum n_p final particles:

$$n_p = \frac{E_{pri}}{E_C} \tag{2.4}$$

where E_{pri} is the energy of the primary photon. The number of generations n_g (depth of the tree) is:

$$n_g = \log_2\left(\frac{E_{pri}}{E_C}\right) \tag{2.5}$$

The model for electromagnetic showers (as sketched in Fig. 2.2(a)) is similar to the concept of a complete binary tree in computer science. Within this analogy, the n_g correspond to the height of the tree. The area mass density $a(h)$ of the atmosphere above the height h is estimated with the barometric formula:

$$a(h) = \int_\infty^h 360\frac{\mathrm{g}}{\mathrm{cm}^2} \cdot \exp\left(-1.6 \cdot 10^{-4}\frac{1}{\mathrm{km}} \cdot (x - 11\ \mathrm{km})\right) \cdot \cos(\theta_Z)\ \mathrm{dx} \tag{2.6}$$

θ_Z is the angle between the zenith and the incoming direction of the primary particle. For example, assuming a 1 TeV incident photon, 11800 secondary particles are produced in the last stage of the shower development. The number of generations in this shower is 13.5 (Eqn. 2.5) which correspond to an area mass density of 500 g cm^{-2}. A comparison of the

radiation length λ_r with the atmospheric area mass density yields 8200 m height above see level for the first interaction and 6600 m for the level, where the critical energy is reached.

The Bethe-Heitler model gives a first description for an electromagnetic air showers. For the analysis of the data of IACTs commonly more detailed models are applied. The reconstruction of γ-rays air showers that will be discussed in Section 3 are based on the shower simulation CORSIKA [56] ("COsmic Ray SImulations for KAscade").

2.3 Hadronic Air Showers

The description of hadronic air showers is more complex than the model proposed by Heitler for electromagnetic showers. Thus, simulations are required to understand the shower properties. As the primary goal of IACTs is the detection of γ-rays induced air showers, it is necessary to distinguish between electromagnetic and hadronic showers. In the γ / hadron separation (described in Section 3.3.4) different characteristics of both shower types are exploited. Thereby the hadronic air showers are more complex then the electromagnetic ones, as the inelastic collisions of shower particles with their targets (the molecules of the atmosphere) generates a bunch of several hadronic secondary particles.

A model for hadronic air showers analogue to Heitler has been suggested by J. Matthews [89]. The model assumes that only pions are produced in hadronic interactions. Pions (π^0, π^+, π^-) are the lightest mesons which consists of two quarks (up- and down-quarks and their anti-quarks). The interaction length for pions in air is given by $\lambda_I = 120$ g cm^{-2} and is assumed to be constant in the range of 10 to 1000 GeV. One third of the pions are neutral (π^0) and decays within a short lifetime with a probability of $\sim$98.8 % into two photons [92], at which the photons initiate electromagnetic sub-showers. The other two thirds are charged pions and generate again pions in inelastic hadronic collisions. For the hadronic air shower, a stopping condition is defined by the point, where the decay probability of the pions exceeds the probability for a pion to interact with air molecules. The last generation of π^- (π^+) decays into muons μ^- (respective anti-muons μ^+) and muon neutrinos ν_μ ($\bar{\nu}_\mu$). Matthews applied his shower model to showers with primary energies larger than 100 TeV. Although for further discussion of hadronic air showers, the Matthews model illustrates the fragmentation of the primary energy into a muon/neutrino component, electromagnetic sub-showers and the development of the hadronic shower core. His model is given in Figure 2.2(b).

The differences between both types of showers can be qualitatively described as follows. In doing so, the discussion make use of the previous argumentations in [20, 48, 65]:

- The transversal momentum of the secondary particles in the hadronic shower is larger. The consequence is that the Cherenkov light profiles as seen by the IACTs also broadens in the shower images (see below and Chapter 3).

- The electromagnetic air showers are more regular than the hadronic showers, therefore parameters gained from the shower images largely varies. As example in Figure 3.8, the length and width of the shower profiles is shown. The parameters are normalized to expectation values and the variances of γ-showers in dependence of the primary energy. One can see that the values of both, length and width, is multiple larger than the variances of the γ-showers.

- As the interaction length of protons ($\lambda_{I,p} \approx 85$ g cm^{-2}) is larger than the interaction length of pair production induced by γ-rays ($\lambda_{pp} \approx 47$ g cm^{-2}), the primary protons penetrate deeper into the atmosphere. The height of first interaction will be shifted to lower heights above the ground.

- In hadronic shower, non-negligible fractions of the primary energy goes into long lifetime particles (e.g. muons) that do not decay into further sub-cascades or even into neutrinos which are only interacting weakly and leave the shower unaffected. Hence, the ratio of the Cherenkov light intensity to the primary energy is lower for hadronic shower than for pure electromagnetic showers.

- In hadronic air showers, a large bunch of muons will reach the ground.

2.4 Detection of Cosmic Rays

The principle of detecting primary particles with Imaging Atmospheric Cherenkov Telescopes (IACTs) is explained in the following. In Figure 2.3(a) a primary particle (broken arrow), the initiated air shower (filled blue triangle), its Cherenkov light pool (inside the gray ring) and two telescopes on the ground are sketched. Following the Bethe-Heitler model, the first interaction of a primary photon will take place in a height of about 8200 m (Eqn. 2.6), whereat the generation of secondary particles range down to a height of 6600 m (for a primary energy of 1 TeV). The Cherenkov light is emitted by the secondary particles with an opening angle θ_C in the order of 1°. The area on the ground illuminated by the Cherenkov light is commonly termed Cherenkov light pool. A telescope situated in the light pool can detect the shower. The Bethe-Heitler model allows to estimate the size of the Cherenkov light pool[2]. Using the first interaction height of 8200 m for an γ-ray photon from the zenith and assuming $\beta \to 1$ for the secondary shower particles (Cherenkov limit) the radius of the Cherenkov light pool is 120 m and the detection area is $\sim 45 \cdot 10^3$ m^2. The inlay in Fig. 2.3(a) shows the Cherenkov light intensity over the impact parameter, at which the gray bar indicates the boundary of the light pool defined by θ_C. Around the boundary a light halo is found and the recent telescopes with mirror areas above 100 m^2 can also detect showers within this halo, so that realistic effective areas are a factor of 10

[2]The size of the Cherenkov light pool is a simple approximation for the detection area around the telescope which the original path of primary particle has to pass, so that an event is detectable for the telescope.

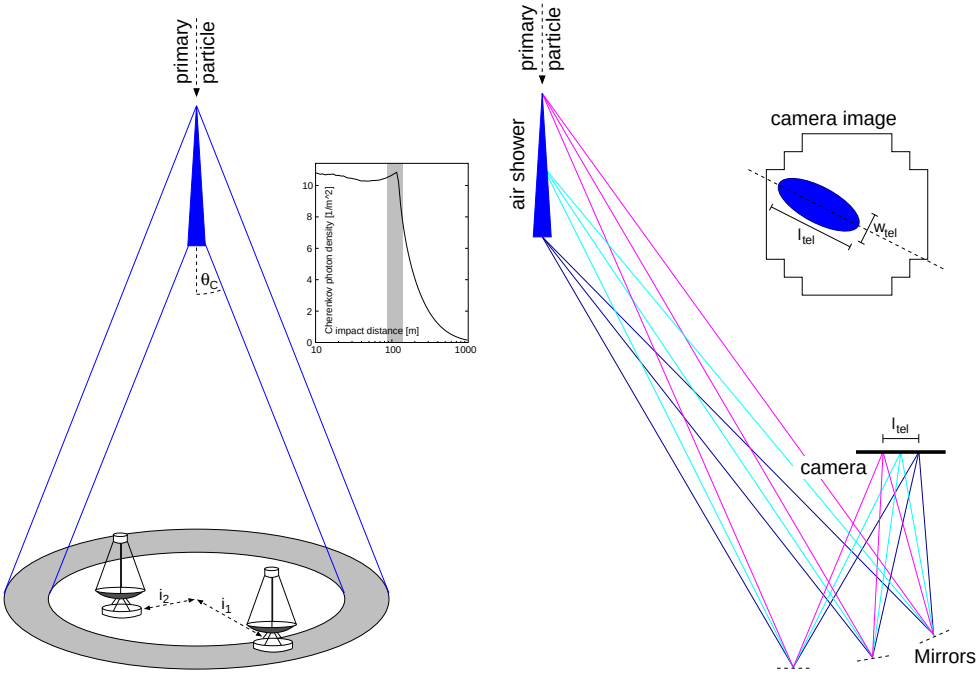

(a) Cherenkov Light Pool (b) ray tracing

Figure 2.3: a) The drawing shows the detection of an air shower (blue) induced by a primary particle with IACT telescopes. The gray ring spanned by the Cherenkov angle θ_C and the air shower elongation encloses the illuminated area on the ground. Two telescopes at impact distances i_1 and i_2 are included in this light pool. The inlay shows the number of Cherenkov photons (300 to 600 nm) from a 100 GeV γ-ray shower reaching the ground at 2200 m sea level for a so-called US standard atmosphere (Fig. 1 in Reference [22]), at which the gray bar indicates the boundary of the light pool. b) The optical path is sketched for Cherenkov light from the top, middle and bottom of an air shower over the telescope mirrors to the camera. The sketch is arranged along the line of intersection through the telescope position and the shower. The length l_{tel} and the width w_{tel} of the shower are indicated by rulers. A drafted camera image is shown as inlay including an image of the air shower.

larger. The distance of a telescope to the elongated path of the primary particle is later on called impact distance.

The telescopes themselves are imaging which means that they project the light from the showers with a mirror dish to a focal plane, as illustrated in Figure 2.3(b). In the focal plane an array of pixelized light detectors (camera) is sketched. Typical diameters for cameras of IACTs are in the order of 1 m including several hundred to thousand pixels. The inlay of the Figure illustrates the image of an air shower (blue ellipse) in the camera[3]. For the separation of γ-ray and hadronic showers the width of the projected shower is important, so that the minimal shower width has to cover at least two pixels to be resolvable by the camera. A larger field of view enables to see showers with larger offset angle of the shower

[3]An example for a shower image from observational data will presented later in Figure 3.5.

Table 2.1: The table lists current and historical IACT experiments, their geographical coordinates, the height of their sites h, the number of telescopes, the total mirror area A_m of all telescopes, pixels per telescope camera and the radius of the field of view r_f. The table was taken from [61].

Instrument	Lat.	Long.	h [m]	Tels.	A_m [m^2]	Pixels	r_f	
H.E.S.S.	$-23°$	$16°$	1800	4	428	960	$2.5°$	
VERITAS	$32°$	$-111°$	1275	4	424	499	$1.75°$	[63, 64]
MAGIC	$29°$	$18°$	2225	1	234	574	$1.75°$	[14]
CANGAROO	$-31°$	$137°$	160	3	172	427	$2.0°$	[101]
Whipple	$32°$	$-111°$	2300	1	75	379	$1.15°$	[102]
HEGRA	$29°$	$18°$	2200	5	43	271	$2.15°$	[31, 57]

direction to the telescopes line of sight. The size of the detection area using the simplified argumentation above does not change with the field of view. In Summary, the optical properties (e.g. focal length of the telescope's mirror dish, camera layout) of an IACT are the size of the field of view, the resolution of the camera and the mirror area.

With mirror areas in the order of 100 m^2 and opening angles of the pixels in order of $\sim$0.15°, each pixel will see as noise a relative strong flux of photons randomly distributed in time on the dark sky (later discussed as night sky background). On the other hand, the Cherenkov light of a single air shower arrives at the telescope camera within a few nanoseconds, so that the gate for the detection of the Cherenkov light can be restricted to a time window in the order of 10 ns, so that fast light detectors and electronics are required. A trigger system has to be included in the camera to detect the time window. The pixel information have to be stored until the trigger decision is available. The combination of mirror area, the ability to reduce the detection window in the pixels, the trigger conditions and the quality of the shower images determines the lower limit in the γ-rays primary energy that the γ-rays are detectable. The lower energy threshold for IACTs is in the order of 10 GeV to 100 GeV.

An important achievement in the development of the IACT is the stereoscopic IACT technique. Thereby several telescopes are combined to an array of IACTs, so that shower images of the same air shower can be taken from more than one telescope. The maximal spacing between the telescopes that they are able to detect efficiently the same shower is given by the radius of the Cherenkov cone calculated above ($\sim$120 m for zenith observations). The multiple shower images improves the reconstruction of the primary particle (incoming direction, energy) and the ability to separate the hadronic showers from the γ-rays showers. For the data taking process, the trigger systems of the cameras can be combined to an array trigger (for H.E.S.S. "central trigger"), that requested a detection of an air shower in at least two telescopes. The array trigger allows to lower the condition of the camera triggers, as they are not sensitive to NSB anymore.

The IACT pioneer experiment is WHIPPLE. It has detected the first TeV γ-ray source (the Crab nebula) in the late 80s. With a diameter of about 10 m for the mirror dish, the

Figure 2.4: The photograph showing the H.E.S.S. telescopes in the Namibian Khomas Highlands was shot by S. Häffner in March 2010.

telescope is almost as larger as the current IACTs, but it was also equipped with much coarser camera pixels. Another historical IACT experiment was HEGRA. The experiment operated 4 small telescopes as stereoscopic array with a spacing of 100 m between the telescopes [31, 57]. The three recent IACT experiments are H.E.S.S., MAGIC and VERITAS. In table 2.1 the properties of the different experiments are summarized.

2.5 The High Energy Stereoscopic System (H.E.S.S.)

The H.E.S.S. experiment consists of four IACT where the telescopes are mounted in the corners of a square with the side length of 120 m. The diagonal is oriented in north-south direction. The dish of each telescope is equipped with 380 spherical mirror facets with a diameter of 60 cm and a total reflecting area of 107 m^2. The mirror arrangement follows the Davies-Cotton design [36], which allows to use mirrors with the same focal length at each position in the telescope dish. In contrast, a parabolic design requires to vary the focal length of the mirrors with the distance to the dish center. The camera is held by a quadrupole arm in the focal plane 15 m away from the mirror dish. Photomultiplier tubes (PMTs) are used as photo detectors. The camera is equipped with 960 PMTs, where each PMT has a field of view of 0.16°. The field of view of the whole camera covers 5° in diameter. In the front of the PMTs light collectors (Winston cones) are installed, which increases the light yield by covering the holes in the arrangement of the PMTs and which protects the PMTs from lateral scattered light. A detailed description of the optical system of H.E.S.S. is given in [25, 35].

In Figure 2.4 the photograph shows the site of the H.E.S.S. experiment in the Namibian Khomas Highlands. The four telescopes of the first phase of H.E.S.S. are in their park position for the daytime. Hence, the telescopes with their large mirror dishes points to bottom, where their cameras are protected in shelters. In the middle of the photograph, parts of the steal structure for the phase II telescope were already assembled. To the left of the telescopes a large garage covers the control building behind. The control building hosts the control room for the operators of the telescopes, the computer farm and the central

trigger system.

The site lies at 1800 m above sea level and its position on the southern hemisphere allows the observation of TeV γ-ray sources in the inner part of the galactic plane. The location in the desert more than 100 km distant from the Namibian capital Windhoek exhibits two important properties for the operation of an IACT experiment. The climate in the Khomas Highlands is very dry and on average more than 200 days of cloud-free sky per year are expected. And second, the luminous pollution by human influence is relatively small. This is an important point, as the night sky background light (NSB) makes up a major fraction of noise within the Cherenkov light shower images.

Chapter 3

Observation of γ-rays with the H.E.S.S. Telescopes

The observational data of H.E.S.S. consists of a sequence of events, at which each event is composed of up to four images (one for each telescope). For the reconstruction of the event's primary particle, the images are parametrized and compared to MCs. The Chapter will start with a summary to the calibration of the shower image produced by the telescope, afterwards the reconstruction of γ-rays introduced events will be discussed. The event reconstruction together with the calibration yields a list of TeV photons with their incoming direction and primary energy. The quality of the reconstruction (energy bias and point spread function) is characterized at the end of the Chapter.

3.1 Data Acquisition and Calibration

The operation of the full four-telescope H.E.S.S. array started in December 2003. Since then, the data taking for standard observations has proceeded under stable conditions. In particular, the terms of the trigger system (described below) kept unchanged. An absolutely dark sky is required for observations with the H.E.S.S. telescopes, which means that besides the sun also the Moon has to be set below the horizon. The dark time is split into single observation runs with a typical run duration of 28 min. During a run, a target position is tracked on the sky, while the telescopes are aligned parallel to each other and the observation direction. After each of the runs, parts of the hardware (i.e. the PMTs high voltage) are restarted and the tracking position normally changes. In one night, not more than about 2 h to 3 h of observation of the same source are possible before it falls to an altitude too close to the horizon. This fragmentation of the observational data into runs will be important in the discussion of the data analysis. If an individual run has passed quality checks (see below), the observation conditions, in particular the optical efficiency, the camera hardware and the atmosphere will be regarded as stable for the run.

A natural period of 28 days for the data taking is defined by the lunar cycle. No observation is possible in full Moon nights. Beyond the full Moon, the absolute dark time starts in the evening and is gradually extended, until the full night can be used in the middle of one period. Afterwards, the darktime gets shorter each night. The lunar cycles are used as calibration periods over which the measurements for pixel calibrations are averaged.

3.1.1 The Trigger System

The detection of cosmic-ray events requires a trigger system that starts the read out of the telescope cameras with a high temporal accuracy. Cherenkov light produced in an air shower of secondary particles arrives at the telescope cameras within a few nanoseconds, at which the spread in the arrival time between different pixels can be in the order of 10 ns. The trigger system of the H.E.S.S. telescope array consists of two levels, at which the first trigger level is implemented in each camera. Pixels are grouped in overlapping trigger sectors each comprising 64 pixels. If a minimum number of pixels N exceeds a threshold s within one sector and within a coincidence interval t_c, the camera is triggered. The standard trigger conditions are $N \geq 3$, $s \geq 3$ photoelectrons[1] and $t_c = 1.5$ ns [7]. The information of the pixel channels is stored in analogue ring samplers, that contains 128 cells with a sampling rate of 1 GHz [5]. The ring samplers are stopped by the first level camera trigger and wait for a second level trigger decision for the whole telescope array.

The central trigger system (CTS) is the second level of the trigger. It is a fast electronic logic device which receives the camera triggers from the four telescopes via glass fiber. If at least two cameras have triggered within a window of 80 ns [49], the final trigger decision will be made and a command for the camera read out is sent to the telescopes. A read out will take $\sim$0.5 ms. The telescopes cannot generate any new trigger during this dead time. In case that only a single telescope has triggered, the read out in the telescope camera is canceled. The dead time of the telescope is then $\sim$6 μs. The CTS is the hardware implementation of the stereoscopic IACT technique. It has been shown that the CTS suppresses majorly background trigger events generated by single muons passing the telescope dish [49]. The number of event triggers (at least two telescopes) is counted by the CTS. The data acquisition software reads out the event counter every 4 s and provides the mean rate and the deviation from the mean rate of all 4 s time intervals for each run. These two values are called CTS rate and CTS rate fluctuations in the following. The exact definition of the CTS rate fluctuations is given in Section 3.2.2. In the later discussion, these two values will be used to detect clouds on the sky and hazy states of the atmosphere.

[1] Photoelectrons will be discussed in the next Section (Sec. 3.1.2).

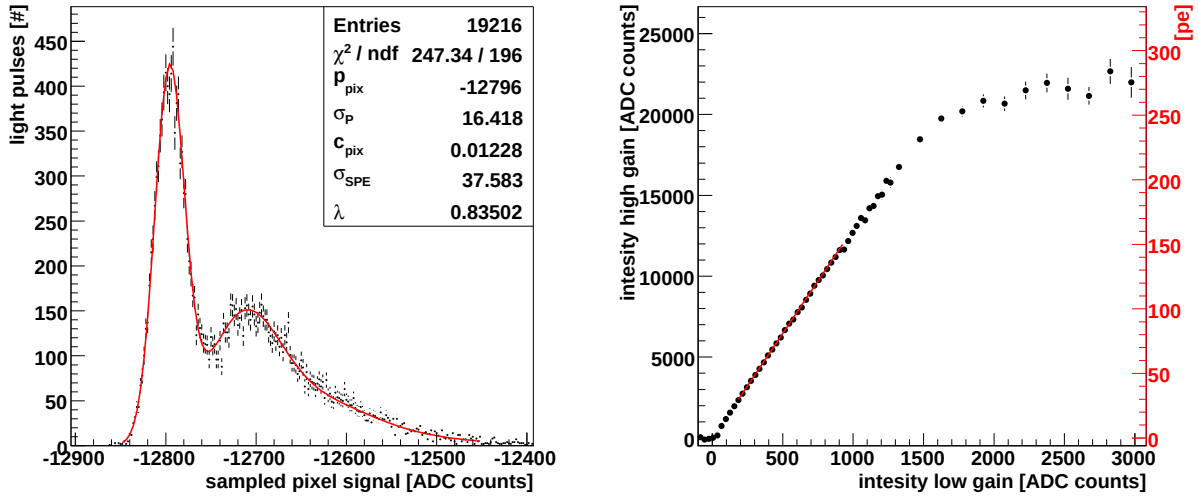

(a) single photoelectrons distribution

(b) amplification ratio

Figure 3.1: The plots show the determination of the conversion factor c_{pix} and the high gain low gain ratio exemplary for one pixel. The applied fit functions (red) are describen in the text.

3.1.2 Pixel Calibration

In the camera read out, the pixels amplitude information which has been stored as charge on the cells of the stopped ring sampler is digitized. The delay between the arrival of the PMT pulse at the sampler and the stop of the sampler is well-known, so that a narrow time window of 16 ns (corresponding to 16 cells) can be selected to integrate the amplitude signal. The aim of the pixel calibration is the conversion of the measured pulse m_{pix} in ADC counts from sampling process to a comparable quantity for the amount of Cherenkov light from a particle shower. In each pixel, the PMT signal is split up into a line with a high amplification and a line with a low amplification. For the high amplification the calibrated value h_{pix} is determined by:

$$h_{pix} = f_{pix} \cdot \frac{m_{pix} - p_{pix}}{c_{pix}} \tag{3.1}$$

In a first step, the electronic pedestal p_{pix} is subtracted from the measured pulse m_{pix}. The electronic pedestal is the measured value, when the PMT is supplied with high voltage and read out without detecting any photons. A major fraction of pixels in the observation runs contains no Cherenkov light from the triggering particle shower, so that the electronic pedestal can be measured in situ with observational data by averaging over a sufficient number of events. The in situ measurement is required, because p_{pix} varies from run to run (i.a. with the temperature of the electronics).

The conversion factor c_{pix} between the number of photoelectrons (pe) released by a light pulse at the photo cathode of the PMT and the m_{pix} value is determined in calibration

runs. Within single photoelectrons (SPE) runs, the camera is illuminated with nanosecond light pulses with a brightness that will convert a single photon into a photoelectron per pixel in about 30 % of all pulses. One can separate the position of the electronic pedestal (no converted electrons) from the peak with a single electron in the m_{pix} distribution by collecting several thousand light pulses. An example for the single photoelectrons distribution is shown in Figure 3.1(a). The peak on the left side of the SPE distribution is formed by events that measured only the pedestal. The broad peak in the middle of the distribution corresponds to the events, where one photon has been converted to a pe. The tail to the right is a superposition of multi-pe conversions. The red line models the SPE distribution by folding the components of a Poisson distribution in the number of photoelectrons n with Gaussian functions (Eqn. 6 in [5]):

$$g\left(x, \bar{x}, \sigma_x\right) = \frac{1}{\sqrt{2\pi} \cdot \sigma_x} \cdot \exp\left(-\frac{1}{2} \cdot \frac{(x-\bar{x})^2}{\sigma_x^2}\right) \tag{3.2}$$

The pedestal peak (the $n = 0$ component of the Poisson distribution) is folded with a Gaussian around the pedestal position p_{pix} with the electronic width σ_{pe}. As there is no amplification process ongoing in the PMT during a pedestal measurement, the origin of electronic width is the noise in the electronic components (i.e. signal amplifier, ring sampler, PMT's anode). For the single and n photoelectron peaks, the width σ_n consists of the fluctuation in the amplification of a single photoelectron σ_{sge} in the PMT and σ_{pe}:

$$\sigma_n = \sqrt{\sigma_{pe}^2 + n \cdot \sigma_{sge}^2} \tag{3.3}$$

The final fit function in the digitized output channel m is spe, where N is a normalization constant depending on the number of recorded light pulses:

$$spe\left(m\right) = N \cdot e^{-\mu} \cdot g\left(m, p_{pix}, \sigma_{pe}\right) + N \cdot \sum_{n=1}^{\cdots} \frac{e^{-\mu} \cdot \mu^n}{n!} \cdot g\left(m, m_{pix} + \frac{n}{c_{pix}}, \sigma_n\right) \tag{3.4}$$

To correct for different quantum efficiencies of the PMTs, as well as the collection efficiencies of the Winston cones, a flat field coefficient is determined. For this purpose, the camera is uniformly illuminated with a laser. The laser intensity can be set to a stable value (within 5 %) from 10 pe to 200 pe in five steps [5]. The flat field coefficient of a pixel f_{pix} is the ratio of the mean signal of all pixels to the observed signal:

$$f_{pix} = \frac{\langle s_i \rangle_{pixels}}{s_{pix}} \tag{3.5}$$

The SPE and the flat field runs should be produced every second night. The runs of one calibration period (defined by the lunar cycle) are merged in one coefficient per pixel. The merging procedure is outlined in [5].

Each pixel provides a second amplified channel with a low gain l_{pix}. The lower amplified channel does not allow separating a single electron peak. Therefor the conversion is done with the SPE coefficient c_{pix} of the first channel together with the amplification ratio r_{pix}:

$$l_{pix} = f_{l,pix} \cdot \frac{m_{l,pix} - p_{l,pix}}{c_{pix}} \cdot r_{pix} \tag{3.6}$$

For the low gain channel separate pedestals $p_{l,pix}$ and flatfield coefficient $f_{l,pix}$ are required. The amplification ratio is determined from scatter plots of l_{pix} to h_{pix} from normal observation runs. In particular, the images of bright showers are required to describe the complete overlapping dynamic range. The runs of a complete calibration period are used. An example is shown in Figure 3.1(b), where the amplification ratio is determined in a linear fit in the range from 30 pe and 150 pe. The high gain is used up to 150 pe, from 150 pe to 200 pe the pixel amplitudes are given by a combined measurement from the high gain and the low gain channel. For signals above 200 pe the high gain channel becomes saturated and the amplitudes are determined from the low gain. The dynamic range of the low gain channel ends at about 2000 pe (Fig. 3 of [5]).

Pixels, where hardware problems with the high voltage or the analogue ring sampler occur, will be marked as broken and their signal will be removed from the analysis. Another reason to discard a pixel as broken is a high noise rate of the PMT. The noise is measured either with the width of the electronic pedestal or with the current of the high voltage supply. Noisy pixels are the ones in which the photo electron rate exceeds 340 MHz for the high gain channel or 300 MHz for the low gain channel. There are several ratings for the number of problematic pixels available in a database. In this work, the number of broken pixels is derived for each observation run from the fully calibrated data. A pixel which does not take part in any of the about 10^5 events[2] of a run is counted as broken. That is for example that a pixel is not counted as broken where no high gain intensity can be determined but a low gain intensity is available.

3.1.3 Absolute Intensity Calibration with Shower Images of Single Muons

The pixel calibration does not capture the status of the telescope's mirrors nor the atmosphere. O. Bolz [30] implemented a method to measure the mirror reflectivity and the transmissibility of the lower atmosphere. He used images of muons crossing the mirror dish of a telescope. The cone of Cherenkov photons, which has been generated by the muon, is seen in the camera as a well-defined ring. The number of expected photoelectrons N_e in each pixel can be derived in dependence of four geometric parameters: the opening angle of the muon's Cherenkov light cone θ_C (Eqn. 2.1), the impact point of the muon in the telescope's mirror dish and the inclination angle of the muon's path to the telescope's line

[2]The 10^5 events are γ-like events counted after event-selection cuts. The γ / hadron separation will be discussed below in Section 3.3.4.

of sight. For the details of the ring analysis see Chapter 3 in Reference [30] and references therein. The muon efficiency ε_μ is the ratio of the seen photoelectrons in a ring image to the number of expected pe. The optical efficiency is the detection probability that an incoming photon following a ray, on which it will be reflected by the mirrors to the camera plane, is detected by a PMT. The measurement of ε_μ is the standard approach for the estimate of the optical efficiency. The following effects contribute to the efficiency:

The Shadow of the camera steel structure and the bracing struts blocks about 10 % of the incoming photons [12].

The Mirror Reflectivity within the typical Cherenkov wavelength range was between 80 % and 85 %, when the mirrors were mounted to the telescopes in 2003 [75, 99]. Over the last six years (i.e. since the installation), the reflectivity decreased to an average value of ∼60 %.

The light collector efficiency (Winston Cones) has been evaluated with ray tracing software [73] to be ∼75 %.

The quantum efficiency of the PMT that a photon reaching the cathode of a PMT will be converted into a SPE is 30 % for λ ∼350 nm. The average quantum efficiency weighted with the wavelength distribution of Cherenkov light from air showers is ∼15 %. These numbers base on measurements with four PMTs [71].

The Transmission Efficiency in the Atmosphere for the Cherenkov light between its emission induced by the muon and the detection at the PMT is larger 90 %. The muon analysis is only affected by the lower atmosphere close to ground level. Photons of the cone which are emitted several hundred meters above the telescopes will pass the telescope beyond the mirror dish. The maximum emission height above the telescopes for Cherenkov photons to be reflected by the mirrors and detected by a PMT is 600 m. This height is reached, if the muon hits the mirror dish in the center and if its incoming direction is parallel to the line of sight.

For each observation run and telescope, the optical efficiency is derived as the muon factor ε_μ. This is possible, because there are about 200 images containing a full muon ring in a 28 min observation, although muon rings are events which are restricted to one telescope, so that the hardware trigger (CTS) suppresses most of them. Unfortunately, the number of ring images decreased to ∼75 images per telescope for runs between 2007 and 2009. The reason for the decrease of muon ring images is unclear at the present. It will be assumed here that the number of photons in a muon ring image and the muon efficiency determined with Bolz's method are not affected. The optical efficiency will be used for the TeV γ-ray analysis below. The primary energy of TeV photons is reconstructed based on the number of pe in the picture of the shower (image size) and the pe number is corrected with ϵ_μ (see Section 3.3.3). A decrease of the optical efficiency will also reduce the hardware trigger rate of the CTS. The hardware trigger is a criterion to detect haze in

the atmosphere. An estimation of the trigger rates in dependence of the optical efficiency will be discussed in the next section.

3.2 Data Quality and Run Selection

The observational data are preselected according to parameters of the individual runs. Systematics in the estimation of background events and in the reconstruction of the γ-ray flux due to partial hardware failure and uncertainties regarding the atmospheric conditions are reduced by this approach. A set of selection criteria has been described by the H.E.S.S. collaboration together with the γ-ray flux from the crab nebula [7] in 2006. The selection criteria suggested here follow the original H.E.S.S. criteria. However, they are slightly modified in order to take into account the aging of the hardware:

The fraction of broken pixels in each telescope is limited to 10 % of all pixels.

The atmosphere can be in a state that reduces the light transmission coefficient dramatically. The runs which are affected by such a hazy atmosphere should be rejected, if their CTS rate is smaller than 60 % of an estimated trigger rate (Sec. 3.2.1).

A partially cloud-covered sky is detected via the CTS trigger rate fluctuation. Runs with a relative CTS rate fluctuation larger than 5 % are affected by clouds (Section 3.2.2) and are rejected from the analysis.

Apart from these quality criteria, two further restrictions will be imposed on the runs that will be used for background rate determination and systematic studies:

All four telescopes have to take part in a run. Nevertheless the event reconstruction, the data analysis and the approaches for systematic studies which are presented here will in principle also work for runs with three telescopes.

The observation time of a run should be between 1650 s and 1700 s. With this selection criterion, runs that have been stopped by the operators upon recognizing a problem are discarded.

3.2.1 Influence of Atmospheric Variations

The atmosphere is an important part of IACT detectors for the indirect measurement of primary γ-ray photons. The main effects are: A denser atmosphere will provide more target material for the primary particle to start the cascade of secondary particles. The point of first interaction and the development of the shower take place at a larger height above the ground. A second effect is, that the density profile between the shower and the telescopes determines the atmospheric transmissibility for the Cherenkov light. K.

Table 3.1: The observation passing the selection criteria are summarized in intervals according to their optical efficiency. In the first column, intervals in the optical efficiency are defined to group the available H.E.S.S. observation runs. The given dates contain at least 80 % of the runs in the interval. $\langle\epsilon_\mu\rangle$ is the average efficiency of the runs in each interval. The trigger rate parameter a_{ϵ_μ} is the extrapolated CTS rate to a zenith angle of 0° for the runs of the interval. It has been determined in a fit (see text).

interval in ϵ_μ	runs			$\langle\epsilon_\mu\rangle$	a_{ϵ_μ} [Hz]
≥ 0.08775	595				
$[0.07735, 0.08775]$	784	2004-06-21	2005-05-29	0.08214	251.5
$[0.07355, 0.07735]$	767	2005-05-01	2006-04-05	0.07556	222.6
$[0.07155, 0.07355]$	811	2005-08-28	2007-02-14	0.07243	222.6
$[0.07005, 0.07155]$	747	2006-04-30	2007-05-11	0.07082	219.7
$[0.06775, 0.07005]$	823	2006-07-26	2007-11-08	0.06909	199.3
$[0.06555, 0.06775]$	733	2007-07-11	2008-10-22	0.06652	198.7
$[0.06405, 0.06555]$	737	2007-08-22	2008-12-30	0.06480	190.7
$[0.06095, 0.06405]$	789	2008-08-06	2009-08-20	0.06286	186.9
< 0.06095	207				

Bernlöhr has investigated the influence of different atmospheric models in Monte Carlo (MC) studies [22] for γ-rays air showers. He claims a loss of 60 % intensity of the Cherenkov light on the ground between the most efficient atmospheric model ("arctic winter") and the "tropical" model. Seasonal changes have been derived with a "midlatitude" model and their differences are quoted to be $\sim$20 %.

A commercial lidar[3] system VAISALA CT25K is installed on the H.E.S.S. site to monitor the atmosphere. It sends out laser pulses and measures the aerosol density profile as backscatter intensity over the runtime of a laser pulse. The lidar is mounted on a pan tilt unit and follows the observation target of the Cherenkov telescopes during the observation runs. It has been proven for an observation campaign of the H.E.S.S. point sources Sagittarius A* [3] and PKS 2155-304 [4] in August 2004, that a higher aerosol density will lead to an underestimate of the γ-ray particle flux and while the CTS rate will be reduced simultaneously [78]. The VAISALA CT25K lidar has some disadvantages: The laser operates in the IR regime at 905 nm instead of Cherenkov light wavelength and the sensitivity range of the PMTs. The laser pulses reach a nominal height of 7.5 km, which is insufficient to reach the region of the shower cascade. Due to hardware failures, the lidar did not operate continuously and it has been stopped completely in late 2007. By now, two stronger lidar systems have been installed on site and the optical telescope ATOM can also provide atmospheric monitoring [54, 55]. However, these efforts are ongoing work and there is no correction procedure for atmospheric variability available from these instruments as yet.

A quality selection criterion is introduced here, which can detect the atmospheric variations and discard runs with unusual low trigger rates. Therefor an estimated trigger rate

[3]Lidar stands for "Light detection and ranging".

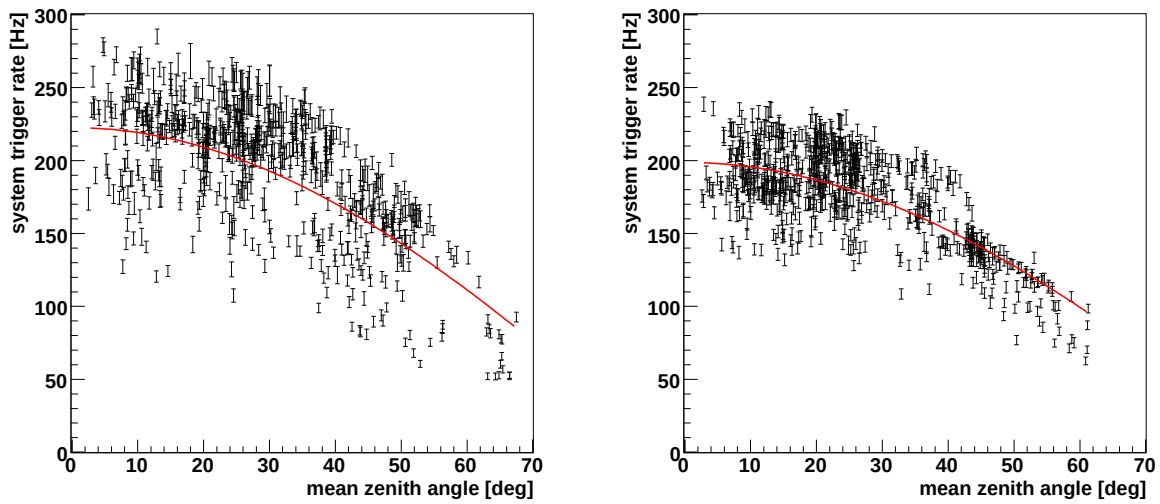

(a) ϵ_μ ∼0.07243 (b) ϵ_μ ∼0.06652

Figure 3.2: The dependence of the four-telescope system trigger (CTS) on the zenith angle are shown here for two optical efficiencies. Each bar shows an observation run which fulfills standard quality criteria. The red line is a cosine function.

for the full four-telescope system in dependence of the zenith angle φ_Z and the optical efficiency ϵ_μ is defined. This rate can be compared to the actual CTS rate. A variation of this approach is discussed in Section 4.3, where a relative calibration between different observation runs is described based on the trigger rate estimation. For the zenith angle dependence of the CTS rate R, it is assumed that the rate is proportional to the cosine of φ_Z. Of course, this is a coarse simplification of the real situation, as several length scales in the development of a shower's Cherenkov light cone depend on $\cos(\varphi_Z)$: Tilting a shower with respect to the zenith, the cross section area of the cone with ground will change with the cosine. The path through the atmosphere and thus the absorption of Cherenkov light is increased. On the other hand, the path of the particle shower in a less dense upper atmosphere is prolonged.

There are about 7000 observation runs which fulfill the selection criteria discussed before. These runs are grouped into eight intervals according to their optical efficiency ϵ_μ. The intervals are summarized in Table 3.1 and the their bounds are chosen such that each of them contains ∼800 runs. Figure 3.2 shows two of these efficiency bands. Every run is marked with an error bar corresponding to the CTS rate fluctuations. The red lines are the results of a fit:

$$R_{\epsilon_\mu}(\varphi_Z) \quad = \quad a_{\epsilon_\mu} \cdot \cos(\varphi_Z) \tag{3.7}$$

where a_{ϵ_μ} is the extrapolated trigger rate for an observation at zenith ($\varphi_Z = 0°$). The fit is a very coarse description of the trigger rates within the intervals (as also seen in Fig.

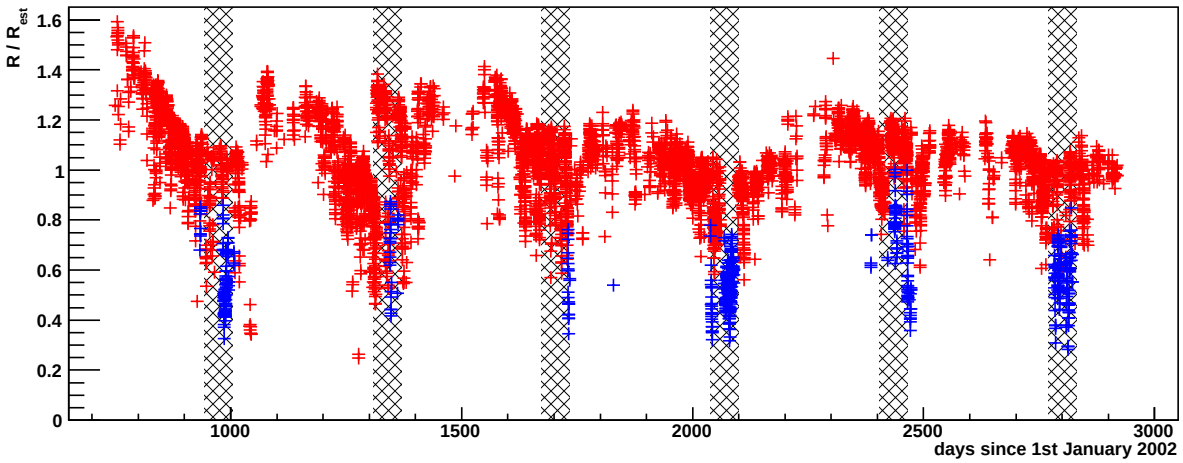

Figure 3.3: The plot shows the ratio of the CTS rate R to the estimated trigger rate R_{est}. Each cross is an observation run with the full four-telescope array. For the runs marked by blue crosses, the atmosphere has been claimed as hazy.

3.2), although the dependency on ϵ_μ of the trigger rate parameter a_{ϵ_μ} follows the expected behavior. The first-level triggers of the cameras reject more air shower events, when the number of detectable pe drops with the efficiency. The estimator for the CTS rate in zenith angle and optical efficiency can be derived by writing the zenith rate factor a_{ϵ_μ} as a linear function in ϵ_μ:

$$R_{est}\left(\varphi_Z, \varepsilon_\mu\right) \quad = \quad p_a \cdot \frac{\varepsilon_\mu}{0.07249} \cdot \cos(\varphi_Z) \tag{3.8}$$

with the parameter $p_a = 216.7$ Hz. One has to note, that a single two-dimensional fit in φ_Z and ϵ_μ with the free parameter p_a over the unbinned runwise rates results in a comparable estimator.

The rate estimator can be used as tool in a systematic search for runs featuring an unusual CTS rate. All observation runs fulfilling the selection criteria (Sec. 3.2) are represented in Figure 3.3 with a cross. The ratio of the actual CTS rate R and the estimated rate R_{est} is drawn over the observation date of the run. The hatched areas mark August and September of each year, starting in 2004 with the first hatched area and ending in 2009 with the last one. One can see that the ratio is stable in time within ± 30 % over all years of data taking. Moreover, an annual periodicity can be seen. R/R_{est} rises to a high value just between October and February and decreases over the rest of the year. In the first months of data taking (end of 2003 / beginning 2004) the CTS rate exceeds the estimated rate by more than 30 %. A fraction of Vela X H.E.S.S. observations were taken in this time. The consequences will be discussed in Section 6.1. For an interpretation of R/R_{est} ratio with regard on the atmospheric conditions, an interesting group of runs possess a small ratios below 0.6. These runs are typically observed in the marked months August and September. Most of the runs are drawn with a blue cross which indicates that

the operators on the H.E.S.S. site rated the atmosphere as hazy in their nightly report. The hazy atmospheric conditions are revealed to humans as red horizon at the Sun set and the stars appear smeared out on the uncovered night sky. The accurateness and awareness of the operators varies, so that not all runs influenced by a hazy atmosphere have been identified and reported by the operators. A cut on less than 0.6 on the ratio of the CTS rate to the estimated rate will reject the most affected runs.

This Section can be summarized as follows: The estimator $R_{est}\left(\varphi_Z, \epsilon_\mu\right)$ of the CTS rate introduced in Eqn. 3.8 describes the trigger rates from the beginning of four-telescope operations in 2003 until now (early 2010). It is obviously, the rate estimator cannot provide a complete model of the CTS rate. However, the estimator is able to identify runs observed under bad atmospheric conditions. As it will be discussed in the next paragraph, a hazy atmosphere and a cloud-covered sky can occur independently of each other and both phenomena can be detected by a specific run selection criterion.

3.2.2 Cloud Detection

Clouds are an additional weather phenomenon to be considered for the quality selection of runs. They can be detected as fluctuations in the CTS rate. This is illustrated in Figure 3.4(a), where the CTS rate is plotted over the time for three different runs. The red points show a run (No. 55430) with good data quality, including a clear sky. The error bars were determined assuming Poisson statistics for the triggers in the time interval of 16 s per data point. The black points are taken from a run (No. 55259), where a single cloud is passing the field of view. The cloud comes into the field of view about 800 s after the run start and leaves it 500 s later. A linear base line function $b\left(t\right)$ is used, which corrects the change of the zenith angle during the run. The base lines are included in the plot as black broken lines. The CTS rate fluctuation is the quadratic sum of deviations between the CTS rates and the base line calculated in 4 s intervals:

$$\delta_R \;=\; \frac{1}{\langle b\left(t\right)\rangle_t} \cdot \sqrt{\frac{\sum\limits_{t \in bins} \left(R_t - b\left(t\right)\right)^2}{\#bins}} \tag{3.9}$$

In Figure 3.4(b), the relative CTS rate fluctuations σ_R/R are plotted against the rate ratio R/R_{est}. Each cross represents an observation run. The plot includes two black lines at $R/R_{est} = 0.6$ and $\sigma_R/R = 0.05$. The lines separate the runs into four sectors labeled with capital letters. The main fraction of the runs populates the sector A with a spill-over into to sector B. These runs are not affected by clouds. The population is smeared out into a tail in the direction of higher trigger rate fluctuations. Runs with a relative CTS rate fluctuation larger than 0.05 (sectors B and D) will be rejected in the quality run selection. The runs included in sector C will be discarded due to a hazy atmosphere. Hence, only runs in sector A fulfill the run selection criteria and will be used for data analysis.

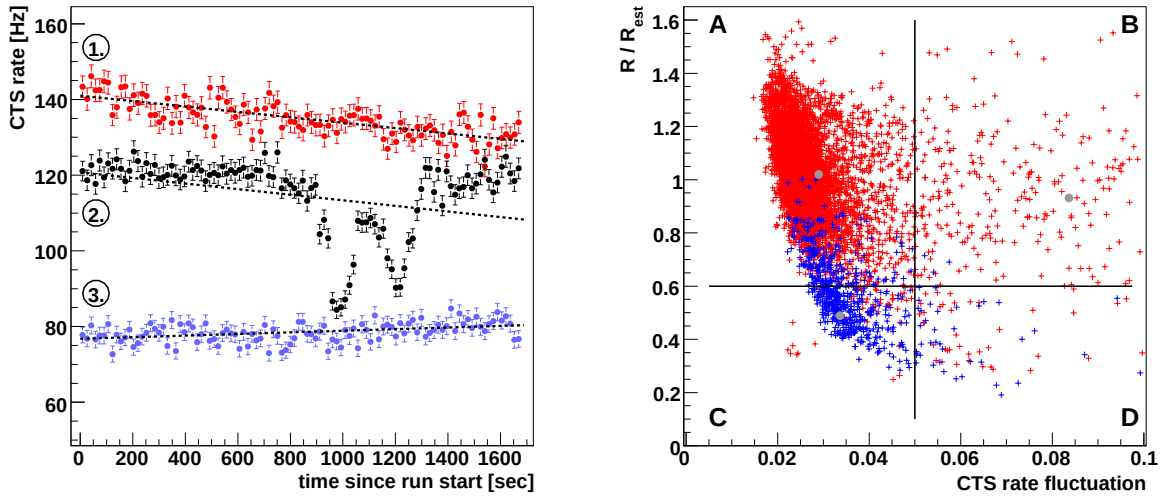

(a) cloud detection

(b) hazy atmosphere versus cloud detection

Figure 3.4: a) The development of the CTS rate over a full run duration is plotted for three exemplary runs. The sky was clear for the first run. The second run is affected by a passing cloud and the atmosphere in the observation of the third run has been identified as hazy. b) The Ratio R/R_{est} is plotted over the CTS rate fluctuation for all available four-telescope runs. The black horizontal and vertical lines show the proposed run selection criteria for R/R_{est} and the CTS rate fluctuation. The atmosphere has been claimed hazy for the runs marked with a blue cross. The three runs from a) are indicated with gray dots.

3.3 Event Reconstruction and Background Suppression

The reconstruction of the characteristics of the primary particle will be presented in this Section. Of interest are the incoming direction, the type (photon or hadronic particle) and the energy under the assumption, that the particle is a photon. The introduced reconstruction method requires that at least two images from different telescopes of each shower are available.

The reconstruction of the primary particle relies on the comparison between the shower image and Monte Carlo simulations. A set of MC has been produced with the CORSIKA software package [56] and K. Bernlöhr's telescope simulation *sim_hessarray* (for a detailed documentation see [23]). In the simulation the observation direction of the telescopes is fixed and a γ-ray point source is set on the sky with a defined offset ψ to the observation direction. The intercept point of the incoming direction of the primary particle with the ground is called impact point. The impact point is scrambled relative to the telescope positions within a radius of 1000 m. The energy distribution of the γ-rays follows a power law with an index of 2.0. The MC are available for different zenith angles (0°, 20°, 30°, 40°,

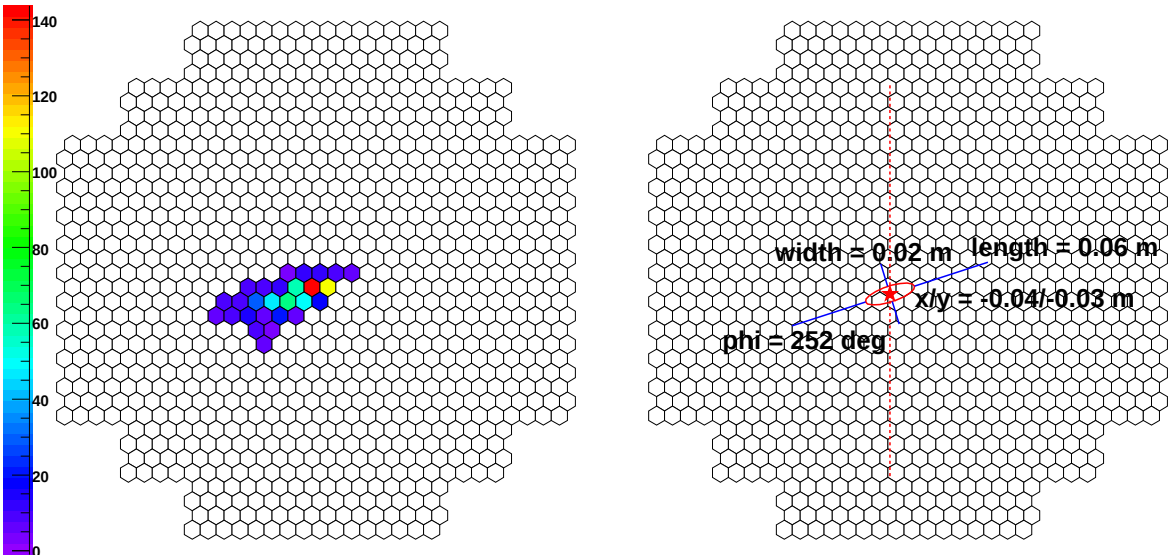

Figure 3.5: An exemplary shower image taken by one of the cameras (*Run: 37243, Bunch: 1934, Event: 195, 2nd telescope*) is presented. The image has been cleaned with tail cuts (see text). The intensity scale is pe. The resulting ellipse using the first and second moments of the intensity distribution is drawn on the right side.

45°, 50°, 55°, 60°, 65°, 67°, 69° and 70°), with the point source at six offset positions (0.0°, 0.5°, 1.0°, 1.5°, 2.0° and 2.5°). Sets of MC are done for two different azimuthal directions, where the telescopes are aligned either to the south or to the north. The mirror reflectivity is assumed to be 70 %.

3.3.1 Hillas Parameters

In 1989, A. M. Hillas introduced a set of simple geometric parameters [60] for the data analysis of the IACT pioneer Whipple. He describes the shower image as an ellipse using the second moments of light intensity distribution in the image. This approach is often called "Hillas analysis".

In the H.E.S.S. analysis the calibrated shower images are cleaned with a tail-cut. All pixels i below an amplitude A_i of 5 pe are neglected. In addition, all pixels below an amplitude of 10 pe are rejected, if no neighboring pixel exceeds 10 pe. Figure 3.5 shows an example for such a cleaned image. The following parameters are obtained from each shower image:

The Image Amplitude is the sum of detected photoelectrons over the remaining pixels after tail cuts:

$$s = \sum_{i}^{N} A_i \tag{3.10}$$

The Center Position of the shower in the camera plane is the amplitude centroid. The coordinates of the pixel i within the camera plane are x_i and y_i and the coordinates (x, y) of the centroid are defined as

$$x = \frac{\sum_i^N x_i \cdot A_i}{s} \tag{3.11}$$

$$y = \frac{\sum_i^N y_i \cdot A_i}{s} \tag{3.12}$$

The Length and Width of the ellipse:

$$len = \sqrt{\frac{\sigma_{xx}^2 + a^2 \cdot \sigma_{yy}^2 + 2a \cdot \sigma_{xy}}{1 + a^2}} \tag{3.13}$$

$$wid = \sqrt{\frac{\sigma_{yy}^2 + a^2 \cdot \sigma_{xx}^2 - 2a \cdot \sigma_{xy}}{1 + a^2}} \tag{3.14}$$

The Orientation of the amplitude distribution. ϕ is the angle (clockwise) between the top of the camera and the major axis of the amplitude distribution:

$$\phi = \arctan(a) \tag{3.15}$$

These relations were already used by Whipple [102], where also the variable a is defined for simplification. The second moments σ_{xx}, σ_{xy}, σ_{yy} and a are defined as follows:

$$\sigma_{xx}^2 = \frac{\sum_i^N x_i^2 \cdot A_i}{s} - x^2 \tag{3.16}$$

$$\sigma_{xy} = \frac{\sum_i^N x_i \cdot y_i \cdot A_i}{s} - x \cdot y \tag{3.17}$$

$$\sigma_{yy}^2 = \frac{\sum_i^N y_i^2 \cdot A_i}{s} - y^2 \tag{3.18}$$

$$a = \frac{\sigma_{yy}^2 - \sigma_{xx}^2 + \sqrt{\left(\sigma_{yy}^2 - \sigma_{xx}^2\right)^2 + 4\sigma_{xy}^2}}{2\sigma_{xy}} \tag{3.19}$$

As example, the reconstruction of a cosmic-ray event from a shower image will be demonstrated. The Hillas parameters of the example event are given in Table 3.2. In the corresponding observation run, the telescopes pointed to RA = $08^h40^m08.64^s$, Dec = $-45°36'00''$ (J2000.0) which is 0.9° to the east of the Vela X TeV flux centroid (see Sec. 6.4.1). The image amplitudes of the event are uncommonly large with $s > 600$ pe in all four telescopes, whereas the event has been chosen to exhibits relative bright amplitudes in all shower images.

Table 3.2: The table demonstrate the reconstruction of the example event (*number: 195, bunch: 1934, run: 37243*). The Hillas parameters derived from the four shower images are presented in the first part of the table. The second part gives the expected values and their standard deviation for the energy and shape read from MC based lookup tables. The lookup values depend on the image amplitude and the impact distance of the shower to the telescope.

telescope	*tel*		1	2	3	4
image amplitude	s	[pe]	610.1	638.2	684.5	605.6
center horizontal	x	[m]	0.150	-0.046	0.121	0.307
center vertical	y	[m]	0.160	-0.032	-0.192	-0.079
orientation	ϕ	[deg]	1.6	252.5	187.9	120.2
length	len	[cm]	6.291	6.791	5.908	6.686
width	wid	[cm]	2.609	1.961	2.106	2.078
impact distance	i	[m]	86.19	120.51	87.22	49.43
muon correction	ε_μ / ε_{MC}		0.965	1.052	0.959	1.021
lookup energy	e	[TeV]	0.979	1.087	1.043	1.016
	σ	[TeV]	$\pm$0.289	$\pm$0.246	$\pm$0.181	$\pm$0.243
lookup length	len_{ex}	[cm]	5.674	6.301	6.739	6.233
	σ_{lex}	[cm]	$\pm$1.756	$\pm$1.391	$\pm$1.444	$\pm$1.386
lookup width	wid_{ex}	[cm]	2.610	2.145	1.845	2.131
	σ_{wex}	[cm]	$\pm$0.419	$\pm$0.323	$\pm$0.272	$\pm$0.324

3.3.2 Direction Reconstruction

The major axis in the camera image defines the propagation direction of the particle shower in the sky. Following this idea, the original direction of the primary particle is part of the projection of the major axis to the sky. With stereoscopic IACTs the original direction is derived by intersecting the major axes obtained from two images of the same shower. If there are more than two images from a particle shower available, a weighted mean of the intersecting points is derived. The intersection is used in an Cartesian plane perpendicular to the observation direction, where the major axis can be described with linear expressions. The major axis of each image is transferred from the focal plane to the intersection plane, while the central positions (corresponding to the observation direction) are overlaid.

The direction reconstruction for the example event (Tab. 3.2) is sketched on a sky map (Fig. 3.6(a)). In contrast to the intersection plane, the sky map will include in the exact mathematical description a slight bending due to the usage of spherical coordinates. This bending is neglected in the map. The red points are the transferred centroids (Eqn. 3.11 and 3.12) from the four shower images. The lines indicate the direction of the major axes. The six intersection points are plotted in blue. Remarkable, one of the intersection points is shifted $\sim$0.5° to the west, while the other five are located near the final reconstructed direction (green point). This final direction is calculated as weighted mean value of the six

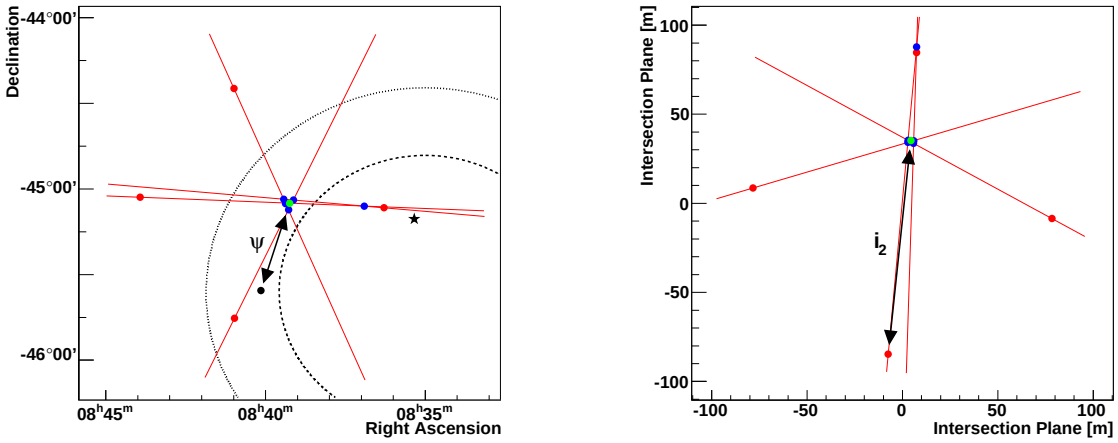

(a) particle direction

(b) impact point

Figure 3.6: a) reconstruction of the original particle's direction (*Run: 37243, Bunch: 1934, Event: 195*) b) The impact point and distance is derived in the plane perpendicular to the observation direction. In the sky map, the red points are the projected amplitude centroids. The lines indicate the direction of the major axes. The blue points are the intersection points of the axes and the green point is the reconstructed direction of the event. The black dot is the observation direction and the event's offset to this direction ψ is illustrated with the arrow. The position of the Vela X pulsar is indicated by a black star. The broken (dotted) black circle shows the integration radii in the Vela X analysis (see Chapter 6). For the reconstruction of the impact point, the red points are the projected positions of the telescopes. The remaining elements use the same color code as in the sky map. The impact distance for the 2^{nd} telescope i_2 is sketched with an arrow.

intersection points. The weighting factor consists of three factors ($w = w_1 \cdot w_2 \cdot w_3$):

$$w_1 = \sin(\Delta\alpha) \tag{3.20}$$

where $\Delta\alpha$ is the intersecting angle between the two axes. w_1 disfavors intersection points with large uncertainties due to almost parallel major axes as in the given example, the point shifted to the west.

$$w_2 = \frac{1}{\frac{1}{s_1} + \frac{1}{s_2}} \tag{3.21}$$

The second factor w_2 preferably selects intersection points from shower images in which a large image amplitude s (Eqn. 3.10) has been seen. The length *len* (Eqn. 3.13) over width *wid* (Eqn. 3.14) ratio allows to estimate the distance between the shower ellipse in the images and the projected particle direction (for details see [13, 62]). The factor w_3 considers that a nearer shower will contribute more accurately to the final direction:

$$w_3 = \frac{1}{\frac{wid_1}{len_1} + \frac{wid_2}{len_2}} \tag{3.22}$$

A comparison of seven direction reconstruction algorithms can be found in [62]. The method described above corresponds to algorithm 3 within the reference. Although in the algorithm here, it is left out to estimate a distance of the shower centroid to the reconstructed direction using the length-width ratio.

Reconstruction of the Impact Point

The impact point is the intersection of the incoming direction of the primary particle with the ground. It is used in the energy reconstruction and in the γ / hadron separation, where the image parameters are compared to MC generated parameters. The parameters depend on the distance of the shower axis to the observing telescope also referred as impact distance. The reconstruction method for the impact point and distance works analogous to the direction reconstruction. A plane perpendicular to the shower direction allows to fix the position of the shower to the telescope positions. The orientation of the major axis and the projected telescopes positions define the intersection lines in this plane. The impact position is again determined as the weighted mean of the intersection points of these lines, where the weighting factor only consists of w_1. The Figure 3.6(a) shows the reconstruction of the impact point for the example event. The final impact point on the ground is calculated by reverting the projection to the intersection plane from the mean intersection point. The impact parameter of an event to a telescope is defined as the distance between the shower axis and the telescope.

3.3.3 Energy Reconstruction

The energy reconstruction is based on the comparison of image parameters with MCs. Therefor lookup tables are filled with the simulated energy e_{tel} of γ-ray MC events. The lookups depend on the image amplitude and the impact distance of the shower axis to the telescope. The injected γ-ray events follow the power law used to generate the MC and in addition are selected by the simulated CTS and camera trigger. As a consequence the lowest energies are overlaid in the corresponding impact parameter / amplitude size bin by mid energy events, so that below a certain threshold the reconstructed energy overestimates the true energy. A separate lookup value for each zenith angle and source offset to the observation direction ψ is available. Energy values between the fixed zenith and offset angles defined in the MC simulations are extracted from the lookups using a linear interpolation analogous to the procedure discussed below for the effective areas (Eqn. 3.32 to 3.39). Apart from the lookups for the energy value, there is a second set of tables providing the standard deviations of the mean energy depending on the four introduced parameters. Figure 3.7 shows the tabulated values for the mean energy and its standard deviation. The parameters of the example event for the shower image from the 2^{nd} telescope are indicated with arrows. The γ-like energy reconstructed from the 2^{nd} image is 1.1 ± 0.3 TeV (see also Tab. 3.2).

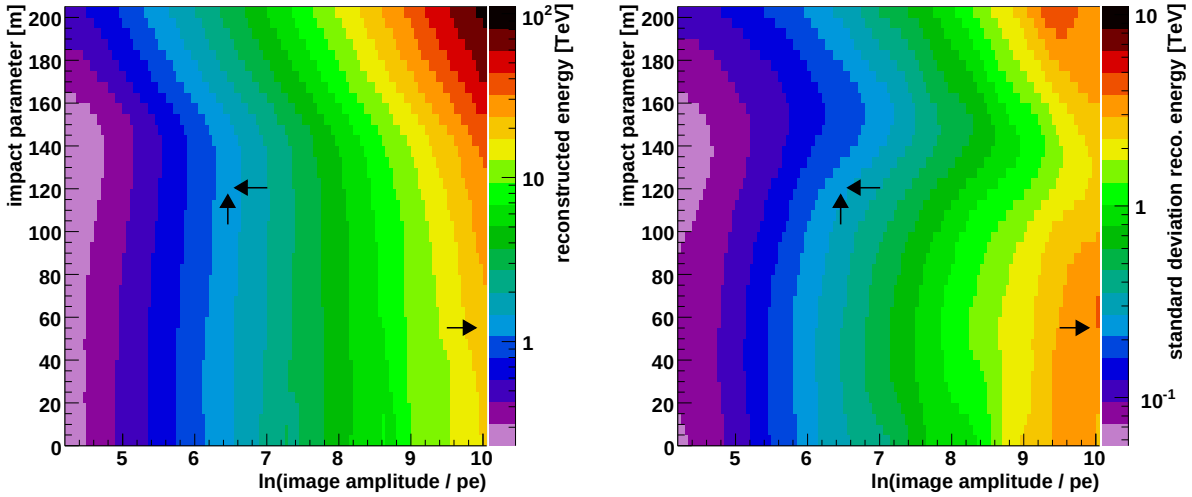

(a) lookup for primary energy

(b) deviation of the primary energy

Figure 3.7: These lookups are produced from MC for γ-ray events at an offset to the observation direction of $\psi = 0.5°$ and telescopes pointing to the south at a zenith angle of $\varphi_Z = 30°$. The arrows indicate the image parameter of the example event (*Run: 37243, Bunch: 1934, Event: 195, 2nd telescope*) and the read out energy / standard deviation on the color bar.

The information from the different telescopes is merged by averaging the individual energies e_{tel}, weighted with their standard deviations accuracy σ_{tel} estimated from the second set of lookups:

$$E_r = \frac{\sum_{tel=1}^{4} e_{tel} \cdot \frac{\varepsilon_{\mu,tel}}{\varepsilon_{MC}} \cdot \frac{1}{\sigma_{tel}^2}}{\sum_{tel=1}^{4} \frac{1}{\sigma_{tel}^2}} \tag{3.23}$$

where $\varepsilon_{\mu,tel}$ is the muon efficiency for the respective telescope determined for each observation run. ε_{MC} is the muon efficiency derived from particular MC simulation, which carries on single muons from hadronic showers to the simulated telescope. The MCs use the same camera simulation as the γ-ray MCs used to fill the lookups. Like for real muon images, the simulated light intensity from the Cherenkov cone is compared to the expected intensity. For a mirror reflectivity of 70 %, ε_{MC} has been evaluated to be 0.07249.

3.3.4 Event-Selection Cuts

The events seen by stereoscopic IACTs are dominated by showers generated by hadronic primaries. A separation of the desired γ-ray events from this background can be achieved

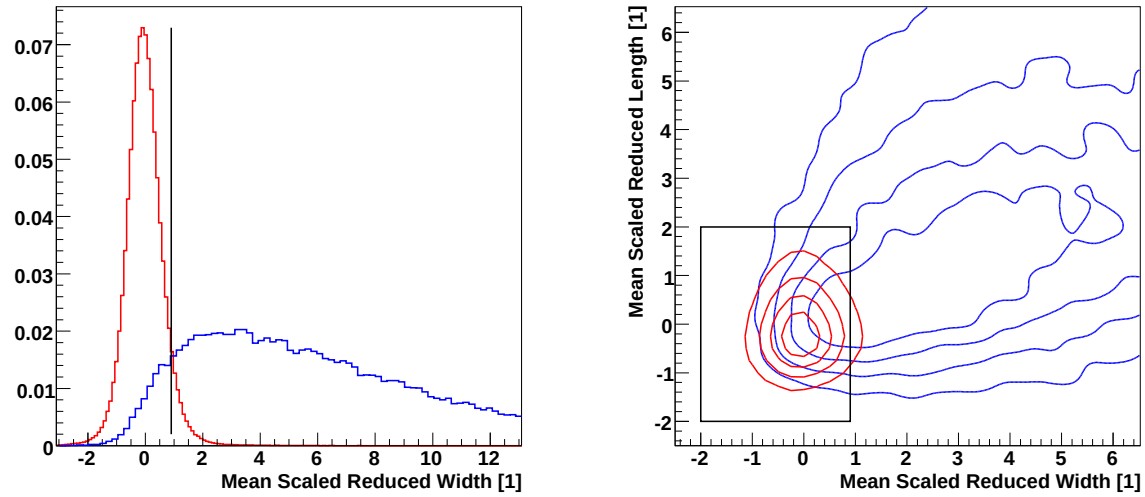

(a) MRSW distribution

(b) MRSW against MRSL distribution

Figure 3.8: a) The MRSW distribution of γ-ray MC events is drawn in red and for the background data events in blue from observations at a zenith angle at 30° and for offsets to the observation direction of 0.5°. b) The two-dimensional distribution in MRSW and MRSL is given in the right panel. The contour levels of the γ-ray events (red) and data events composed of background cosmic-ray events (blue) are 20 %, 40 %, 60 % and 80 %. The black line (box) in the plots give the standard set of event selection cuts.

by exploiting the differences in shower development between these two types of showers. A qualitative list of the difference between both shower types is discussed in Section 2.3.

The γ / hadron separation requires shower parameters on which intervals can be found that features a higher rate fraction of γ-ray events than for hadronic events. The performance of a given set of selection parameters is characterized by the selection efficiency ϵ_γ for gamma particles, ϵ_{bg} for background particles (remaining after cuts) and by the quality factor q. The quality factor describes the improvement of the signal-to-noise ratio:

$$q = \frac{\epsilon_\gamma}{\sqrt{\epsilon_{bg}}} \tag{3.24}$$

A robust approach for the definition of cuts is to select those events for which the value of the parameter p is included in the interval $[p_\nearrow, p_\searrow]$. $p_\nearrow$ and $p_\searrow$ are set to maximize the quality factor. The selection intervals describe a box in the phase space of two parameters, so that the combination of two cuts defined as intervals is called a box cut. The Hillas-style H.E.S.S. analysis, as it was presented in [7], includes three types of cuts:

1. cuts applied to shower images
2. cuts imposed on event parameters (all telescopes)

3. geometrical cuts on the morphologic extension of γ-ray sources (point-like sources)

The image cuts reject individual images with a relatively low quality. An event is rejected by the image cuts, if less than two shower images remain. The image cuts are applied on the local distances *loc* and the image amplitude s (Eqn. 3.10). *loc* is the distance of the amplitude centroid (x, y) to the camera center. Images with $loc > 0.525$ m are rejected. The local distance cut avoids truncated showers at the edge of the camera. One of the classical H.E.S.S. suggestions for sets of cuts are "standard cuts" [7]. These cuts are defined by a required size cut at $s > 80$ pe. The set is typically applied for spectral and morphological analysis of already discovered sources and the discussion in this Section will be restricted to the $s > 80$ pe cut. The cuts on the shower images are defined a priori without any optimization process, as it will be discussed for the event cuts.

The second type of cuts is applied to the parameters of the whole event, where the information of all telescopes is already merged. It has been shown for a simulated IACT [12], for the stereoscopic phase of the HEGRA experiment with data and MCs [57] and in preparations for the VERITAS experiment based on MCs [74], that the essential separation potential resides in the shower width. Therefor the width wid_{tel} in each shower image is reduced by the expected width $wid_{ex,tel}$ considering the reconstructed energy (Eqn. 3.23) and the impact distance. The reduced width is scaled with the standard deviation of this expectation $\sigma_{wex,tel}$:

$$wid_{rs,tel} = \frac{wid_{tel} - wid_{ex,tel}}{\sigma_{wex,tel}} \tag{3.25}$$

The expected width $wid_{ex,tel}$ and its deviation $\sigma_{wex,tel}$ are read from lookup tables, which are arranged analogously to the lookups for the energy reconstruction (Fig. 3.7). The deviation from the lookups yield an estimate of the variation on reduced scaled width $wid_{rs,tel}$:

$$\sigma_{rsw,tel} = \frac{\sigma_{wex,tel}}{wid_{rs,tel}} \tag{3.26}$$

The actual separation parameter, the mean reduced scaled width (MRSW) w_{mrs} is defined as weighted mean over all selected shower images from the individual telescopes:

$$w_{mrs} = \frac{\sum_{tel} wid_{rs,tel} \cdot \frac{1}{\sigma^2_{rsw,tel}}}{\sum_{tel} \frac{1}{\sigma^2_{rsr,tel}}} \tag{3.27}$$

The shape parameters for the example events are given in Table 3.2. The width of the image from the 2^{nd} telescope (Fig. 3.5) is $wid_2 = 1.961$ cm. The expected width derived from the lookup tables is $wid_{ex,2} = 2.145$ cm with a standard deviation $wid_{rs,2} = 0.323$ cm. This yields a reduced scaled width of $wid_{rs,2} = -0.57$ for the 2^{nd} telescope. The MRSW width, the merged information of all four telescopes is $w_{mrs} \sim 0.0$. This result is dominated by the image from the 1^{st} telescope, where the measured width meets the expected value.

The Hillas-style H.E.S.S. cuts are designed for point source analysis. Therefor, the events are selected in dependence of the distance θ of the event to the source. The cut is typically given for θ^2, so that the background level is constant in first approximation in the θ^2 distribution. Finally, the optimization of a set of selection cuts is done for the upper limit on the MRSW $w_{mrs,\searrow}$ and on θ^2. For the standard cuts ($s_{tel} > 80$ pe), a Crab-like point source has been assumed with 10 % of the Crab's flux. The cuts suggested independently of the zenith angle and the offset ψ are:

$$w_{mrs} < 0.9 \quad \text{and} \quad \theta^2 < 0.0125 \text{ deg}^2 \tag{3.28}$$

Additional quality cuts are imposed on the MRSW and on and the mean reduced scaled length MRSL (defined analogously to the MRSW). These cuts are set a priori without optimization and they suppress a small fraction of showers with unusual images:

$$w_{mrs} > -2.0 \quad \text{and} \quad l_{mrs} \in [-2.0, 2.0] \tag{3.29}$$

The TeV emission from Vela X is largely extended, so that the selection cuts have to be modified by skipping the θ^2-cut. Technically the $\theta^2_{\searrow}$ is set to 0.36 deg^2, where almost all particles emitted by a point-like source and spread by the IACT technique and the reconstruction algorithm are accepted. This approach has also been applied for the H.E.S.S. observation of the SNR RX J1713.7-3946 [8].

In Figure 3.8(a) the distribution of the MRSW for γ-ray and background events at a zenith angle around 30° and for event offsets to the observation direction of 0.5° is shown. The shower images have already been selected with regard to image amplitude and local distance. The cut on the MRSW is indicated by the black line. Both distributions in MRSW and MRSL are shown in Figure 3.8(b). The box cut is drawn in black. A γ-ray efficiency of $\epsilon_\gamma = 0.60$ is reached, while the background events can be reduced to $\epsilon_{BG} = 0.03$. The reconstructed direction is required to determine the offset and the MRSW of an event, so that the selection efficiencies are calculated based on the events with a reconstructed direction. The quality factor is 3.5 for $\varphi_Z = 30°$ and $\psi = 0.5°$. A list of quality factors under different zenith and offset angles is presented in Table 3.3.

3.4 Characteristics of the "Hillas Analysis"

The "Hillas analysis", described above, generates a list of TeV γ-like events, wherein the incoming direction, the primary energy and the time of arrival are given. The candidate events have passed the event-selection, so that they either should be generated by TeV photons or else be of hadronic origin while showing the characteristics of a γ event. Here, the characteristics of γ-rays induced events, determined by the reconstruction algorithm and by the telescope's hardware, will be presented. A discussion of the γ-like reconstructed and selected background events can be found in Section 4.2.

Table 3.3: The quality factors q, the analysis threshold t_a (Sec. 3.4.1) and peak energy of the background rates (Sec. 4.2.1) are summarized for the standard cuts (see text). The cuts for extended TeV γ-ray sources are applied and the selection cuts do not include the θ^2 cut. The selection efficiencies ϵ_γ (MC) and ϵ_{BG} (data) are the ratios of selected events to the events with an available reconstructed direction N_γ and N_{BG}.

φ_Z [°]	ψ [°]	N_γ	N_{BG}	ϵ_γ	ϵ_{BG}	q	t_a [TeV]	t_b [TeV]
20	0.5	637675	429160	0.597	0.028	3.549	0.279	0.266
20	1.0	618492	906957	0.556	0.028	3.297	0.279	0.266
20	1.5	570542	842179	0.434	0.031	2.464	0.279	0.266
20	2.0	398519	551234	0.356	0.035	1.911	0.279	0.293
20	2.5	254990	277304	0.259	0.036	1.365	0.556	0.322
30	0.5	620114	130774	0.599	0.029	3.527	0.343	0.322
30	1.0	601399	338236	0.559	0.030	3.246	0.343	0.322
30	1.5	555215	472605	0.443	0.029	2.585	0.367	0.354
30	2.0	409864	602396	0.372	0.029	2.202	0.367	0.354
30	2.5	267871	583254	0.271	0.028	1.607	0.596	0.322
40	0.5	608735	701674	0.598	0.021	4.126	0.519	0.472
40	1.0	590316	1838003	0.560	0.023	3.657	0.519	0.519
40	1.5	546357	2530191	0.451	0.027	2.755	0.519	0.519
40	2.0	413071	3183487	0.380	0.032	2.126	0.519	0.519
40	2.5	278685	3444454	0.282	0.036	1.418	0.966	0.429
50	0.5	857038	435409	0.598	0.029	3.520	0.902	0.761
50	1.0	833241	1088964	0.560	0.030	3.238	0.902	0.838
50	1.5	774152	1365611	0.456	0.031	2.592	0.902	0.838
50	2.0	613091	1568288	0.376	0.032	2.095	0.966	0.838
50	2.5	405933	1368246	0.276	0.033	1.518	1.274	0.692

3.4.1 Performance of the Energy Reconstruction

The quality of the energy reconstruction is studied by comparing the simulation energy and the reconstructed energy of MC events. The energy response matrix stores the distribution of events in the reconstructed energy in dependence of the simulated energy. The response matrix for observations of γ-rays at the zenith angle of 30° and with an offset of 0.5° is presented in Figure 3.9(a). A typical application of the response matrix is to fold a model for the spectral distribution of the γ-ray flux of a source with the expected smoothing by the energy reconstruction algorithm. The implementation of the forward folding method is discussed in [65]. The later discussion in this work makes use of a different approach. The reconstructed energy E_R will be assumed as a correct estimate for the primary energy of the high-energy photons. The assumption of good reconstructed energy corresponds to a near-diagonal response matrix, with few (and small) off-diagonal entries.

At low simulated energies ($<$ 400 GeV in Fig. 3.9(a)), the reconstructed energy is

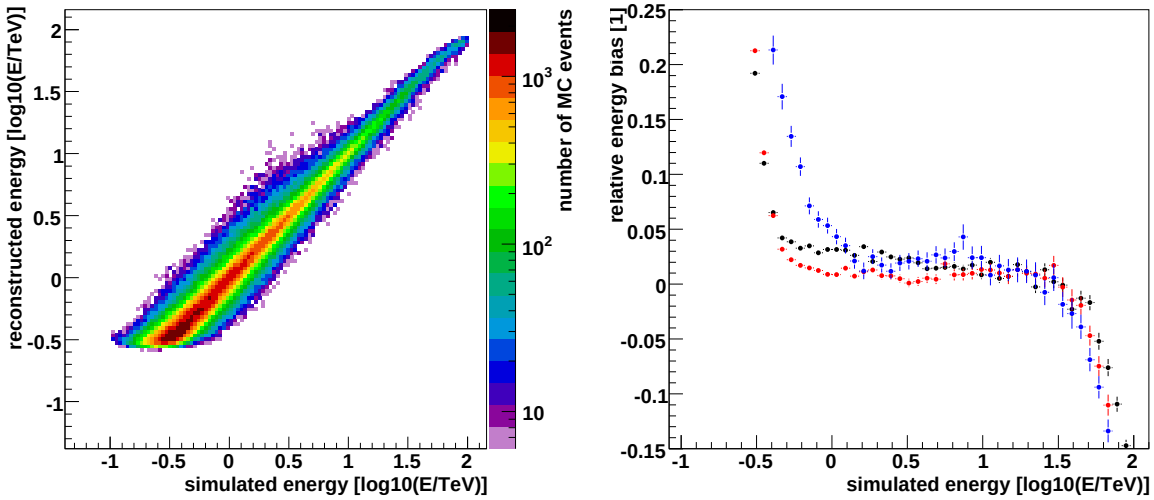

(a) response matrix (b) energy bias

Figure 3.9: The response matrix and the energy bias are derived from γ-ray MC simulations at a zenith angle of 30° and an source offset to the observation direction of 0.5°.

overestimated and the response matrix bent away from the diagonal. The reason for the overestimate is, that the low energies near the trigger condition (camera, CTS and *loc* cut) are statistically suppressed in the lookups for the energy reconstruction (Fig. 3.7). Influences on the flux determination of γ-ray sources are avoided by an analysis threshold t_a. All events below t_a will be rejected from the analysis. The analysis threshold is defined as the simulated energy E_S, where the energy bias E_{bias} exceeds 10 %:

$$E_{bias} = \frac{E_R - E_S}{E_S} \tag{3.30}$$

The energy bias is plotted as a function of the simulated energy in Figure 3.9(b). The analysis threshold is $t_a = 340$ GeV for this example at $\varphi_Z = 30°$ and $\psi = 0.5°$. The zenith and offset angle dependent values of t_a are listed in Table 3.3. The analysis threshold strongly depends on the zenith angle. In particular, the threshold rises with a zenith angle above 30°. The threshold is constant in the offset up to 2.0°. For the test samples at $\psi = 2.5°$ the energy resolution is much worse. This is one of the arguments for restricting the analysis to $\psi \leq 2.0°$.

A similar underestimate of the true energy by the reconstructed value appears for energies above 50 GeV. The definition of an upper analysis threshold is typically not necessary, as there is no flux from most of the γ-ray sources observable.

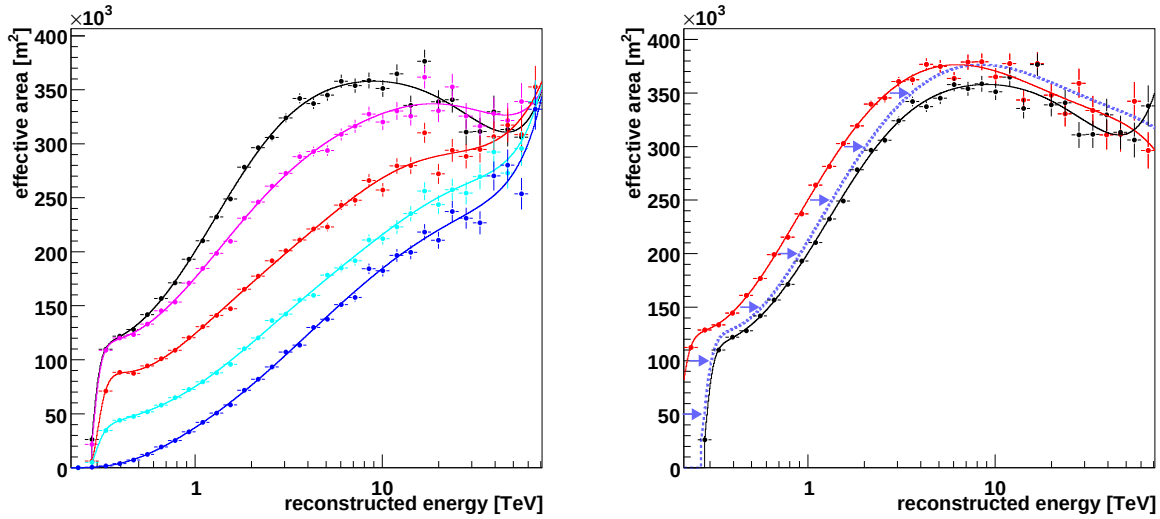

(a) effective area for different offsets

(b) effective area for different optical efficiency

Figure 3.10: a) The effective area is shown for a zenith angle of 30° in dependence of the reconstructed energy. Different direction of γ-rays emitters to the line of sight are drawn in different colors: 0.5° (black), 1.0° (magenta), 1.5° (red), 2.0° (cyan) and 2.5° (blue). b) The effective area for $\varphi_Z = 30°$ and $\psi = 0.5°$ is shown for two optical efficiencies $\epsilon_{MC} = 0.07249$ (black) and $\epsilon_{MCa} = 0.1$ (red). The blue, thick, broken line shows the effective area for ϵ_{MC}, determined from MC with an optical efficiency of ϵ_{MCa}. The arrows illustrate the shift from ϵ_{MCa} effective areas to ϵ_{MC}.

3.4.2 Trigger Efficiency

The detection area for primary particles and the detection efficiency for IACTs are combined in the effective area. The effective area is the size of the integrated area on the ground, where showers of γ-ray particles will be detected, which elongated path of the primary particle passes the area. The determination of the effective area, its dependencies and its handling in the H.E.S.S. analysis will be presented in the following.

The effective area is determined using the MC introduced on page 50. In these MC, the impact point (crossing between elongated path and the ground plane) is set randomly with a homogeneous probability density within a radius of 1000 m around the telescopes. The reconstruction and selection algorithms discussed above are applied. The effective area A is derived from the number of events N_p which pass the selection cuts, the total number of events N_s introduced in the simulation and the size of the area including the impact positions:

$$A\left(E, \varphi_Z, \psi\right) = \frac{N_p\left(E, \varphi_Z, \psi\right)}{N_s\left(E, \varphi_Z, \psi\right)} \cdot \pi \cdot 10^6 \cdot \mathrm{m}^2 \tag{3.31}$$

The MC are simulated for a defined zenith angle φ_Z and for a given offset ψ of the source position to the observation direction, so that A also depends on these parameters. Effective

areas at zenith and offset angles between the MC steps ($\varphi_Z \in [\varphi_{Z,low}, \varphi_{Z,up}]$ and $\psi \in [\psi_{low}, \psi_{up}]$) are calculated using linear interpolation. In a first step, the effective area is interpolated in the cosine of the zenith angle at the lower bound of the offset angle:

$$A_{ll} := A(\varphi_{Z,low}, \psi_{low}) \tag{3.32}$$

$$A_{ul} := A(\varphi_{Z,up}, \psi_{low}) \tag{3.33}$$

$$A_{\psi,low}(\varphi_Z) = (A_{ul} - A_{ll}) \cdot \frac{\cos(\varphi_Z) - \cos(\varphi_{Z,low})}{\cos(\varphi_{Z,high}) - \cos(\varphi_{Z,low})} + A_{ll} \tag{3.34}$$

and at the upper bound of the offset angle:

$$A_{lu} := A(\varphi_{Z,low}, \psi_{up}) \tag{3.35}$$

$$A_{uu} := A(\varphi_{Z,up}, \psi_{up}) \tag{3.36}$$

$$A_{\psi,up}(\varphi_Z) = (A_{uu} - A_{lu}) \cdot \frac{\cos(\varphi_Z) - \cos(\varphi_{Z,low})}{\cos(\varphi_{Z,high}) - \cos(\varphi_{Z,low})} + A_{lu} \tag{3.37}$$

$$\tag{3.38}$$

The second step interpolates A in the offset angle:

$$A_{\psi,up}(\varphi_Z, \psi) = (A_{\psi,up}(\varphi_Z) - A_{\psi,low}(\varphi_Z)) \cdot \frac{\psi - \psi_{low}}{\psi_{high} - \psi_{low}} + A_{\psi,low}(\varphi_Z) \tag{3.39}$$

The effective area is shown in Figure 3.10(a) for $\varphi_Z = 30°$ for different offset angles. The values $A(E)$ are given as points for the energy bins, in which the effective area has been processed. The error bars along the energy axis indicate the bin size, the error bars on the effective area are derived from Poisson statistics on N_p. The determination of the flux spectrum will use a smoothed version of the effective area. The smoothed area is the result of a fit with a polynom of seventh order on a logarithmic energy scale combined with a linear term in energy:

$$f(E) = p_0 \cdot \exp(p_1 \cdot \log_{10}(E)) + \sum_{i=0}^{7} p_{i+2} \cdot \log_{10}(E)^i \tag{3.40}$$

The smoothing function describes the effective area reasonably well starting at the analysis threshold up to an energy of about 10 TeV. For higher energies, the determination of the effective areas from MC simulations is problematic, due to a lack in MC event statistics.

The effective area in the energy bins depend on the spectral photon flux distribution, which has been chosen as a power law (pl, see Eqn. 5.16) with an index of 2.0 in the MC simulation. The spectral distribution can be corrected to any other assumed shape of the differential photon spectrum $\frac{dN}{dE}$ of a γ-ray source by weighting the events when adding up N_p and correcting N_s to N'_s:

$$N_p(E) = \sum_{events} \frac{\mathrm{d}N}{\mathrm{dE}}(E) \cdot \frac{1}{pl(E, 2.0)} \tag{3.41}$$

$$N'_s(E) = \frac{\mathrm{d}N}{\mathrm{dE}}(E) \cdot \frac{1}{pl(E, 2.0)} \cdot N_s(E) \tag{3.42}$$

The effective areas (as shown in Fig. 3.10(a)) are available for H.E.S.S. data preprocessed as lookup tables. They are corrected in these tables to a source spectrum following a power law with an index of 2.6.

The effective areas are defined in dependence of an energy E (Eqn. 3.31). They have to reflect trigger and selection efficiency for the energy scale, which is implemented in the method to reconstruct the flux of a γ-ray source. When the spectral shape of a source's γ-ray flux is determined by fitting the differential photon spectrum in the reconstructed energy (see Sec. 5.2), the energy scale of the effective areas has to be the reconstructed energy. This approach solves also a further problem. Like all other MC based lookups, the effective area depends on the fixed optical efficiency in the MC simulations. The correct effective area A_r for an observation run is extracted from the A-lookup produced for an optical efficiency ϵ_{MC} by reverse the run's optical efficiency $\epsilon_{\mu,r}$ from the reconstructed energy E_R (Eqn. 3.23). ϵ_R is the mean value over the optical efficiency for the single telescopes. The reconstructed energy is multiplied with the ratio of $\epsilon_{\mu,r}$ and ϵ_{MC}, when including it in Eqn. 3.31:

$$A_r\left(E_R, \epsilon_{\mu,r}, \ldots\right) \;=\; A\left(E_R \cdot \frac{\epsilon_{MC}}{\epsilon_{\mu,r}}, \ldots\right) \tag{3.43}$$

It can be show with two independent sets of MC produced for the optical efficiencies $\epsilon_{MCa} = 0.1$ and $\epsilon_{MC} = 0.07249$, that the MC at the fixed efficiency also describes the effective areas for runs in the interval $\epsilon_{\mu,r} \in [\epsilon_{MC}, \epsilon_{MCa}]$. An example for $\varphi_Z = 30°$ and an offset $\psi = 0.5°$ is given in Figure 3.10(b). The effective area for $\epsilon_{MC} = 0.07249$ is drawn in black and the effective area $\epsilon_{MCa} = 0.1$ in red. On a logarithmic energy scale, the effective area curve will be shifted by the ratio of ϵ_{MCa} and ϵ_{MC}. The blue, thick broken line shows the effective area for ϵ_{MC}, where the reconstructed energy has been transferred (shifted) from ϵ_{MCa} to ϵ_{MC}. The agreement between the shifted ϵ_{MCa} area and the area at ϵ_{MC} can be also found for all typical zenith angles and offsets up to 2.5°. Unfortunately, there is no further MC set available for lower optical efficiency, although observational data with efficiencies down to $\epsilon_\mu = 0.06$ exist. It will be assumed, that the effective area can be corrected for different optical efficiencies between 0.1 and 0.06. The upper range between 0.1 and 0.07249 has been proven by the existing MCs.

3.4.3 Point Spread Function

The point spread function (PSF) can be determined using the MC of primary γ-rays. The reconstructed direction (from the algorithm in Section 3.3.2) can be compared with the original position of the simulated point source. In Figure 3.11(a) the PSF of the four-telescope H.E.S.S. array, including events seen by only three or two telescopes, is shown in a radial projection around the source. The deviation of the reconstructed direction from the original can be described by a two-dimensional Gaussian function. For a small fraction of events, the direction reconstruction is worse. These events form a second component

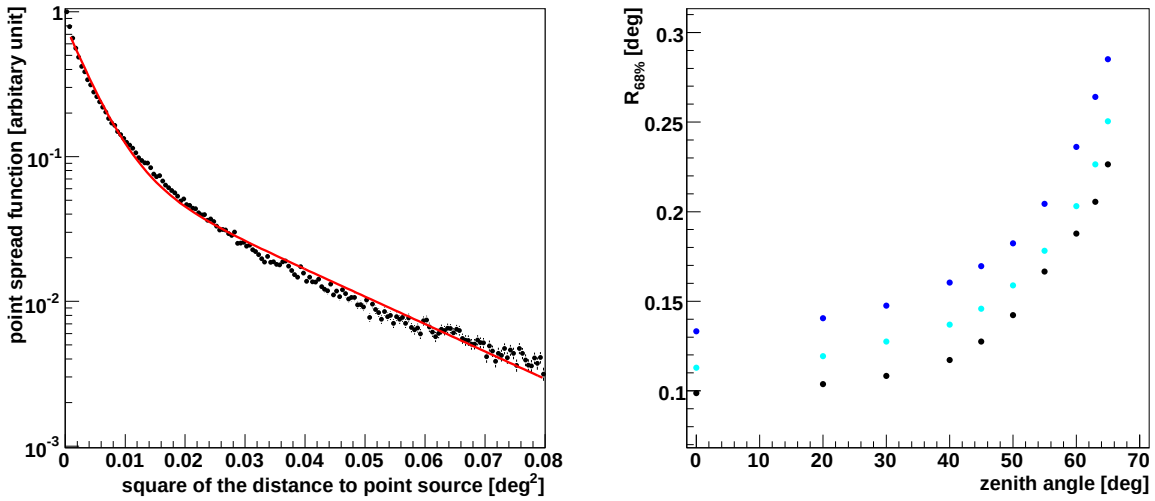

(a) point spread function (b) R_{68}

Figure 3.11: a) The point spread function at a zenith angle of 30° is shown for the full four-telescope array. The read line is a two-component fit. b) The radius containing 68 % of the events from a point source is plotted over the zenith angle. The radius is given for the source offset of 0.5° (black), 2.0° (cyan) and 2.5° (blue).

(p_1, p_3) in the PSF. The radial projection to the square of the distance between the reconstructed direction and the true position of the simulated source θ^2 of the sum of the two-dimensional Gaussian is:

$$psf\left(\theta^2\right) \quad = \quad p_0 \cdot \exp^{-\frac{\theta^2}{2 \cdot p_1^2}} + p_2 \cdot exp^{-\frac{\theta^2}{2 \cdot p_3^2}} \tag{3.44}$$

The radius R_{68} defines a circle around the point source position that contains 68 % of the selected events. In Figure 3.11(b) the radius R_{68} is plotted over the zenith angle. The black points are determined from the MC with a source offset of $\psi = 0.5°$. The point spread function radii up to an offset of 1.5° are comparable to the one at $\psi = 0.5°$. The point spread function becomes slightly broadened at 2.0°. For $\psi = 2.5°$ R_{68} almost doubles.

Chapter 4

Background from γ-like Events

In the previous Chapter, the analysis of observational data from the H.E.S.S. IACT array was discussed. The properties (energy resolution, effective area, point spread function) of the γ-rays air shower events are defined by the reconstruction algorithm and the hardware configure of the telescopes. The physics of electromagnetic air showers is relative simple and well understood, so that γ-ray events can be studied using MC simulations. In this Section, the background events will be characterized. These events are much harder to simulate as the air showers are more complex and only a small fraction of the events will pass the event-selection. The statistic of the background events simulated in MC is very low, a larger amount of computing power (depending on the simulated issues) is required to generate γ-like events. To avoid MCs for the characterization of the background events, the almost the complete data set of six years observations with the H.E.S.S. telescopes will be used in the following.

4.1 Background models

A large fraction of events originating from hadronic primary particles pass the event-selection and are indistinguishable from γ-ray events. A background model estimating the number of background events N_b is required. The number of excess counts N_{ex} which are generated by γ-ray photons can be derived:

$$N_{ex} = N_t - \alpha \cdot N_b \tag{4.1}$$

where N_t is the number of events contained in a test region for a γ-ray source. A test region is in general a well-defined region on the sky, in which the existence of a γ-ray flux is probed. α is the exposure ratio between the test region and the region used for background estimation. The exposure ratio is determined, for example, by the ratio of the geometrical size of the test and background regions and by the different observation durations between the extracted test data and the background data. The event counters

N_t and N_b, as well as the exposure ratio, in general depend on the energy and the position on the sky. Two methods for the estimation of the background are relevant for the analysis in Chapter 6. The focus is set here on the OnOff background model. But before it will be discussed here, the reflected background model will only be introduced briefly, whereas a full overview of the background models is given in [21].

4.1.1 Reflected Background Model

The reflected background model is a standard approach to estimate the energy-dependent background for a spectral analysis with observational data proposed for this type of analysis. Within this model, the background is extracted from the same observation run as the test region. This way, misestimation due to aging and partial failure of the hardware, the calibrations and different absorption of Cherenkov light in the atmosphere is avoided. The region from which the background is extracted is defined by a point reflection of the test region with respect to the observation direction. The requirement for the model to work is, that there is no contamination (e.g. by another source) in the background region. This implies that the test region should not enclose the observation direction. In variations of the reflected background method multiple background regions are searched in a ring around the observation position, which is given by rotation of the test region.

4.1.2 OnOff Background Model

In the OnOff model, observational data and background data are extracted from separate runs. Observation runs with no γ-ray source in the field of view are used as background data. Typical applications of the OnOff model are observations of extended sources. The observation strategy, when taking data on sources foreseen to be analyzed with the OnOff background model, is the classical OnOff mode, which was first proposed for the Whipple experiment [102]. Runs pointing to the source are interspersed by runs pointing to an empty field at the same zenith angle. The corresponding tracking points are located 5° in western and eastern direction on the sky for a source with a declination of $-45°$ (e.g. Vela X) and a run duration of $t_d = 28$ min. A background observation following these points with a time delay of t_d will track exactly the same zenith angles as the On target observation. Another advantage of the classical approach is, that the impact of variations of the observation condition is reduced. For example, conditions that related to hardware issues, are dust an the mirrors which will be cleaned by rain, broken and therefore missing pixels in the camera and the temperature of the pixels. But the most important impact is induced by the atmospheric conditions. The refraction index and the density in dependence of the height will influence the propagation of the Cherenkov light from the air showers to the telescopes, just as well the generation of the Cherenkov light and the shower development (Eqn. 2.3 and 2.6). In most cases, the atmospheric conditions may not change within in the hour observation for the On target and the background run. Although a monitoring

an the atmospheric conditions should be applied and observation pairs with an unstable atmosphere removed from the analysis (see e.g. [102]).

However, for H.E.S.S. almost no dedicated background runs have been taken. There are two reasons for the lack of such dedicated background runs. The first one is, that in the early years the extension of TeV γ-ray sources was not known and the accumulated data of the first years where required to recognize that our Galaxy is full of extended sources. The second reason is, that the observation strategy of the H.E.S.S. collaboration preferred a faster discovery of new sources instead of deep observations allowing a more accurate background estimation for already known sources. As an alternative for the dedicated background observations, other discretionary observation runs containing no γ-ray sources are used as background data. In order to arrange for a suitable pairing of On target and background runs, it is important to have a deep understanding of the background and its dependencies.

Background Data Selection for the OnOff Model

A critical step in the analysis with the OnOff background model is the selection of background runs. A heuristic algorithm is proposed to associate one background run with each On target run. To ensure that background and On target data were taken under comparable conditions the algorithm evaluates a set of i runwise parameters X_i. Here the algorithm will be given first, a discussion of the particular parameters can be found below:

1. A run list of On target pointings is generated. The runs have to fulfill the first three selection criteria (broken pixel, atmospheric fluctuations, clouds, Sec. 3.2).

2. The list of potential background runs contains all H.E.S.S. observations since December 2003, which pass the five run selection criteria. Runs are excluded from this list, if their observation position is located within $\pm 3^\circ$ in latitude along the galactic plane or if their field of view contains known, strong TeV sources.

3. For each On target run, the algorithm will loop over all available background runs and a weight W_r is calculated for each background run. The weight is the quadratic sum of the differences between the selection parameters of On target runs X_{On} and background runs X_{Off}:

$$W_r = \sum_i w_i^2 \cdot (X_{On,i} - X_{Off,i})^2 \tag{4.2}$$

   where the w_i are pre-defined weighting with coefficients which the individual parameters X_i enter the summation.

4. Pairs of On target and background runs are chosen, such as the total sum S of weight W_r over all selected run pairs is minimized:

$$S = \sum_{r \in On} W_r \tag{4.3}$$

In Section 4.2 the correlation between the selection parameters X_i is discussed. The investigated parameters are the zenith angle, the azimuth angle, the optical efficiency, number of broken pixels in the cameras, the temperature of the camera and the night sky background. The most important selection parameter is the zenith angle of the telescope pointing with the zenith angle being averaged here over the duration of the run and over the four telescopes. This example regarding the zenith angle also demonstrates one of the handicaps of the presented algorithm and the OnOff background model with non-dedicated background runs. Typically targets are observed near their maximum upper culmination. Therefor background targets which are in the same declination band as the On source target are preferred by the algorithm. It also implies that On data are taken during a different season of the year than the background data and that the background data will point on a small number of observation targets with a high exposure in the corresponding declination band.

4.2 Characterization of the Background

The main goal is to find parameters for the observation runs that characterize the background and to quantify the weighting factors for the background data selection algorithm discussed before. Furthermore, a general description of the background characteristics will be given. As before, all results are given for the standard cuts. However, most of the qualitative results should be applicable to other event reconstruction techniques and selection cuts. The discussion starts with the obvious dependency on the telescope's observation direction.

4.2.1 Zenith Dependency of the Background Event Rates

The zenith dependency of the system trigger (see e.g. Fig. 3.2) is carried over to the post-cut event rates. In Figure 4.1 the background rates for the different zenith angles φ_Z are given for standard cuts whereas in the left panel the background rates at $\varphi_Z = 30°$ are shown for events with an offset to the observation direction of $\psi \sim 0.5°$ ($0.25°$ to $0.66°$). The rates within energy bins are quoted in units of observation duration, solid angle and bin width in TeV. To obtain the background rates, events within a range of $\Delta\varphi_Z < \pm 1.5°$ around $30°$ have been selected from observation runs with an optical efficiency $\epsilon_\mu \sim 0.0725$ (Tab. 3.1). The curve contains about 30 h of observation time from which the known TeV γ-ray sources within the field of view were removed.

The background rate curve shown in Figure 4.1(a) is exemplary for other offsets and zenith angles. The background curves depending on the zenith angles and the offset are

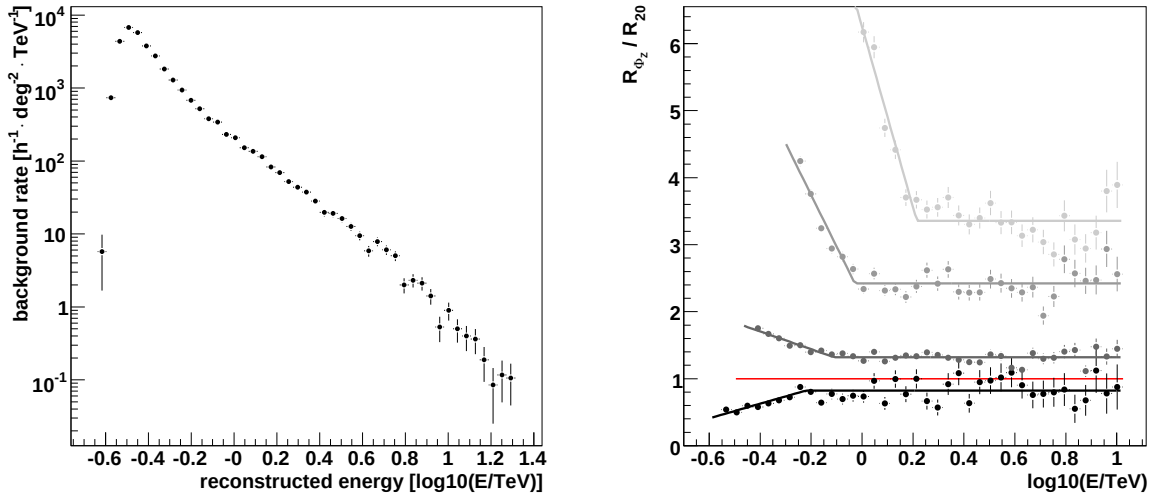

(a) absolute background rate

(b) normalized background rates

Figure 4.1: a) The post-cut background event rate (standard cuts) at an offset of $\psi = 0.5°$ and a zenith angle of 30°. b) The background rates averaged up to an offset of $\psi \leq 2.25°$ at $\varphi_Z = 0°$ (black), 30°, 40° and 50° (in decreasing shades of gray) are shown normalized to the background rates within the same energy bins at $\varphi_Z = 20°$ (indicated by the red line).

fitted with a sum of two power laws in the reconstructed γ-like energy E_r:

$$f(E_r) \quad = \quad n_1 \cdot \left(\frac{E_r}{\mathrm{TeV}}\right)^{-i_1} + n_2 \cdot \left(\frac{E_r}{\mathrm{TeV}}\right)^{-i_2} \tag{4.4}$$

The power-law sum is fitted between the energy where the background curve reaches their maximum rate and 10 TeV. In Table 3.3 the peak energy t_b is given and Table 4.1 states the parameters n and i. The background curves exhibit a soft component at low E_r with indices i_1 between ∼3.75 and ∼5 and a harder component with indices i_2 around 2.0. The maximal rate decreases from ∼15000 events per hour, TeV and deg^2 ($\varphi_Z = 0°$, $\psi = 0.5°$) to ∼1500 events per hour, TeV and deg^2 ($\varphi_Z = 50°$, $\psi = 0.5°$). Comparing the background rates for different offsets at a fixed zenith, the rates decrease with an increasing offset by an energy-independent factor over the whole energy range, up to offsets $\psi > 2.0°$(see also Fig. 4.2(b). This behavior allows to quantify the dependencies of the background rate on the zenith and the offset angle independently from each other.

The zenith dependence of the background rates is illustrated in Figure 4.1(b). As a reference curve the background rates at $\varphi_Z = 20°$ are chosen and the rates at other zenith angles are divided by the reference in each energy bin. The rate ratio is drawn in black for $\varphi_Z = 0°$. The ratios for $\varphi_Z = 30°$, $\varphi_Z = 40°$ and $\varphi_Z = 50°$ are drawn in decreasing levels of gray. All four ratio curves follow the same behavior. Their energy ranges are limited by the peak energy for low values of the reconstructed energy E_r. The ratios are restricted to 10 TeV, because it is hard to find a common description for all zenith angles

Table 4.1: The background curves depending on the zenith angle φ_Z and the offset ψ from the observation position were fitted with the sum of two power laws (Eqn. 4.4). The normalization parameters n_1 and n_2 are given in units of h^{-1} deg^{-2} TeV^{-1}.

φ_Z [°]	ψ [°]	n_1	i_1	n_2	i_2
0	0.5	failed		failed	
0	1.0	13.3	4.4	82.6	2.1
0	1.5	16.8	4.1	58.3	1.8
0	2.0	14.8	3.5	56.2	1.8
0	2.5	failed		failed	
20	0.5	8.1	5.1	151.0	2.4
20	1.0	29.9	4.3	91.5	2.0
20	1.5	37.0	3.9	61.3	1.6
20	2.0	15.5	4.0	64.0	1.7
20	2.5	55.7	1.7	-	-
30	0.5	30.8	4.5	175.1	2.2
30	1.0	65.3	4.0	102.5	1.9
30	1.5	36.4	4.5	97.8	1.8
30	2.0	26.1	4.1	76.9	1.6
30	2.5	66.0	1.6	-	-
40	0.5	114.0	4.3	290.6	2.0
40	1.0	107.6	4.9	253.2	2.0
40	1.5	162.0	4.3	157.1	1.6
40	2.0	74.5	4.3	146.8	1.6
40	2.5	failed		failed	
45	0.5	173.3	4.6	382.9	2.1
45	1.0	201.6	4.4	283.8	2.0
45	1.5	265.9	3.8	135.7	1.7
45	2.0	144.3	3.7	119.9	1.5
45	2.5	78.9	1.4	-	-
50	0.5	542.7	3.3	263.3	1.8
50	1.0	456.0	4.3	308.1	1.9
50	1.5	517.9	3.6	128.5	1.5
50	2.0	242.4	3.6	135.3	1.6
50	2.5	77.0	1.3	-	-

above 10 TeV. In the first third of the range, the background ratio can be described with a linear function in the logarithmic energy. In the remaining range up to 10 TeV the ratio is constant. Guiding lines following the linear respectively the constant behavior were included in the plot. The algorithm for the search of background data requires an estimate of the differential change in the background rate with the zenith angle. The estimate should aim for the analysis of the Vela X data described in Section 6, so that we are interested in the zenith angles between 20° and 50°. The analysis is most sensitive to systematic effects at low energies where the background rates are highest. An energy threshold for the Vela X data at 750 GeV will be discussed later, so that the differential change is read out between 750 GeV and 1 TeV, where the background rate rises with a relative factor in the order of 2.5 for 10° in the zenith angle. This corresponds to 15 % more background events per degree.

In Figure 4.2 the post-cuts background rates are plotted in dependence of the square of the offset ψ^2. The rates are normalized to the solid angle defined by the binning of ψ. A polynomial of 4^{th} order in ψ^2 has been used to model the background rates. As an example, the underlying data points for the rates at $\varphi_Z = 20°$ are given as dark red stars. The offset-dependent background rates are often called acceptance curves[1]. An implicit aspect of this

[1]The term "acceptance curves" stems from the idea that the offset-dependence of the trigger efficiencies for γ-rays and γ-like is similar. So that the positive term "acceptance" for the background efficiency is used, although efficiencies as low as possible are desirable

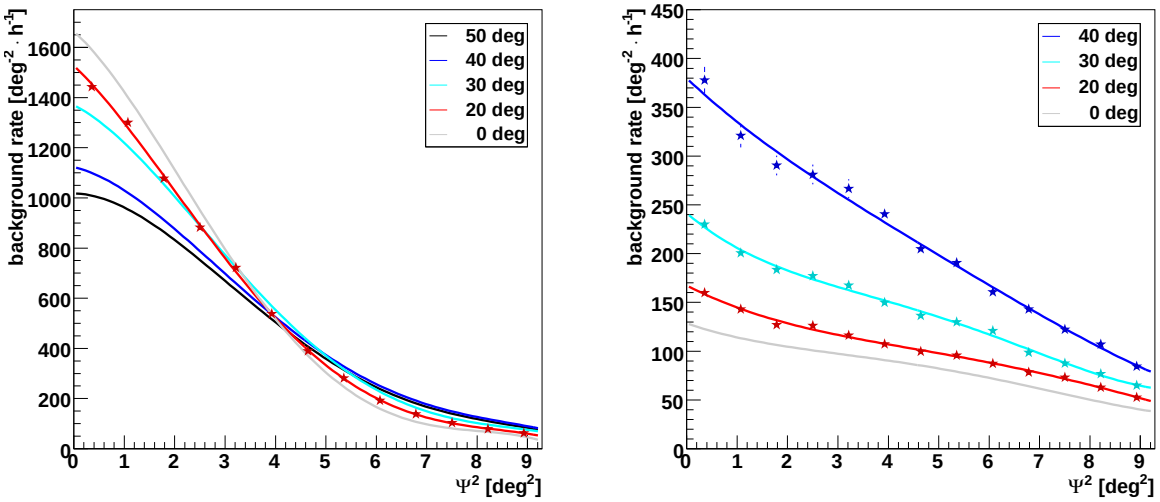

(a) acceptance curves

(b) acceptance curves, > 750 GeV

Figure 4.2: a) The background rates are shown at an offset ψ from the observation direction per deadtime-corrected observation time and solid angle. The background rates are integrated over the energy. The rates are drawn as modeled line for different zenith angles. The underlying data points are given as red stars for $\varphi_Z = 20°$. The statistical error is in the order of the size of the star symbol. b) The background rates are given with a lower cut on the reconstructed energy at 750 GeV.

term is that γ-ray and background acceptances can be mixed for simplification. The energy-integrated background curves are comparable to the acceptance curves presented by Berge et al. as normalized relative rates [21]. In Figure 4.2(b), the post-cut background rates are shown with an additional lower event cut on the reconstructed energy at ≥ 750 GeV. These curves are more suitable to derive the background rates for an analysis that applies a lower energy threshold as event-selection cut on the reconstructed energy. Such an energy cut should guarantee that all analyzed data fulfills the appropriate energy threshold. The background rates at 50° are skipped in the plot, as their energy threshold is higher than the 750 GeV. Later in Section 5.3, the exchangeability γ-rays and background acceptance will be rejected, at which γ-rays acceptance curves are derived using MC simulations.

4.2.2 Testing Scheme for Influences on the Background Rates

Apart from the zenith angle dependence, there are several other parameters which influence the background rates. However, these effects are typically more than a factor of 10 smaller than that of the zenith angle. Unfortunately, there is not enough observational data available to split it up first according to the zenith angle and second with respect to a further parameter. Hence, the influence of this second parameter cannot be derived in an absolute rate. Instead, the complete data set which passes the run selection (about 7000

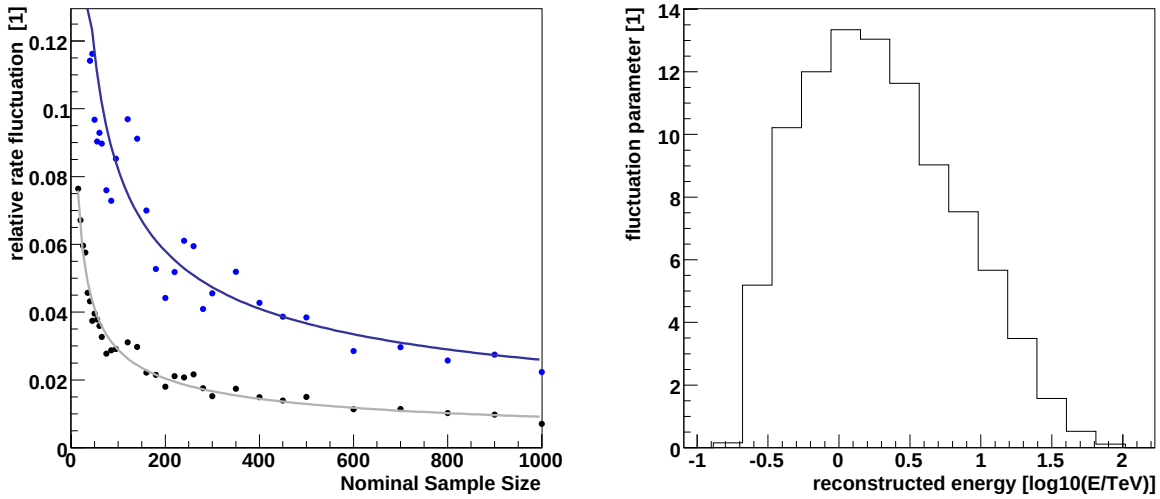

(a) fluctuation of the background rates

(b) fluctuation parameter

Figure 4.3: a) The plots show the relative fluctuation of the background rates at 550 – 900 GeV (black) and 25 – 40 TeV (blue) plotted against the nominal number of observation runs each with a duration of 28 min. A square-root function including a fluctuation parameter is fitted to the data points. b) The fluctuation parameter is derived for different γ-like energies.

runs) is split up into intervals in the parameter of interest. In particular an interval is chosen as reference. It should contain at least twice the number of runs (1000 to 2500 runs) compared to the other intervals. The algorithm for the search of background runs is used to associate a run from the reference interval to each run in a test interval. Within the algorithm the gradient of 15 % additional background events per degree in zenith angle is applied to compensate the influence of the zenith angle to the background rates. Runs will be skipped, if no unique partner run can be found within the reference with a maximal deviation in the zenith angle of 3°. This cut reduces the nominal number N_n of runs in each interval by a factor $f \sim 0.85$ to an effective number of run pairs N_e:

$$N_e := f \cdot N_n \tag{4.5}$$

The analysis is restricted to runs with a mean zenith angle below 45°. The background rate is determined for each interval and divided by the rate from the reference list. To study the influence of the primary energy of the cosmic-ray background events, the reconstructed γ-like energy is split into coarse bins equispaced on a logarithmic scale. The background rates are integrated over the field of view up to an offset of 2.25°. It is assumed, that the parameters of interest do not change the shape of the offset-dependent acceptance of the background rate.

The uncertainty of the determination of the rate ratios includes the statistical fluctuations due to the Poisson statistics in the data interval and the reference interval. Both are

statistically independent measurements, so that these statistical variations can be propagated easily to an error estimate for the rate ratios. The pure Poisson statistic approach works well for rate ratios at high γ-like energies (> 10 TeV). However fluctuations between the observation runs dominate the errors on the background rates for lower energies. These runwise fluctuations can be estimated by applying the described procedure for a random parameter. The error on the background rate ratio is then established as the RMS around the expected ratio of 1 for 100 tries of random parameters. The results of this approach are shown in Figure 4.3. The determined data points will follow the function of the square root of the interval size:

$$\Lambda = \frac{1}{\sqrt{a \cdot N_n}} \tag{4.6}$$

The fluctuation parameter a is found to be 12.0 for 550 – 900 GeV and 1.56 for 25 – 40 TeV. In Figure 4.3(b) the fluctuation parameter is given for the complete range in the γ-like energy. The relation can also be expressed through the effective number of run pairs (Eqn. 4.5), which is appropriate, if an entire OnOff list is to be rated:

$$\Lambda = \sqrt{\frac{f}{a} \cdot \frac{1}{N_e}} \tag{4.7}$$

4.2.3 Dependence on the Azimuth Angle

An azimuth angle dependency of the background rate can be expected for several reasons. The idea related most strongly to a physical motivation is that the shower development changes with the relative orientation of the shower to the magnetic field of the Earth. Monte Carlo simulations for protons [24] have shown that the pre-cuts trigger rate rises with a decreasing angle between the shower direction and the magnetic field. If the zenith angle is kept constant while the azimuth angle varies, one expects from the projection of the magnetic field direction on the horizon a maximal background rate at 14° from the northern direction. A minimum background rate should be seen near the south.

A second cause of a background dependency on the azimuth angle is the target tracking. During the typical duration of an observation run of 28 min zenith and azimuth angle change by several degrees, while the telescopes track a fixed target in the sky. For target positions in the northern ($\phi_A = 0°$) or in the southern ($\phi_A = 180°$) direction most of the tracking movement is seen in a change of the azimuth angle while the zenith angle remains at a constant level. On the other hand, for targets in the east ($\phi_A = 90°$) or in the west ($\phi_A = 270°$) the zenith angle changes by almost 10° and the azimuth angle is conserved. The parameter that is tested in the plots of Figure 4.4 is the mean azimuth angle over the observation time of the individual runs. A gradient from an asymmetric dependency of the background rate in the zenith angle (between lowest and highest angle) might be transfered it into an apparent dependency on this mean azimuth angle.

The relative changes in the background rate with the azimuth angle are shown in Figure 4.4. These plots bare a distinct minimum in the south and a maximum in the north. It is an

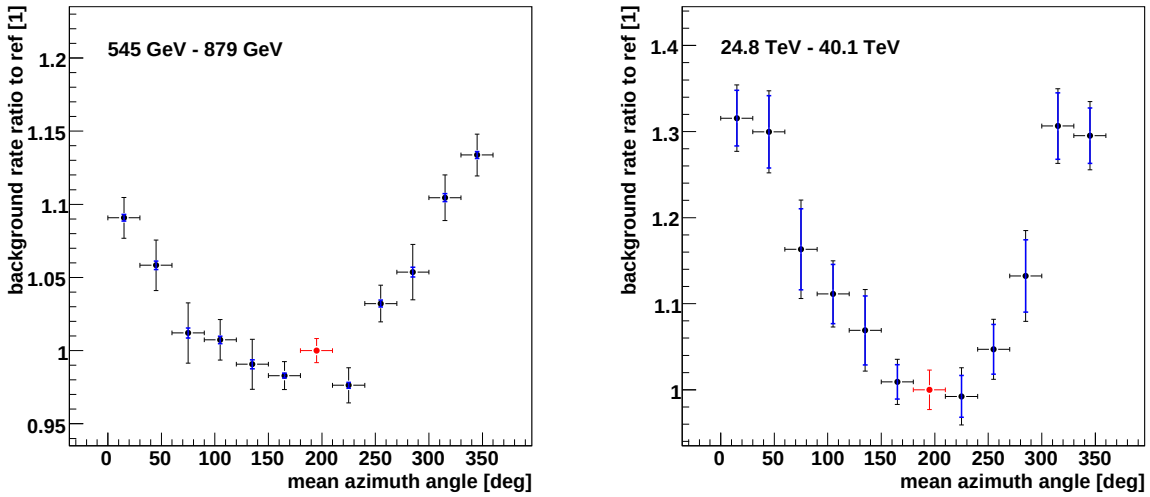

(a) 550 – 900 GeV (b) 25 – 40 TeV

Figure 4.4: The plots show the relative change of the background rate for reconstructed energies at 550 – 900 GeV and 25 – 40 TeV observed at different mean azimuth angles in comparison to runs observed at a reference azimuth angle of 195°. The horizontal errorbars indicate the applied binning for the azimuth angle. The blue error bars show the expected statistical error due to Poisson statistics and the black error bars include runwise fluctuations (see Eqn. 4.7). The red point indicates the reference data set.

evidence of a geomagnetic effect in the post-selected background rate. However, a detection claim for such an effect will require further investigations using dedicated observations. Sky maps of TeV γ-ray flux in this work are produced with a lower energy threshold of 750 GeV. As the systematics of these maps are dominated by the events with a low reconstructed energies near the threshold, the plot shown in the left panel (550 GeV to 900 GeV) gives a relevant estimation of the influence of the azimuth angle. The relative change in the rate is 20 % between the minimum in the south and the maximum in the north. The gradient which will be used as weighting factor is 0.1 % per degree in the azimuth. For higher energies a change in the behavior of the azimuth angle dependency of background rates cannot be observed. In the energy range from 24.8 TeV to 40.1 TeV (Fig. 4.4(b)), the amplitude of the effect reaches 30 % and 50 % for background rates with energies above 50 TeV (not shown here).

4.2.4 Dependence on the Optical Efficiency

It has been shown in MC studies for γ-ray showers that the reconstructed energy can be corrected for optical efficiency ϵ_μ (Eqn. 3.23) without affecting trigger efficiency after event-selection cuts (see Fig. 3.10(b)). Two differences in the characteristics of background events in comparison to these MC studies have to be considered here. First, the cut on the

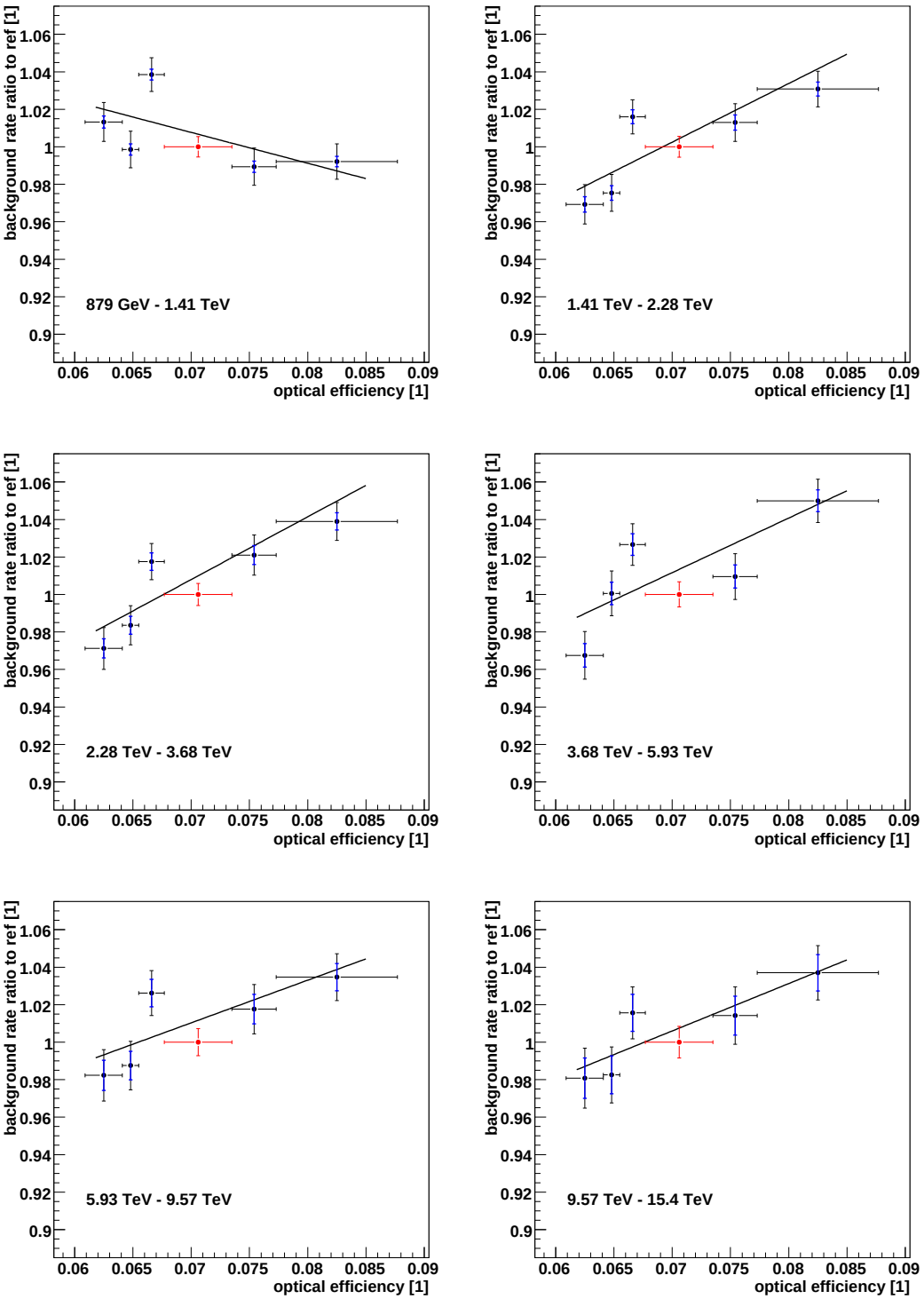

Figure 4.5: The plots show the relative change of the background rate with optical efficiency and include the rate ratios for different bins in reconstructed energy.

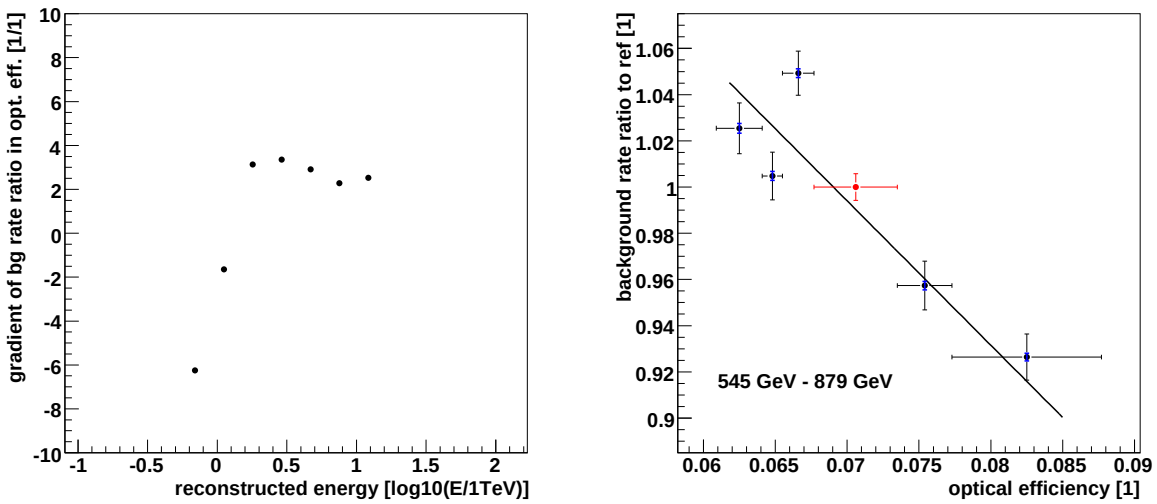

(a) rate gradients

(b) relative background rate

Figure 4.6: a) The relative change of the background rate for reconstructed energies at 550 – 900 GeV with the change in the optical efficiency is shown. For a detailed description see caption of Figure 4.4. b) The gradient in the background ratio is plotted over the reconstructed energy.

image size s (Eqn. 3.10) in the event-selection is applied without any correction on s for the optical efficiency. That is, the rate of background events at a given energy is reduced by a lower optical efficiency. During the determination of the γ-ray trigger efficiency from MCs, the event energy is reconstructed for the exact optical efficiency and correction for ϵ_{MC} does not affect anything. Second, the shower images of background events may still exhibit some differences compared to γ-ray images. In case of slight variations in the image size, the event-selection might lead to a different hadron or γ-like rating. The background rates of events corrected for optical efficiency indeed show a dependence on the optical efficiency, as can be seen in Figure 4.5. The background rate ratios are shown there for various γ-like energies between 900 GeV and 15.4 TeV. A linear function has been fitted to the data points and the gradient is $\frac{\mathrm{d}R}{\mathrm{d}\epsilon_\mu}$ ∼3. The gradient is constant for energies down to 2 TeV. For lower energies the gradient turns over to be negative. In Figure 4.6(a), the development of the gradients in the γ-like energy is presented. The gradient used as a weighting factor in the background association algorithm is again the one for the energy bin at 550 – 900 GeV (Fig. 4.6(b)). Its value is $\frac{\mathrm{dR}}{\mathrm{d}\epsilon_\mu} \sim -6$.

4.2.5 Dependence on the Number of Broken Pixels

Camera pixels in which no calibrated intensity data could be derived because of hardware failure are usually referred as “broken pixels”. They are removed from the analysis. The

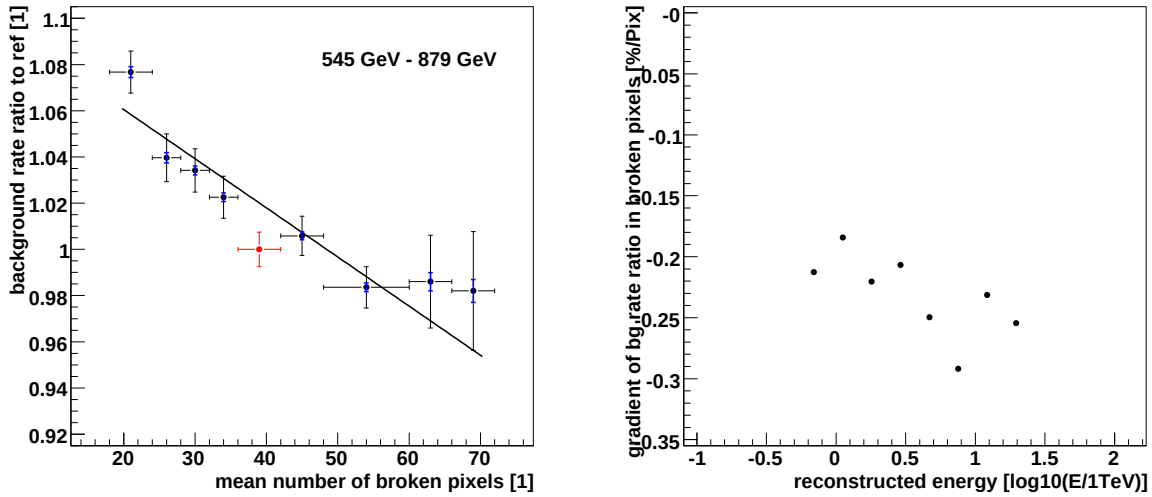

(a) relative background rate

(b) rate gradients

Figure 4.7: a) The plot shows the relative change of the background rate for reconstructed energies at 550 – 900 GeV depending on the mean number of broken pixels in the telescope camera within observation runs. For a detailed description see the caption of Figure 4.4. b) The gradient in the rate ratios of the dependency in the number of broken pixels is given for the different energy bins.

broken pixels affects the data analysis in two issues. The first one is the energy reconstruction where a missing pixels does not contribute to the image size, so that the reconstructed energy goes below the primary energy. This effect is the same for background events, although the reconstructed energy does not estimate the particles primary energy. The amplitude correction with the optical efficiency (Eqn. 3.23) does not correct for the broken pixel, as the muon coefficient is evaluated in a fit that ignores broken pixels. It has been shown that the broken pixels do not affect the muon coefficient as long as their number per telescope is smaller than ∼100 [30]. The second issue is the γ / hadron separation, where the event-selection parameters on the shapes of the shower images (Eqn. 3.13 and 3.14) can change for γ-ray events as well as for hadronic events.

The description of broken pixels has been simplified by counting them in a simple number. It is ignored that the pixels in the center of the camera are more important than at the edge and that broken pixel can group due to the hardware design of the camera. Anyway, the number of broken pixels influence the background rates as can be seen in Figure 4.7, at which in the left panel the background rate dependence on their number is shown for the energy interval between 550 GeV and 900 GeV. A linear fit results in the gradient $\frac{\mathrm{d}R}{\mathrm{dN_{BP}}} \sim -0.002$. In the right panel, the gradients are given up to a reconstructed energy of 40 TeV.

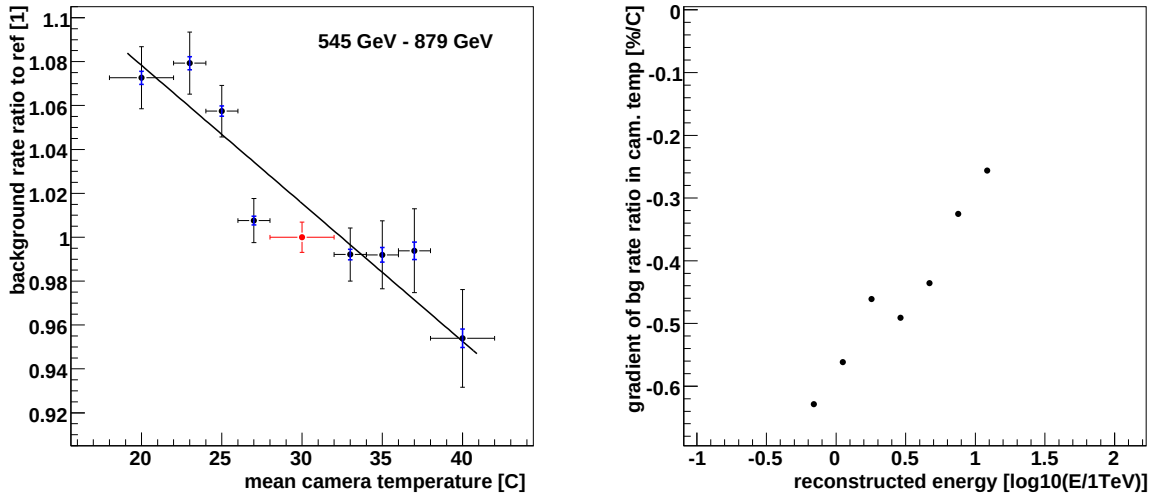

(a) relative background rate

(b) rate gradients

Figure 4.8: a) The plot shows the relative change of the background rate for reconstructed energies at 550 – 900 GeV depending on the mean temperature of the cameras during the observation runs. For a detailed description see the caption of Figure 4.4. b) The gradient in the rate ratios representing their dependency on the camera temperature is given for each energy bin.

4.2.6 Dependence on the Camera Temperature

A temperature per camera is measured with thermometers situated regularly in the electronic backend of the pixels. The mean temperature is derived by averaging the temperatures measured by these sensors over the duration of an observation run. Cooling is provided to the cameras by fans that exchange warm air inside the camera with ambient air. The cameras are operated in temperature equilibrium with the ambient air, which is reached typically within 1 h of operation. The mean temperature of the four cameras is used as the test parameter for the dependency test. Runs are rejected if the temperature of one camera deviates from the mean temperature by more than 2.5 ℃. In Figure 4.8(a) the dependency is shown for the energy bin at 550 – 900 GeV. As already seen for the other parameters, in each energy bin the rate ratio can be fitted with a linear function. The gradients evaluated in these fits are presented in Figure 4.7(b). At 550 – 900 GeV the gradient is $\frac{\mathrm{d}R}{\mathrm{dT_C}} \sim -0.006\ {}^{1}/_{\mathrm{°C}}$.

4.2.7 Dependence on the Night Sky Background

Another parameter which has often been claimed to show an effect on the background events is the noise in the PMTs generated by single photons distributed randomly over time (night sky background, NSB). It is assumed here that the NSB is distributed homogeneously over all camera pixels and over the duration of one observation run. That

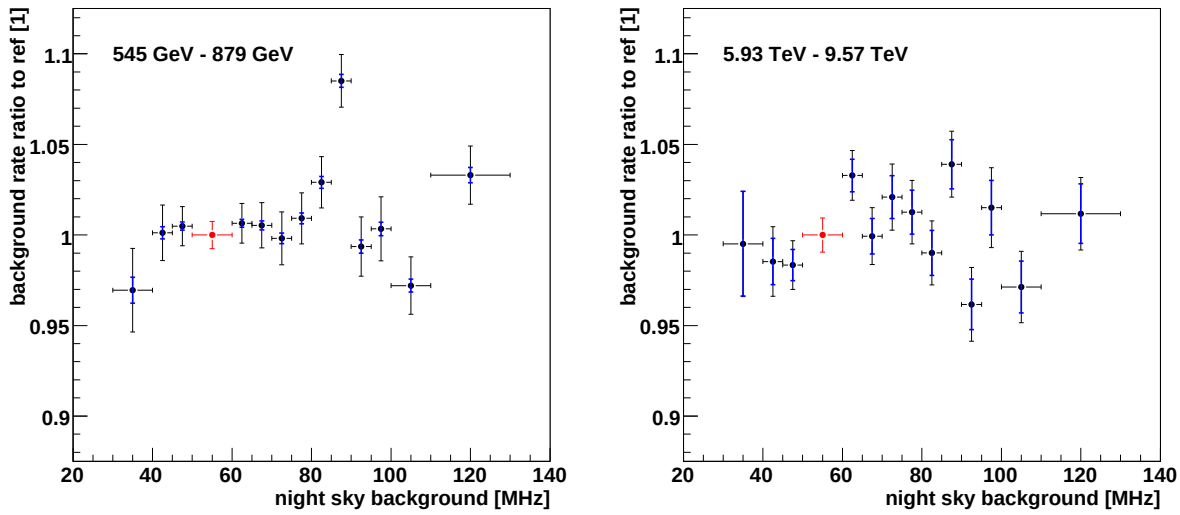

Figure 4.9: The plots show the relative background rate for reconstructed energies at 550 – 900 GeV and 6.0 – 9.6 TeV in dependence of the night sky background measured by the telescope cameras. For a detailed description see the caption of Figure 4.4.

is, NSB bright regions are not considered. The typical NSB rates seen by the pixels are between 50 MHz and 150 MHz.

Measurements of the NSB photoelectrons rate in a PMT are performed by the H.E.S.S. camera during standard observations with two different methods [5]. First, the current through the PMT's high voltage power supply is proportional to the NSB pe rate. The second method uses the width of the electronic pedestal, which is also proportional to the NSB rate. Both methods allow the determination of the NSB for each pixel in a time interval in the order of 1 s. The results of the NSB measurements are stored run-by-run for each telescope in a database. Unfortunately, in half of the runs one of the methods failed or both NSB measurement differ strongly from each other. These runs are excluded from the analysis presented here.

For the investigated NSB range, no effect can be found on the background rates within 1.5 % above 550 GeV in the reconstructed energies. As example, Figure 4.9 shows the corresponding plots for the energy ranges 550 – 900 GeV and 6.0 – 9.6 GeV. The limit of 1.5 % has been taken from the error estimator (Eqn. 4.7) at energies of 550 – 900 GeV tested in samples with a size of $N_e \sim 300$ runs. The statement that the background rate is independent from the NSB rate is validated here only for the whole field of view. That is, bright regions within the field of view ($< 1°$) and single bright stars are not considered.

A contribution to the ongoing discussion whether the background depends on the NSB rate for energies lower than 550 GeV can be made here, although it should be regarded with some caution. Regarding the energy interval between 340 – 550 GeV a gradient of $\frac{\mathrm{d}R}{\mathrm{dNSB}} \sim (-7.5 \pm 2.0) \cdot 10^{-4}$ $^1/_{\mathrm{MHz}}$ is found. As the background rate is dominated by the

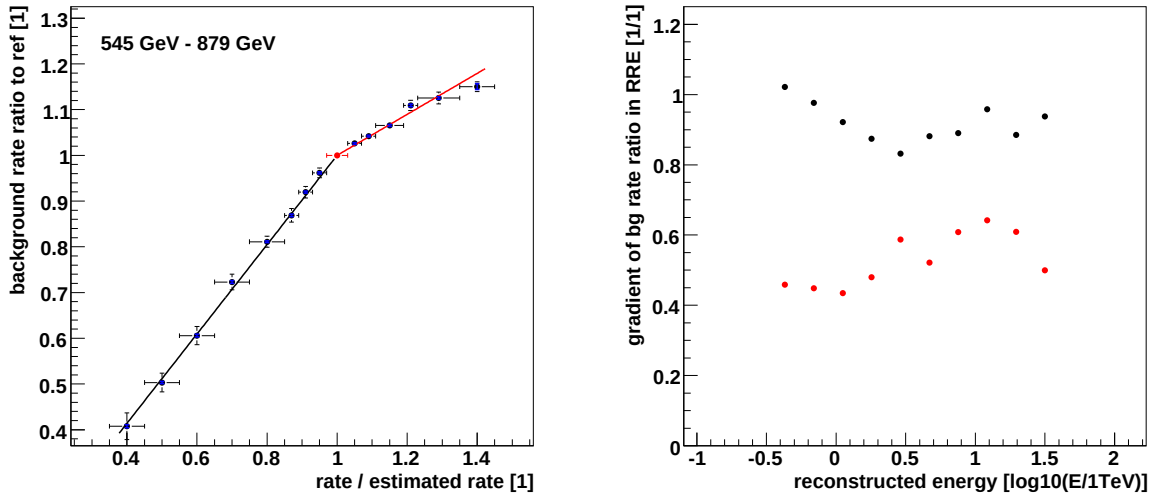

(a) relative background rate

(b) rate gradients

Figure 4.10: a) The plots show the relative change of the background rate as function of the ratio of the CTS rate to the estimated rate R/R_{est}. Two linear functions were fitted to the data points. b) The linear coefficients are drawn for different energy bins (in black for the lower linear component and red for the higher component).

events with low reconstructed energies, the dependence of the background on the NSB can also be detected, if no energy bound is defined. The results within the energy interval between 340 GeV and 550 GeV may be influenced by the disregarded systematics due to shifts of the peak of the background rate t_b (see Tab. 3.3) between different observation runs and systematics due to selection effects of the γ / hadron separation cuts, so that one should not trust the above-mentioned gradient and NSB dependence without further checks. For the analysis of the Vela X data, the background behavior for γ-like reconstructed energies lower than 550 GeV is irrelevant.

4.3 Rate Correction Methods for Atmospheric Fluctuations

It has been discussed that the status of the atmosphere can be generally understood by looking at the trigger rate of the CTS. Two approaches (background run selection, correction of the exposure ratio) to limit the effects of the appropriate atmosphere on the post-selected γ-like background rate for analysis with the OnOff background model will be presented. A tool for both approaches is the estimated trigger rate (Eqn. 3.8). The ratio of the actual CTS rate and the estimated rate can help to detect unacceptable hazy atmospheres, furthermore it is also an indicator for a continuous process of increasing cov-

erage of the sky with homogeneous layers of aerosols. The ratio of CTS rate and estimated trigger rate is a single parameter for each run, so that the testing procedure for background rates can be applied to R/R_{est}. The resulting plot for in the energy bin 550 – 900 GeV is given in Figure 4.10. The background rate ratios show the same shape for different energies, as can be seen in Figure 4.11. Two linear functions with a break B_{RR} are used to fit the ratios:

$$f\left(R/R_{est}\right) = \begin{cases} g_1 \cdot \left(R/R_{est} - B_{RR}\right) + 1 & \text{for} \quad R/R_{est} < B_{RR} \\ g_2 \cdot \left(R/R_{est} - B_{RR}\right) + 1 & \text{for} \quad R/R_{est} > B_{RR} \end{cases} \tag{4.8}$$

The fit results for the gradients g_1 and g_2 are plotted in Figure 4.10(b). The break has been set to the fixed value $B_{RR} = 1$. For the first parts of $f\left(R/R_{est}\right)$ below the break, the gradient g_1 is 1. This demonstrates a 1:1 relation between the pre-selected event trigger rates of CTS and the post-selected rate of γ-like background events.

4.3.1 Correction within the Association of Background Runs

An approach to correct for atmospheric fluctuations is to include the R/R_{est} ratio as associate parameter into the background run selection algorithm (Sec. 4.1.2). To be more specific, the gradient g_1 below the break (Eqn. 4.8) is used as weighting factor. The disadvantage of this correction method is that the selection on the trigger rates reduces the impact of the other weighting factors. In Section 4.4, the background rates are compared for an Off selections considering the R/R_{est} ratio with an Off selections ignoring any atmospheric monitoring parameters.

A short notice should be given here, on another quite simple approach that is similar to the above suggested background run selection. One can start with an background run selection that does not considers the atmosphere. The region of the analyzed source is excluded and the background rates for the On target runs and the background runs are compared, e.g. in dependence of the zenith angle φ_Z or the offset angle ψ. Background runs are replaced until the background rates match. Note that such an approach is not recommended here to produced unbiased results with the OnOff background model.

4.3.2 Modifying the Exposure Ratio

Another possibility to correct the influence of the atmosphere is to modify the exposure ratio (Eqn. 4.1). The fit function $f\left(R/R_{est}\right)$ (Eqn. 4.8) with the parameters $g_1 = 1$ and $g_2 = 0.4$ derived in the energy range 550 – 900 GeV will be applied. For each run pair, the original exposure ratio α_A is corrected to:

$$\alpha_{A,cor} = \frac{f\left(RR_t\right)}{f\left(RR_b\right)} \cdot \alpha_A \tag{4.9}$$

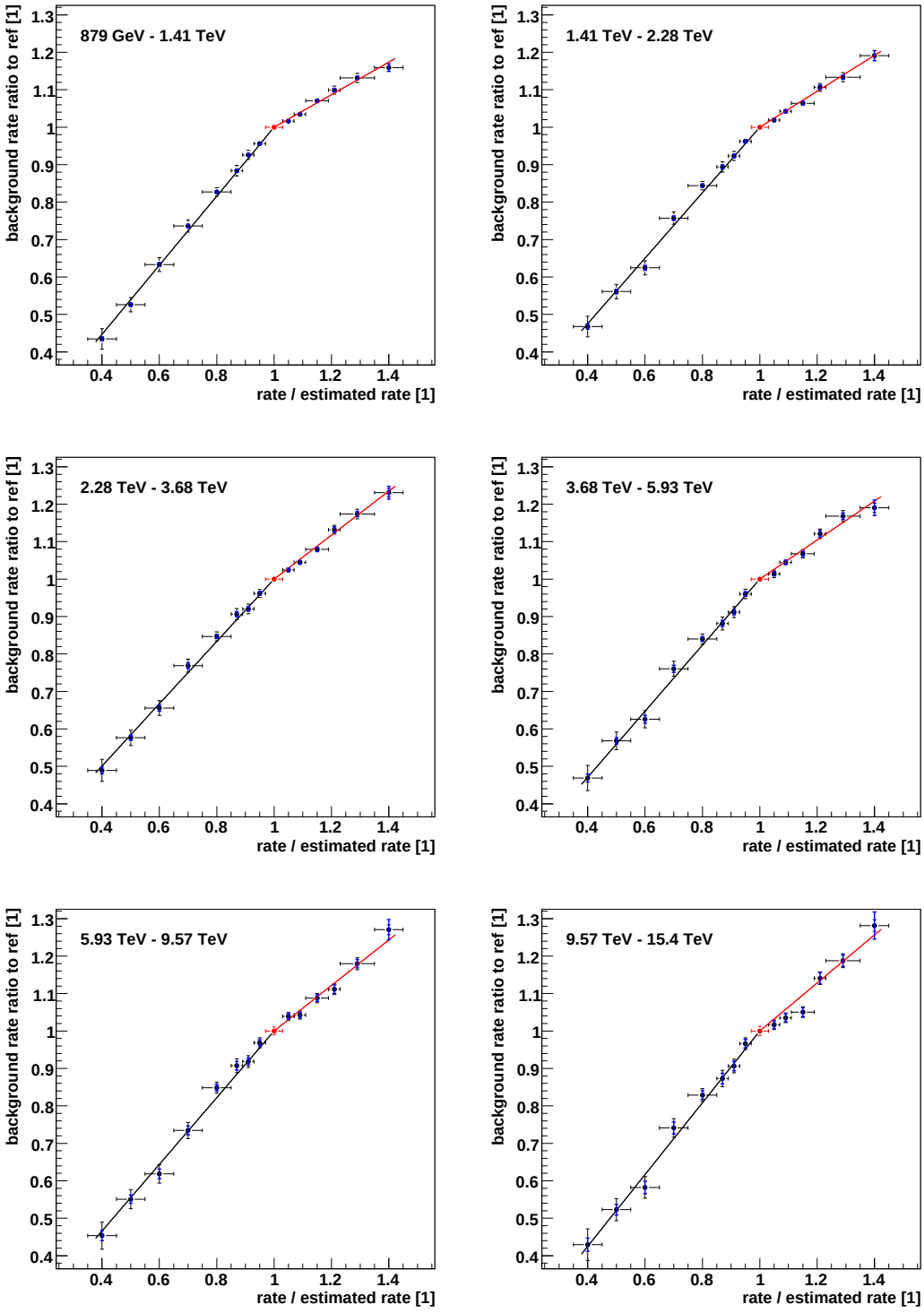

Figure 4.11: The plots show the relative change of the background rate depending on the ratio of the CTS rate to the estimated rate R/R_{est}. Two linear functions connected at a break point were fitted to the data points. A general description of the plots is given in the caption of Figure 4.4.

where RR_t is R/R_{est} for the On target run and RR_b for the background run. In the following this approach will be referred as R/R_{est} correction. For the OnOff model without any further background corrections, α_A is given by the ratio of deadtime-corrected observation times between the On target runs t_t and the background runs t_b:

$$\alpha_A = \frac{t_t}{t_b} \tag{4.10}$$

4.3.3 General Ideas of Correcting Atmospheric Fluctuations

A short summary of the existing ideas for the correction of the atmospheric fluctuations in the analysis of IACT data will be helpful in the following discussion. The suggested approaches aim for a determination of the influence on the detection of γ-ray events from point sources that are variable in their flux on time scales of hours to months. In the analysis of these sources the background is extracted from the same field of view (e.g. reflected background) and the atmospheric influence on the background events is not relevant, as both the background model and the test region are affected in the same way. However, the general ideas will also work for background events, which are of interest for the OnOff background model.

For H.E.S.S. data a method to correct for a hazy atmosphere has already been presented for the data analysis of the active galactic nucleus PKS 2155-304 [93]. Therein an estimated trigger rate depending on the zenith angle has been used to assign to each observation run one of three classifications regarding the atmospheric conditions. For each class a separate set of MC as basis for effective areas and background separation was produced, where the models for aerosol layers in the atmosphere were included in the simulations. Hereby, the authors were able to use data affected by hazy dust layers which would otherwise have been discarded. It was shown that the uncorrected flux spectrum is significantly softer in comparison to the corrected spectrum.

A very interesting suggestion for the correction of atmospheric fluctuations was made for the pioneer experiment Whipple [79]. The authors used a histogram over the Cherenkov light luminosity per event of an observation run. The definition of the luminosity parameter is comparable to that of the image size used in this work (Eqn. 3.10) and thus it is likewise proportional to the primary energy of cosmic rays. A throughput factor is defined that represents the relative fraction of detected pe in an observation in comparison to a reference observation. If the luminosity is plotted on a logarithmic scale, the throughput factor will shift the histogram in vertical direction. The procedure works similar to the evaluation of the optical efficiency via single muon events (see Eqn. 3.43) and it measures the optical efficiency of a telescope and of the atmosphere up to the height where the shower of secondary particles starts to develop. In Figure 4.12(a) the authors demonstrate the determination of the throughput factor for the example of light collecting cones in front of their telescope camera. An observation run has been taken with these cones and one without. The lower plot gives the resulting χ^2 for test values of the throughput factor

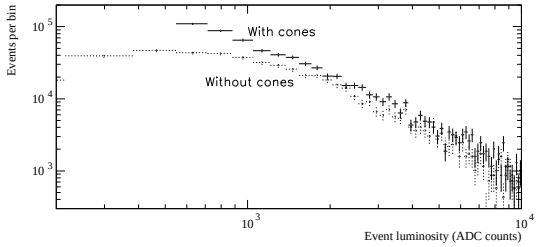

(a) throughput factor (Whipple)

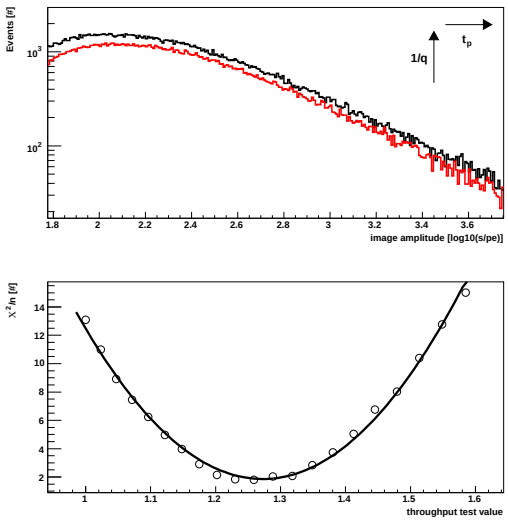

(b) throughput factor (H.E.S.S.)

Figure 4.12: a) The upper plot shows two luminosity curves (see text) taken with the Whipple telescope. A χ^2-minimization is used in the lower plot to evaluate a factor in the luminosity that shifts the With-cones-curve to the Without-cones-curve. The plots have been taken from [79]. b) In the upper panel, the image size distribution of a run observed with a clear atmosphere (black) and a hazy atmosphere (red) is shown. The lower plot shows the minimum in χ^2 for the throughput factor that shifts the hazy sky distribution to the clear sky distribution.

when the curve with cones is shifted (logarithmic scale) to the curve without the cones. A minimal χ^2 is found for a throughput of 0.73 which is consistent with an independent estimate for the effect of the cones given by the authors [79].

The drawback of the throughput factor in the analysis of γ-ray sources is that it requires a reference luminosity distribution. In general the luminosity distribution depends on the zenith angle of the observation, so that one observation run in a source's data set is not a sufficient reference by itself. Below, the application of the throughput concept to H.E.S.S. data will be discussed (Fig. 4.12(b)).

For the MAGIC telescope monitoring of the atmosphere is guaranteed by optical telescopes situated at the same site (Roque de los Muchachos Observatory on La Palma, Canary Islands). A correction based on the extinction coefficients in the red optical bands (r' and R band) was presented in [40]. The authors showed that by using their correction they can reduce the spread in the image size distribution curves for different observations.

4.3.4 Advanced Correction Method for Atmospheric Conditions in H.E.S.S. Observations

We have seen two ideas to measure the influence of the atmosphere on the cosmic-ray air showers (mostly generated by protons) in order to correct the flux estimate for TeV γ-ray sources. The first approach makes use of the trigger rate of the IACTs array which allows to classify the atmosphere. The second idea defines an optical efficiency for the Cherenkov light yield of cosmic-ray events that includes the transmissibility of the relevant parts of the atmosphere as well as the efficiency of the telescopes. This atmospheric throughput can be measured from the light (size) distribution of the invariant cosmic-ray flux and spectral shape. The connection between both approaches is the integration over the size distribution. In the simplest case for single-telescope operation the integral over the distribution is the trigger rate of the telescope. Although the logic of a stereo trigger (for H.E.S.S. the CTS rate) is more complex, a relation between the integral and the trigger is still traceable.

A throughput is determined for an example of two H.E.S.S. observation runs and it will be compared to estimate of the atmospheric conditions with the R/R_{est} ratio. Both runs (No. = 36652 and 33567) were observed with a mean zenith angle of $\varphi_Z = 64.4°$ and an optical efficiency of $\epsilon_\mu = 0.0725$, hence it is not necessary to consider any dependency of the size distribution on these two parameters. The $(R/R_{est})_{36652}$ ratio for the first run is 1.042 and for the second run $(R/R_{est})_{33567} = 0.748$. The latter run is thus clearly affected by a hazy atmosphere. Due to the influence of a denser atmosphere the size distribution will be shifted to lower values by the loss of photons within one image and the total amount of events will decrease because of events getting too weak for triggering the CTS – especially in the second telescope required for an array trigger. A size distribution of the shower images taken with one of the four telescopes are shown in the upper panel of Figure 4.12(b). Other than the selection introduced by the hardware trigger (CTS), no event selection has been applied. The two distributions s^{36652} and s^{33567} can be shifted (logarithmic scales) to match each other by minimizing the sum in the bin index p within the range between 320 pe ($10^{2.5}$) and 3200 pe ($10^{3.5}$):

$$\chi^2(p,q) \;=\; \sum_i s_i^{36652} - \frac{1}{q} \cdot s_{i+p}^{33567} \tag{4.11}$$

where the trigger loss factor q reduces the size distribution for the second run by the events that do not trigger because of the denser atmosphere. The throughput factor t_p is then the bin size ds times the number of shifted bins p were χ^2 reaches its minimum:

$$t_p \;=\; \mathrm{ds} \cdot \min_{\chi^2(p,q)} p \tag{4.12}$$

As the throughput factor and trigger loss factor both cannot be extracted from the size distributions, it will be assumed that q equals 1. It might be also possible to find a description for a relation between t_p and q, whereby in a general case, the relation can depend also

on the image size or further parameters like the zenith angles of the observations. Using the results of Section 4.2.4, a limit for the loss factor can be suggested. A decrease of the optical efficiency by 50 % can be estimated for a reduction of the post-selected background events by only 10 %. The effect might be a bit larger for the pre-selected events shown in the size distribution, however one can assume that the true value of q is not smaller than 0.8.

For the two example runs, the throughput factor is found to be $t_p = 1.276$ (lower panel of Fig. 4.12(b)). The parametrization of Eqn. 4.4 for the background rates can be modified according to the throughput factor:

$$I_r\left(t_p\right) = \int_{t_p \cdot 550\ \mathrm{GeV}}^{t_p \cdot 900\ \mathrm{GeV}} \left(n_1 \cdot \left(\frac{E}{\mathrm{TeV}}\right)^{-i_1} + n_2 \cdot \left(\frac{E}{\mathrm{TeV}}\right)^{-i_2} \right) \mathrm{dE} \tag{4.13}$$

As integration range again the same range from 550 GeV to 900 GeV will be used which was already considered for the determination of the relation between CTS rate and background rate (Fig. 4.10(a)). The parameters for $\varphi_Z = 30°$ and $\psi = 1.0°$ are taken from Table 4.1 to calculate the integrals for the example runs:

$$\begin{aligned} I_{36652}\left(1.0\right) &= 164.4 \\ I_{33567}\left(1.276\right) &= 104.4 \end{aligned} \tag{4.14}$$

The ratio of both integrals that estimates the ratio of the background rates is 1.57. On the other hand, the expected ratio from the R/R_{est} ratio (Eqn. 4.8 and 4.9) is 1.39. The discrepancy between both methods can be explained by the trigger loss factor. To bring both methods to an agreement $q = 0.930$ is required, which is consistent with the assumed limit of 0.8.

The example shows that there is a potential for the throughput factor to be integrated as an atmospheric correction method in the analysis of H.E.S.S. data. Starting-points for an implementation of the throughput may be:

a) as correction factor for the size of a shower image;

b) as factor in the energy reconstruction (analogously to the muon efficiency ϵ_μ in Eqn. 3.23);

c) as scaling factor for event rates (γ-rays and background).

However, there are a few questions that will be left open here and have to be clarified first:

- The trigger loss factor has to be determined either from a large amount of observational data or with MC. If required, q can be evaluated for different size values.

- The relation between throughput factor and optical efficiency from muon rings should be clarified. It would be interesting to investigate whether the trigger loss factor may even be used to correct for the number of broken pixels.

- The throughput factor is determined relative to a reference size distribution. The reference has to deal with systematic influences on the size distribution, e.g. by different zenith angles, without becoming inconsistent for different (On target) runs of an analysis data set. In the OnOff model the On target run is a suitable reference for the corresponding background run to correct for background rates. If a general, absolute reference can be found, a correction for the γ-ray flux between different observation runs will be possible for any background model.

- The dependencies of a background rate (discussed in Section 4.2) have to be reunderstood when a throughput correction is applied. Most interesting is the relation between the background ratio and the R/R_{est} ratio (Fig. 4.10 and 4.11), as this plot will give a feedback on the impact of the potential throughput correction.

- The influence on the reconstructed energy of γ-ray events can be tested with MCs. The control histograms are the response matrix and the energy bias (Fig. 3.9).

4.4 Darkfield tests for the OnOff Background Model

The OnOff background including the background run selection algorithm and the correction method for the hazy atmosphere can be tested on darkfields. Darkfields are test regions without any detected TeV γ-ray source. Observations of active galactic nuclei (AGN) contain appropriate darkfields. For the H.E.S.S. telescopes, these sources are point-like, they are extra galactic sources and no diffuse emission as from the galactic plane is expected in their surroundings. AGNs are variable sources, so that many of them are reobserved and a large exposure time is available for the field of view around them. As discussed before, the selection algorithm prefers background runs with observation targets at a similar declination as the On target runs. Here, the sky will be divided into 10°-wide declination bands. Only one source will be selected in each band, to guarantee that the different darkfields are tested with independent background data. A scan for TeV γ-ray sources or diffuse γ-ray emission in the test regions is beyond the scope of this thesis, so that the complete coordinates of the AGN will not be given here[2].

The first tested darkfield lies in the declination band between $-15°$ and $-25°$ and will be discussed as an example for the other bands. There are 68 observation runs with four telescopes passing the run selection, the first one dating from April 2004 and the last one from January 2008. The observations were performed in the so-called wobble mode (for details see [7]), where the observation positions are wobbled in small distances around the

[2]In each of the declination bands, there is at least a second AGN with a comparable amount of exposure available, so that an identification of the original target is not possible.

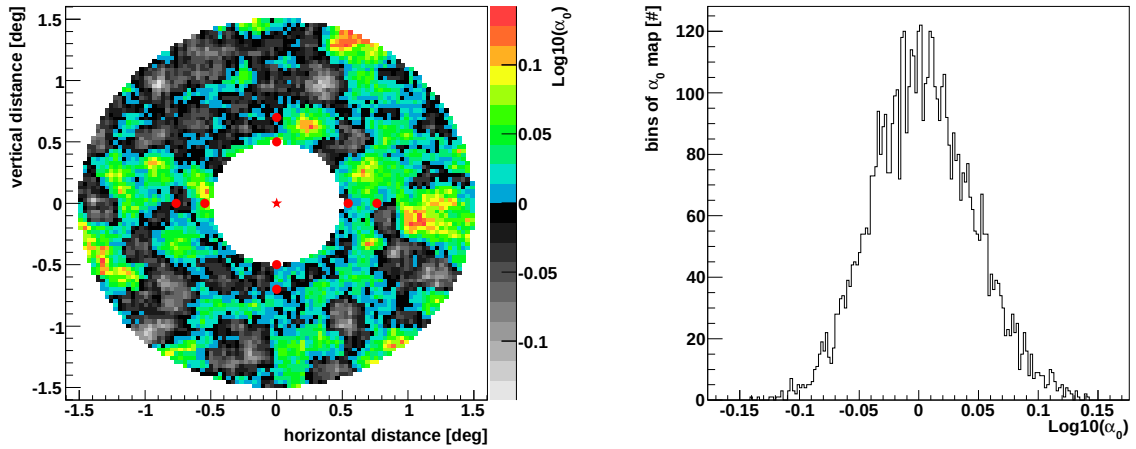

(a) α_0 sky map (b) α_0 distribution

Figure 4.13: a) The sky map shows a supposed darkfield around an AGN, whose position is indicated with a red star. The horizontal axis is parallel to the right ascension axis and the vertical axis is parallel to the declination axis. The red dots mark the pointing positions which the telescopes tracked in the corresponding observation runs. The sky map show the ratio between the sourceless foreground and the background events (α_0, Eqn. 4.15) on a logarithmic scale. b) The distribution of the values of α_0 has been extracted from the bins of the sky map.

source position. A sky map of the darkfield is shown in Figure 4.13, where the observation positions of the runs and the source position are marked. The darkfield is defined as a ring between the radii 0.5° and 1.5° around the AGN.

The darkfield test is based on the assumption, that the test region is free of TeV γ-ray sources, so that the number of excess counts N_{ex} should be zero on average. The exposure ratio α is split up into the ratio determined in the data analysis α_A (including the ratio of observation durations and R/R_{est} correction where applied) and an additional factor α_0, which is defined such as to fulfill the condition $N_{ex} = 0$:

$$\alpha \;:=\; \alpha_A \cdot \alpha_0 \tag{4.15}$$

Eqn. 4.1 can be transformed to:

$$\alpha_0 \;=\; \frac{N_t}{\alpha_A \cdot N_b} \tag{4.16}$$

The sky map in Figure 4.13 shows $\log_{10}(\alpha_0)$ calculated within an oversampling radius[3] of $r_o = 0.12°$ and the distribution over all bins of the map. The logarithm is used, because it transforms the α_0 distribution to a symmetric distribution. The mean value of the distribution is $3.6 \cdot 10^{-4}$, which corresponds to $\alpha_0 = 1.001$ and reproduces the darkfield assumption $N_{ex} = 0$ very well. In this example the background run selection has been

[3]For the definition of the oversampling radius r_o, see Section 5.3.

Table 4.2: The table lists the α_0 from the analysis of the darkfield in the declination band $[-15°, -25°]$. The darkfields has been tested using three sets of run parameters to generate a background list combined with three methods handling the atmospheric conditions (none, R/R_{est}, run selection).

declination band	background run association	exposure	correction method	α_0
$-15°$	φ_Z, ϵ_μ	62 pairs	none	0.943
to	φ_Z, ϵ_μ	62 pairs	R/R_{est}	1.001
$-25°$	φ_Z, ϵ_μ, R/R_{est}	62 pairs	run selection	1.038
(MC: south)	φ_Z, ϕ_A, ϵ_μ	47 pairs	none	1.096
	φ_Z, ϕ_A, ϵ_μ	47 pairs	R/R_{est}	1.026
	φ_Z, ϕ_A, ϵ_μ, R/R_{est}	45 pairs	run selection	1.050
	φ_Z, ϕ_A, ϵ_μ, T_C, N_{BP}	47 pairs	none	1.086
	φ_Z, ϕ_A, ϵ_μ, T_C, N_{BP}	47 pairs	R/R_{est}	1.017
	φ_Z, ϕ_A, ϵ_μ, T_C, N_{BP}, R/R_{est}	43 pairs	run selection	1.056

restricted to weighting factors on the zenith angle φ_Z and the optical efficiency ϵ_μ. The R/R_{est} correction Eqn. 4.9 was applied, resulting in $\alpha_{A,cor} = 1.050$.

Three sets of weighting parameters for the background run selection are tested for each darkfield. The weighting parameters are summarized in Table 4.3. The first set consists of the zenith angle φ_Z and the optical efficiency ϵ_μ. In the second set, the azimuth angle ϕ_A is added. The camera temperature T_C and the number of broken pixels N_{BP} are included in the third set. All these parameters are defined in Section 4.2 as mean parameters for the full four-telescope array, time-averaged over the observation run. The generation of the OnOff runlists is fully automatic. OnOff run pairs with a large deviation in zenith angle or the optical efficiency are removed from the run list, at which the corresponding cuts are also given in Table 4.3. A further selection criterion to be imposed on the OnOff pairs is the energy threshold achieved in the observation runs. The darkfield analysis is restricted to events with a reconstructed γ-ray energy larger than 750 GeV. OnOff run pairs are removed from the automatic runlist, if the threshold of the On target or the background run is higher than the 750 GeV.

The three runlists for a darkfield are analyzed with the different correction methods for atmospheric fluctuations, as discussed before. The first method is the rescaling of α_A using the ratio between the CTS rate and the estimated trigger rate R/R_{est}. In the second method, R/R_{est} is used in the background run selection algorithm. The results for the example darkfield at a declination of $\sim 20°$ are summarized in Table 4.2. The number of remaining runs in the OnOff list after selection of the associated pairs and the corresponding value of α_0 are given. If no correction for atmospheric fluctuations is applied the background events are misestimated by +6 % (0.943) to −10 % (1.096). Beyond the atmosphere correction, no significant improvement can be seen for the run list based on the φ_Z and ϵ_μ parameters in comparison to the lists based on all five association parameters.

Table 4.3: The table presents the weighting factors w_i for the selection parameters in the background run selection algorithm. The weighting factors have been determined in Section 4.2. In the last column a cut is proposed which can be applied on the difference in the selection parameter within a run pair to reject pairs where the association failed.

parameter			w_i	cut
zenith angle	φ_Z	[deg]	$0.15\,{}^{1}/_{\text{deg}}$	3°
optical efficiency	ϵ_μ	[1]	-6	0.005
azimuth angle	ϕ_A	[deg]	$0.001\,{}^{1}/_{\text{deg}}$	
number of broken pixels	N_{BP}	[#]	$-0.002\,{}^{1}/_{\text{Pixel}}$	
camera temperature	T_C	[°C]	$-0.006\,{}^{1}/_{\text{°C}}$	

The approach of the darkfields test can be summarized as follows: Test regions with a high exposure and the absence of TeV γ-rays sources (darkfields) are considered. An exposure ratio α_0 that is required to realize the exact sourceless hypothesis in the test region is derived in addition to all known/described correction methods for background event rates. The entire ensemble of darkfields is listed in the Tables 4.4 and 4.5. The four darkfields of in Table 4.4 culminate in the north of the telescopes array. The lookups for the event reconstruction were exchanged by lookups produced with MC simulations of point sources in the northern sky. All darkfields behave similarly to the discussed example. The results of the darkfield analysis can be summarized as follows:

- OnOff Background models using a background run association based only on the parameters zenith angle and optical efficiency can exhibit misestimates of the background up to ± 20 %.
- The discussed correction methods for background rates are able to reduce the misestimates to a level of ± 5 %. Further quantification of this remaining misestimate in dependency of the number of runs can not be given here.
- An improvement of the consistence in the background rate of the darkfield runs and the associated background runs using the azimuth angle, the number of broken pixels and the camera temperature in the association algorithm could not be proven.

Table 4.4: The table lists the α_0 from the analysis of four darkfields. For each darkfield, OnOff lists were tested using three sets of run parameters combined with three methods handling the atmospheric conditions (none, R/R_{est}, run selection). The targets in the middle of the listed darkfields culminates in northern direction of the H.E.S.S. array.

declination band	background run association	exposure	correction method	α_0
25°	φ_Z, ϵ_μ	66 pairs	none	0.998
to	φ_Z, ϵ_μ	66 pairs	R/R_{est}	1.009
15°	φ_Z, ϵ_μ, R/R_{est}	66 pairs	run selection	0.984
(MC: north)	φ_Z, ϕ_A, ϵ_μ	44 pairs	none	0.990
	φ_Z, ϕ_A, ϵ_μ	44 pairs	R/R_{est}	0.992
	φ_Z, ϕ_A, ϵ_μ, R/R_{est}	46 pairs	run selection	0.997
	φ_Z, ϕ_A, ϵ_μ, T_C, N_{BP}	46 pairs	none	1.016
	φ_Z, ϕ_A, ϵ_μ, T_C, N_{BP}	46 pairs	R/R_{est}	1.005
	φ_Z, ϕ_A, ϵ_μ, T_C, N_{BP}, R/R_{est}	47 pairs	run selection	0.989
15°	φ_Z, ϵ_μ	52 pairs	none	1.163
to	φ_Z, ϵ_μ	52 pairs	R/R_{est}	1.062
5°	φ_Z, ϵ_μ, R/R_{est}	52 pairs	run selection	1.062
(MC: north)	φ_Z, ϕ_A, ϵ_μ	31 pairs	none	1.084
	φ_Z, ϕ_A, ϵ_μ	31 pairs	R/R_{est}	0.996
	φ_Z, ϕ_A, ϵ_μ, R/R_{est}	32 pairs	run selection	0.959
	φ_Z, ϕ_A, ϵ_μ, T_C, N_{BP}	26 pairs	none	1.057
	φ_Z, ϕ_A, ϵ_μ, T_C, N_{BP}	26 pairs	R/R_{est}	0.954
	φ_Z, ϕ_A, ϵ_μ, T_C, N_{BP}, R/R_{est}	27 pairs	run selection	1.012
5°	φ_Z, ϵ_μ	117 pairs	none	1.025
to	φ_Z, ϵ_μ	117 pairs	R/R_{est}	1.038
−5°	φ_Z, ϵ_μ, R/R_{est}	120 pairs	run selection	1.029
(MC: north)	φ_Z, ϕ_A, ϵ_μ	101 pairs	none	1.012
	φ_Z, ϕ_A, ϵ_μ	101 pairs	R/R_{est}	1.013
	φ_Z, ϕ_A, ϵ_μ, R/R_{est}	93 pairs	run selection	0.987
	φ_Z, ϕ_A, ϵ_μ, T_C, N_{BP}	101 pairs	none	1.005
	φ_Z, ϕ_A, ϵ_μ, T_C, N_{BP}	101 pairs	R/R_{est}	1.016
	φ_Z, ϕ_A, ϵ_μ, T_C, N_{BP}, R/R_{est}	96 pairs	run selection	0.976
−5°	φ_Z, ϵ_μ	70 pairs	none	0.982
to	φ_Z, ϵ_μ	70 pairs	R/R_{est}	1.030
−15°	φ_Z, ϵ_μ, R/R_{est}	72 pairs	run selection	0.990
(MC: north)	φ_Z, ϕ_A, ϵ_μ	64 pairs	none	0.989
	φ_Z, ϕ_A, ϵ_μ	64 pairs	R/R_{est}	1.035
	φ_Z, ϕ_A, ϵ_μ, R/R_{est}	59 pairs	run selection	0.993
	φ_Z, ϕ_A, ϵ_μ, T_C, N_{BP}	64 pairs	none	1.001
	φ_Z, ϕ_A, ϵ_μ, T_C, N_{BP}	64 pairs	R/R_{est}	0.986
	φ_Z, ϕ_A, ϵ_μ, T_C, N_{BP}, R/R_{est}	57 pairs	run selection	1.051

Table 4.5: The table lists the α_0 from the analysis of three darkfields. For each darkfield, OnOff lists were tested using three sets of run parameters combined with three methods handling the atmospheric conditions (none, R/R_{est}, run selection). The targets in the middle of the listed darkfields culminates in southern direction of the H.E.S.S. array.

declination band	background run association	exposure	correction method	α_0
$-25°$	φ_Z, ϵ_μ	225 pairs	none	0.992
to	φ_Z, ϵ_μ	225 pairs	R/R_{est}	1.036
$-35°$	φ_Z, ϵ_μ, R/R_{est}	226 pairs	run selection	1.010
(MC: south)	φ_Z, ϕ_A, ϵ_μ	137 pairs	none	0.978
	φ_Z, ϕ_A, ϵ_μ	137 pairs	R/R_{est}	1.047
	φ_Z, ϕ_A, ϵ_μ, R/R_{est}	122 pairs	run selection	1.010
	φ_Z, ϕ_A, ϵ_μ, T_C, N_{BP}	133 pairs	none	0.986
	φ_Z, ϕ_A, ϵ_μ, T_C, N_{BP}	133 pairs	R/R_{est}	1.036
	φ_Z, ϕ_A, ϵ_μ, T_C, N_{BP}, R/R_{est}	126 pairs	run selection	0.989
$-35°$	φ_Z, ϵ_μ	208 pairs	none	0.982
to	φ_Z, ϵ_μ	208 pairs	R/R_{est}	0.942
$-45°$	φ_Z, ϵ_μ, R/R_{est}	206 pairs	run selection	0.949
(MC: south)	φ_Z, ϕ_A, ϵ_μ	137 pairs	none	1.029
	φ_Z, ϕ_A, ϵ_μ	137 pairs	R/R_{est}	0.965
	φ_Z, ϕ_A, ϵ_μ, R/R_{est}	130 pairs	run selection	0.966
	φ_Z, ϕ_A, ϵ_μ, T_C, N_{BP}	132 pairs	none	1.026
	φ_Z, ϕ_A, ϵ_μ, T_C, N_{BP}	132 pairs	R/R_{est}	0.947
	φ_Z, ϕ_A, ϵ_μ, T_C, N_{BP}, R/R_{est}	133 pairs	run selection	0.969
$-45°$	φ_Z, ϵ_μ	30 pairs	none	0.977
to	φ_Z, ϵ_μ	30 pairs	R/R_{est}	0.969
$-55°$	φ_Z, ϵ_μ, R/R_{est}	31 pairs	run selection	0.949
(MC: south)	φ_Z, ϕ_A, ϵ_μ	27 pairs	none	0.991
	φ_Z, ϕ_A, ϵ_μ	27 pairs	R/R_{est}	0.990
	φ_Z, ϕ_A, ϵ_μ, R/R_{est}	24 pairs	run selection	0.986
	φ_Z, ϕ_A, ϵ_μ, T_C, N_{BP}	27 pairs	none	1.013
	φ_Z, ϕ_A, ϵ_μ, T_C, N_{BP}	27 pairs	R/R_{est}	0.993
	φ_Z, ϕ_A, ϵ_μ, T_C, N_{BP}, R/R_{est}	24 pairs	run selection	0.972

Chapter 5

Technical Aspects of Flux Estimates

So far, the analysis of H.E.S.S. observational data and the handling of remaining background events has been discussed. Two analytical tools for the analysis with the OnOff background model will be presented here. They allow to display estimates of the γ-ray flux in spectral plots and sky maps.

5.1 Determination of γ-Ray Source Significances

An important point for the validation of a positive excess N_{ex} (Eqn. 4.2) as a source of TeV γ-rays is the significance of the signal. Li & Ma [80] discussed two approaches for the determination of the significance. The first one, Li and Ma's formula (9) is the propagated standard deviation of the Poisson distributed On target counts N_t and the background counts N_b:

$$\sigma\left(N_t, N_b, \alpha\right) \;=\; \frac{N_t - \alpha \cdot N_b}{\sqrt{\alpha \cdot (N_t + N_b)}} \tag{5.1}$$

Li and Ma showed that the significance will be overestimated for $\alpha > 1$ and underestimated for $\alpha < 1$. For the OnOff background this usually will not happen as the exposure ratio α is generally $\sim$1. However, the H.E.S.S. analysis software makes use of the second approach, which is therefore relevant for the analysis results presented in Chapter 6 of this thesis. The significance will be calculated exactly, testing the null hypothesis that the test region doesn't contain any γ-ray source and the excess counts originate from fluctuations of the background with the maximum likelihood ratio. The result is Li and Ma's formula (17):

$$\sigma\left(N_t, N_b, \alpha\right) \;=\; \sqrt{2N_t \cdot \ln\left[\frac{1+\alpha}{\alpha} \cdot \frac{N_t}{N_t + N_b}\right] + 2N_b \cdot \ln\left[(1+\alpha) \cdot \frac{N_b}{N_t + N_b}\right]} \tag{5.2}$$

Estimating Confidence Intervals for the γ-Rays Flux

The evaluation of the confidence intervals for the number of excess N_{ex} (Eqn. 4.1) poses a problem similar to that of the significance determination. For large count numbers from the On target N_t and background N_b data, the error on the excess events can be derived with the rules of uncertainty propagation by assuming Poisson distribution of N_t and N_b (Eqn. 4 in [80]):

$$\Delta N_{ex} = \sqrt{N_t + \alpha^2 \cdot N_b} \tag{5.3}$$

Below, γ-ray flux will be calculated by dividing the number of excess events by an exposure (Eqn. 5.10). Thereby, uncertainties of the exposure are neglected in the first instance[1], so that the relative error on N_{ex} is also the relative error of the flux estimate. In case of small count numbers, the probability density function P that the actual signal N_{ex} and the expected background counts B were measured as N_t and N_b should be considered:

$$P\left(N_{ex}, B\right) = \frac{\left(N_{ex} + \alpha \cdot B\right)^{N_t}}{N_t!} \cdot \exp\left(-\left(N_{ex} + \alpha \cdot B\right)\right) \cdot \frac{B^{N_b}}{N_b!} \cdot \exp\left(-B\right) \tag{5.4}$$

To reduce this approach to a probability density function with a dependence only on the signal, an estimate for the background counts is required. As a solution for the case of an exposure ratio larger than 1, N_b itself can be utilized as estimator. However, for the OnOff background model, the exposure ratio is almost 1. Hence, the most likely background counts for a constant signal can be used:

$$\frac{\mathrm{d}P\left(N_{ex} = const, B_{max}\right)}{\mathrm{dB}} = 0 \tag{5.5}$$

which yields:

$$B_{max}\left(N_{ex}\right) = \frac{1}{\alpha^2 + \alpha} \cdot \left(\frac{t}{2} + \sqrt{\frac{t^2}{4} + \left(\alpha^2 + \alpha\right) \cdot N_b \cdot N_{ex}}\right) \tag{5.6}$$

$$t = \alpha\left(N_t + N_b\right) - \left(\alpha + 1\right) \cdot N_{ex} \tag{5.7}$$

The resulting probability density function is not symmetric. The final error estimations ΔN_{ex}^- and ΔN_{ex}^+ are derived by scanning P for:

$$P\left(N_{ex} - \Delta N_{ex}^-, B_{max}\left(N_{ex} - \Delta N_{ex}^-\right)\right) = \frac{1}{2} \cdot P\left(N_{ex}, B_{max}\left(N_{ex}\right)\right) \tag{5.8}$$

$$P\left(N_{ex} + \Delta N_{ex}^+, B_{max}\left(N_{ex} + \Delta N_{ex}^+\right)\right) = \frac{1}{2} \cdot P\left(N_{ex}, B_{max}\left(N_{ex}\right)\right) \tag{5.9}$$

In the H.E.S.S. analysis software, this final estimate for the errors is applied as standard. For the subsequent presentation of the analysis results for the Vela X data, differences

[1] A discussion of the systematic errors of the flux estimate including the effects of the exposure determination can be found in Section 6.3.5.

between both approaches for the error estimate (Eqn. 5.3 and Eqn. 5.8, 5.9) are relevant in two or three bins including the highest energy events of the spectral energy distributions (Fig. 6.5, 6.6, 6.7 and 6.8). For the error estimation of the low-energy bins of the spectra and the flux profiles (Fig. 6.10 and 6.10) the Poisson (Eqn. 5.3) approach is sufficient. In case of a negative excess of a flux point, the error is calculated for the assumption that the background data contain a γ-ray source and the on target data is background. One has to note, that the description follows the implementation in the H.E.S.S. analysis software that has been often used over the past years. Thereby negative signals N_{ex} in P are allowed. A second inexactness of the ansatz in Eqn. 5.8 and 5.9 is, that a Gaussian approximation of P is assumed for the half maximum probabilities to determine N_{ex}^{-} and N_{ex}^{+}, instead of integrating P over the confidence interval.

5.2 Evaluation of Flux Spectra

The procedure to extract the γ-ray photon flux spectrum from a test region applying the OnOff background model is similar to the extraction of a spectrum with other background models (reflected background, ring background). A good description of the determination of a flux spectrum has been given by S. Hoppe [65]. The algorithm presented here will follow his method A, with some adaptations due to a customization to the OnOff model, a change of the underlying analysis framework and the extension of Vela X. The method assumes that the bias between the photon's primary energy and the reconstructed energy (see Fig. 3.9(b)) is negligible. Another restriction made in systematic studies of the background in Section 4.2 and the characterization of the γ-ray events in Section 3.4 concerns the limit in the offset to the observation direction $\psi \leq 2.0°$. Above 2.0° the energy reconstruction and the point spread function deteriorate and the dependency on background rates becomes more complicated. Therefore, the analysis presented here is restricted to events with offsets smaller than 2.0°.

The starting point for the determination of the γ-ray flux f within an energy bin dE_i is the number of γ-ray excess counts $N_{ex,i}$ in this energy bin (Eqn. 4.1). $N_{ex,i}$ will be normalized with the exposure-weighted detection area $A_{t,i}^{*}$:

$$f_i = N_{ex,i} \cdot \frac{1}{A_{t,i}^{*}} \cdot \frac{1}{\mathrm{dE}_i} \tag{5.10}$$

The energy range is split up into bins of equal size on a logarithmic scale while the bins are signed with the index i. The number of bins per decade is chosen depending on the strength of the γ-ray signal and its ratio to the background. Later on 6 to 8 bins per decade will be used. As the observation data is organized in runs (with a duration of 28 min), the strategy to merge these runs is to sum up the quantities of Eqn. 4.1 and 5.10. The number of events in the test regions is:

$$N_{t,i} = \sum_{r \in on} N_{i,r} \tag{5.11}$$

The run number of a single run is termed here with the symbol r. The total number of events in the corresponding regions of the background runs is:

$$N_{b,i} = \sum_{r \in off} N_{i,r} \tag{5.12}$$

To fulfill the assumption that the energy bias for the reconstructed energy is negligible an event-selection cut at the lower analysis threshold t_a in the reconstructed energy has to be applied. As discussed before, the threshold is defined as the energy of MC γ-rays where the energy reconstruction overestimates the simulated energy by more than 10 % (Sec. 3.4.1). The thresholds t_a are determined with predefined optical efficiency ϵ_{MC} in the MC simulations. For each run, t_a is corrected by the ratio of the average ϵ_μ over the telescopes and ϵ_{MC} analogously to the correction of the reconstructed energy (see Eqn. 3.23). In the OnOff background model the t_a for a pair of On target and background runs is determined by the higher one out of the two individual threshold values. In case of the OnOff background, it should be also proven that the subtraction of γ-like background also works for all reconstructed energies down to the applied energy cut. Looking at the background curve shown in Figure 4.1(a), an obvious criterion for a lower energy threshold that should not be under-run by the OnOff background subtraction is the energy t_b where the background rate peaks. The background rates on the falling edge for energies below t_b can vary strongly between On target runs and background runs and the γ-ray signal-to-background ratio is rather low at these energies. For the reconstruction method and the standard selection cuts introduced in Section 3.3, the threshold defined by the peak energy t_b is in the same order as the analysis threshold t_a. A comparison of both thresholds can be found in Table 3.3. Technically the threshold is implemented by resetting the $N_{i,r}$ and $A_{r,i}$ in the bins below the threshold to zero.

The effective areas, available from lookup tables, have been introduced in Section 3.4.2. They will be used here in their interpolated version and corrected for the mean muon efficiency of the four telescopes in each run (Eqn. 3.43). The effective area at the center energy of a bin E_i is $A_i(\varphi_Z, \psi)$. Largely extended regions may cover several degrees in the zenith angle φ_Z and in the offset angle ψ. During an observation run, the zenith will change as well, while the telescopes tracks the target position in the sky. To derive the effective area of a test region in a run, the coverage distribution of the test region $D_{z,o}$ in φ_Z and ψ is evaluated. Therefor the sky is spanned by a grid and all grid points which are included in the test region are counted. The run is split up into time intervals and the scan is repeated for all time intervals. The coverage distribution for a run will be normalized to 1:

$$1 = \sum_{z,o} D_{z,o} \tag{5.13}$$

The determination of the coverage distribution is illustrated in Figure 5.1. An observation run in the northeast of Vela X is used as example. The pointing position of the run

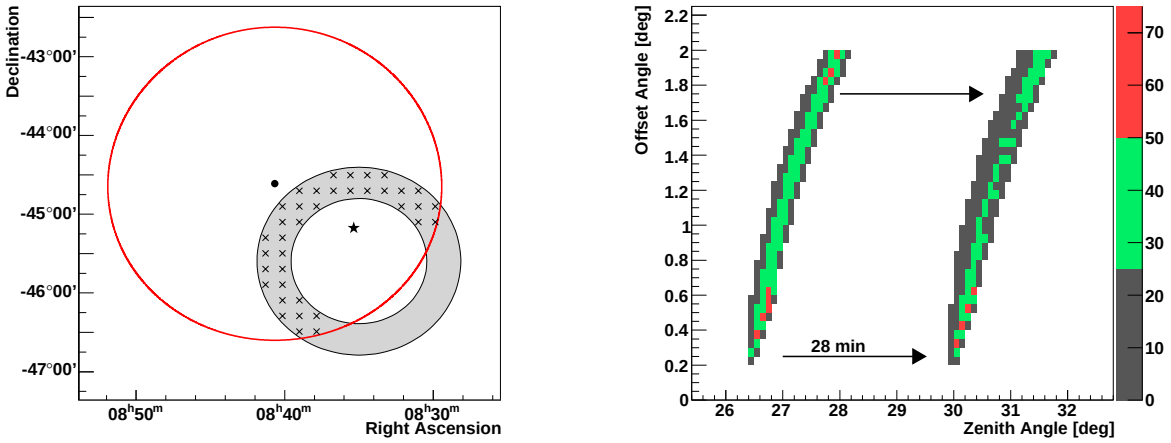

(a) sky-map (b) zenith-offset distribution

Figure 5.1: a) The sky-map sketches the determination of the zenith-offset coverage distribution by a scan over the solid angle for a test region in an observation run next to Vela X (*No. 49831*). A detailed description is given in the text. b) The resulting zenith-offset distribution for a scan at the beginning and the end of the observation run.

at RA $= 08^h40^m40^s$, Dec $= -44°36'40''$ is indicated with a black dot and the maximum offset for events of $\psi \leq 2.0°$ is drawn as red circle. The test region is a ring (0.8° to 1.2°) filled in gray and the position of the Vela Pulsar is indicated by a black star. A scan with a step size of 0.02° is carried out on the field of view in the sky. In the sketch, the scanning grid was enlarged to 0.2° for better visualization and the grid points that are included in the ψ-cut and the test region are marked by the crosses. In Figure 5.1(b) the zenith offset distribution $D_{z,o}$ is shown for a first scan at the beginning and a second scan at the end of the run. In the data analysis typically 20 scans are performed per run. This approach will necessarily leave in the zenith-offsets distributions. However the offset and zenith steps in the production of the effective areas from MC simulations are even wider, so that these holes will not introduce considerable systematics in the flux estimate. The effective area for the energy bin i of a test region in a run is:

$$A_{i,r} \quad = \quad \sum_{z,o} D_{z,o} \cdot A_i \left(\varphi_Z, \psi_o\right) \tag{5.14}$$

Also important for the calculation of a run's exposure contributed to the flux estimate of test region is the effective size of test region. For large test regions (as it is the case for Vela X) the test region can exceed above the field of view, defined by the ψ-cut. The effective size of test region s_r is defined as cross section between the field of view of a run and the entire test region. For the run in Figure 5.1, the resulting effective size of the test region s_r is 1.54 deg^2 while the complete ring covers 2.51 deg^2.

The effective area for the complete data set is the exposure-weighted sum of the effective areas of the individual runs. The exposure is determined by the deadtime-corrected

observation duration t_r and the effective size of the test region s_r:

$$A^*_{t,i} = \sum_{r \in on} A_{i,r} \cdot t_r \cdot s_r \tag{5.15}$$

As $A^*_{t,i}$ is normalized to the size of the test region, the resulting f_i (Eqn. 5.10) is a so-called surface flux. The unnormalized flux is derived by multiplying f_i with the size of the entire test region.

Model Fits to the Data Points

The final data points will be fitted with simple models using a χ^2 minimization. The spectral distribution of the TeV photon flux from γ-ray sources can declines over several decade along a power law. As for many source the exposure only allows to determine four or five flux points, the pure power-law fits are prominent models with a normalization N_0 and the positive photon index γ as free parameters:

$$f_{pl}(E) = N_0 \cdot \left(\frac{E}{\mathrm{TeV}}\right)^{-\gamma} \tag{5.16}$$

The assumed generation process for pulsar nebulae that are observable in TeV (power-law injection, synchrotron cooling of the leptonic plasma, TeV γ-rays photons via Inverse Compton) will maintain a power-law spectrum with exponential cutoff in the TeV range:

$$f_{cut}(E) = N_0 \cdot \left(\frac{E}{\mathrm{TeV}}\right)^{-\gamma} \cdot \exp\left(-\frac{E}{E_{cut}}\right) \tag{5.17}$$

Due to the large changes in the flux level over the wide bins in energy, the center of the energy bin E_i is not the energy corresponding to the measured flux f_i. The data points are shifted on the abscissa following the procedure describen in Reference [77] and using the model from a first fit. A final fit is applied on the shifted data points. In principle, this is a recursive approach, but usually the second step is already stable.

5.3 The Art of Flux Maps

The energy-integrated γ-ray flux depending on the positions in the sky is calculated in a similar way as the spectrum. The events are counted in spatial bins with the two dimensions on the sky instead of spectral bins. The number of events in a bin of the On target runs is (run index r):

$$N^t_{x,y} = \sum_{r \in on} N_{x,y,r} \tag{5.18}$$

The number of events in a bin of the background runs is:

$$N^b_{x,y} = \sum_{r \in off} N_{x,y,r} \tag{5.19}$$

The background exposure ratio α_A is assumed to be constant within a pair of On target and background run over the field of view and the energy. In case of the OnOff background model the exposure ratio is given by the ratio of the deadtime-corrected observation duration between the On target and the background run and, if applied, by the correction for atmospheric influences (Eqn. 4.9). In principle, the background depends on the offset to the observation direction and the zenith angle (see Fig. 4.2), so that differences in the zenith angle for On target and background runs can introduce a spatial dependency of the exposure ratio. However, the influence of such spatial dependencies on the excess calculation is rather small, so that these effects are neglected. The background ratio will be averaged over all run pairs:

$$N^{ex}_{x,y} = \sum_{x,y \in r_o} N^t_{x,y} - \langle \alpha_{A,r} \rangle_{pairs} \cdot N^b_{x,y} \tag{5.20}$$

This relation includes an oversampling radius r_o that is an option in the generation of flux maps. All bins around the x, y bin within the oversampling radius are summed up in the On target count maps, background count maps and the exposure maps. The oversampling will maintain a correlated flux map.

The conversion of the excess counts into a flux requires an estimate of the γ-ray exposure. A simple approach assumes that the acceptance of γ-ray events with an increasing offset angle behaves like the triggers of γ-like background events. This implies that the background acceptances curves (Fig. 4.2) can be used also for the estimate of the γ-ray exposure. The results are so-called "acceptance-corrected excess maps", where the acceptance-corrected excess is proportional to the γ-ray flux. The simple approach is superseded here by a more complex one using the γ-ray trigger acceptance from MC simulations. The exposure is estimated using the number of expected γ-ray events. Therefor the shape of the spectral flux of the γ-source in the field of view has to be assumed a priory. The spectral flux $\mathrm{d}N/\mathrm{dE}$ folded with the effective area (Eqn. 3.43) yields the γ-ray exposure $\Theta^r_{x,y}$ in the bin x, y for the run with the index r:

$$\Theta^r_{x,y} = t \cdot N_A \cdot \int_{E_{min}}^{E_{max}} A_r \left(E, \epsilon_{\mu,r}, \varphi_{Z,x,y}, \psi_{x,y}\right) \cdot \frac{\mathrm{d}N}{\mathrm{dE}}(E) \cdot \mathrm{dE} \tag{5.21}$$

The averaging over all runs is done in a similar fashion as for the excess counts (Eqn. 5.20). If an oversampling radius has been applied in the averaging of the excess counts, it is also required for the exposure estimation of the bins:

$$\Theta_{x,y} = \sum_{x,y \in r_o} \Theta^r_{x,y} \tag{5.22}$$

The final flux estimate for a bin in the sky is:

$$F_{x,y} = \frac{N^{ex}_{x,y}}{\Theta_{x,y}} \cdot N_A \cdot \int_{E_{min}}^{E_{max}} \frac{\mathrm{d}N}{\mathrm{dE}}(E) \cdot \mathrm{dE} \tag{5.23}$$

The flux $F_{x,y}$ is calculated per bin (or in case of oversampling: per bin and its surrounding), so that the flux map depends on the bin size s_b. The bin size corrected flux is called surface flux:

$$S_{x,y} = F_{x,y} \cdot \frac{1}{s_b} \tag{5.24}$$

An Example of a Flux Map

In the Introduction, a surface flux sky map has been shown (Fig. 1.2). It will be used here as an example illustrating flux maps. The map includes Vela X on the right and the SNR VelaJr on the left side. Observational data on Vela X (for details see Sec. 6.1) and on VelaJr were used to generate this map. In total, there are 316 runs with an observation time of 136.9 h included in this map. All of these runs fulfill a lower energy threshold of 750 GeV. The energy threshold is used as lower integration bound for the flux estimate and events are taken into account only, if their reconstructed energy exceeds the lower limit.

For the assumption of the spectral flux shape, one has to consider the relatively hard spectrum of Vela X, here simplified using a power law with an index of 1.7. For the surroundings of Vela X, a common power-law index 2.5 is used. A compromise between these two spectra is that in a sphere with the radius of 1.6° around Vela X where beyond the softer index is used and in between the harder ones:

$$\frac{\mathrm{d}N}{\mathrm{dE}} \propto \begin{cases} \left(\frac{E}{\mathrm{TeV}}\right)^{-1.7} & \text{Vela X and surrounding} \\ \left(\frac{E}{\mathrm{TeV}}\right)^{-2.5} & \text{remaining map} \end{cases} \tag{5.25}$$

The spectral index of Vela Junior was derived to be $\Gamma = 2.24 \pm 0.04_{stat} \pm 0.15_{syst}$ [10]. The systematic overestimation using the softer index 2.5 for the flux above 750 GeV is ∼4 %. In case of Vela X where the index of 1.7 is a good assumption for the measured spectrum with an index of 1.3 and a cutoff of 13 TeV (Tab. 6.3). The systematic overestimate is as well in the order of 4 %.

Sky maps of TeV γ-ray data are typically tunned to allow the viewer to see only objects and features in the map which can be established by more exact procedures. The typical tools to change the impression that a sky map conveys are the size of the correlation radius (here oversampling radius) and the choice of the color scale. The oversampling radius was set to $r_o = 0.12$ deg. The transient between gray and black shades and blue has been set to a level of $5 \cdot 10^{-12}$ cm^{-2}s^{-1}deg^{-2}, which corresponds a level of about 2σ.

Another cleanup that was applied to the flux map is defined by the requirement of a minimal γ-exposure for each bin. A bin is rejected, if its exposure goes below 20 % of the maximal bin exposure (here in the inner region of Vela X). This cleanup avoids that small exposure values will give rise to insignificant flux hot spots at the edge of the flux map.

Chapter 6

The Analysis of the H.E.S.S. Observation of Vela X and its Results

In this Chapter, the analysis results of the H.E.S.S. data on Vela X are presented. The main part of the results is based on the background estimation with the OnOff model using non-dedicated background runs. The pointing positions of one fourth of the data set has been chosen such that the reflected background model can be applied. This allows a cross check of the results obtained with the OnOff model. It will be shown that the suggested correction for atmospheric conditions using the R/R_{est} ratio of On target and background runs (Eqn. 4.9) yield more consistent results in comparison with an analysis that neglects the atmosphere.

First, the data set on Vela X itself will be presented, followed by a claim of extended emission around the previously used integration region and a discussion of the spectrum and morphology. The morphological results of the analysis published by the H.E.S.S. collaboration in 2006 [6] are used here as a starting point. In particular, these are a suggested center for the TeV flux termed "position II" at RA $= 08^h35^m00^s$, Dec $= -45°36'00''$ (J2000) and the radius of 0.8° as integration region for the extraction of a spectrum. The 0.8° region corresponds to a test region, where the TeV flux is supposed to be connected to the X-ray emission from the jet-like feature.

Within the H.E.S.S. collaboration, it is aspired that an analysis result is confirmed by a second independent analysis chain. For Vela X, the second analysis was described by F. Dubois [42]. The main difference to the analysis used in this thesis is the set of events selection cuts to separate the γ-ray events from the hadronic background. F. Dubois proposed a combination of existing separation cuts, hereafter referred to Xeff cuts. Using the Xeff cuts, a larger fraction of the γ-ray events pass the events selection, although there is also a slight increase of the γ-like background events. Hence, the analysis with the Xeff cuts is more sensitive for the detection of γ-rays. A caveat for the Xeff cuts combining them with the OnOff background model is that the systematic effects based on the atmospheric observation conditions will be amplified by the larger amount of the γ-like

background events. In the following, the results of F. Dubois will be compared with the results obtained in this thesis. Based on the Xeff analysis, preliminary results on the entire Vela X data set were reported for the H.E.S.S. collaboration [43]. At the moment, a final statement on the analysis results for Vela X from the H.E.S.S. collaboration is pending.

Another observation of TeV γ-rays from Vela X was performed with the first phase of the CANGAROO experiment from 1993 to 1995. The data has been reanalyzed in 2009 in regard of the H.E.S.S. publication from 2006. For a test region corresponding to the inner test region, the flux above 2.5 TeV was found to be $3.05 \cdot 10^{-12}$ cm^{-2} s^{-1} [105]. Assuming the spectral shape that was reported by the H.E.S.S. collaboration, the integrated flux can be expanded down to a lower integration bound of 1 TeV. The extrapolated integrated flux as seen by CANGAROO is then $10.6 \cdot 10^{-12}$ cm^{-2} s^{-1}. Within the given error for the lower bound of the integration range of ± 1.6 TeV, the CANGAROO flux is consistent with all other results which are presented below, so that it will not be further discussed.

6.1 The H.E.S.S. Observation History of Vela X

Since the construction of the four-telescope array was finished in 2003, the Vela X was a source of interest for the H.E.S.S. experiment. The size of the TeV nebula was not known before the H.E.S.S. observations. So that, during the last five years, the observation strategy was revised several times, in each case affected by preliminary results obtained from the ongoing observation campaign. The available data set is summarized in Table 6.1 and the pointing positions are indicated on a sky map in Figure 6.1(a). Vela X is visible for H.E.S.S. around the turn of the years, so that the runs are grouped in seasons from August to July. The table compares the complete data with the reduced data, that passed the three run selection criteria (broken pixels, atmosphere and clouds). Most of the rejected runs suffer from a cloudy sky.

The circumstances of the observations in the different seasons were the following: In the first season (2003/04), the target of the observation was the pulsar itself. The runs are taken 0.5° to the north and to the south of the pulsar. This strategy called wobble mode optimizes the data set for extracting a spectrum from the pulsar with the reflected background model[1]. A combined campaign for Vela X and the nearby SNR Vela Junior took place in 2004/05. In each turn, a dedicated background run, a run on Vela X and one on Vela Junior with equivalent zenith angles were taken. Unfortunately, the weather conditions were not perfect during that season. Typically either the run pointing at Vela X or the dedicated background run was affected by clouds. The target positions in 2006/07 were chosen at a distance of 0.9° to the TeV centroid in horizontal and vertical direction. If the source extension would be restricted to 0.8°, as published in 2006, these positions would allow reflected background extraction regions. The first observations in 2007/08

[1]To allow the reflected background model to be used the condition has to be fulfilled, that the reflected background regions are not contaminated by TeV γ-ray sources.

Table 6.1: The table lists the available four-telescope H.E.S.S. observation data targeting Vela X. For each observation season, the number of runs and the resulting observation duration t_{obs} are given before and after run quality selection, as well as the mean zenith angle $\langle\varphi_Z\rangle$, the rate ratio $\langle R/R_{est}\rangle$, mean muon factor $\langle\epsilon_\mu\rangle$ and number of broken pixels $\langle N_{BP}\rangle$.

season	runs all	(t_{obs})	passed cuts	(t_{obs})	$\langle\varphi_Z\rangle$ $[deg]$	$\langle R/R_{est}\rangle$	$\langle\epsilon_\mu\rangle$	$\langle N_{BP}\rangle$
2003/04	49	(21.3 h)	26	(12.2 h)	27.83	1.41	0.0904	23.7
2004/05	24	(9.9 h)	15	(6.9 h)	27.83	1.19	0.0789	29.4
2005/06	5	(2.1 h)	-					
2006/07	55	(25.2 h)	51	(23.5 h)	25.03	1.15	0.0712	49.0
2007/08	11	(4.4 h)	8	(3.5 h)	23.97	0.95	0.0647	40.9
2008/09	50	(22.1 h)	31	(14.3 h)	24.19	1.11	0.0639	61.1
all	194	(85.0 h)	131	(60.3 h)	26.51	1.19	0.0738	44.1

point to the middle of the ring extension. In the second part of season 2007/08 and in 2008/09 the observation runs were taken at three positions which allow to use the reflected background method also for the larger ring extension.

Table 6.1 includes the mean zenith angle $\langle\varphi_Z\rangle$, mean R/R_{est} ratio, the mean muon factor $\langle\epsilon_\mu\rangle$ and the mean number of broken pixels $\langle N_{BP}\rangle$. Thus, it displays a problem of the Vela X data set: The R/R_{est} ratio is considerably larger than 1. If the rate ratio of the background runs is ignored in an OnOff analysis, an underestimation of the background up to 20 % can be assumed from the shown dependency of the background rate on the rate ratio (Eqn. 4.8). The observation runs of the first season possess an extraordinarily high R/R_{est} at 1.4 (see Fig. 3.3). In these early observations, targets with promising chances to detect TeV γ-ray sources have been observed, so that the field of view of these early observations typically contain γ-ray sources and there is only a marginal amount of available background data. Therefore, the dependency on R/R_{est} is corrected by rescaling the exposure ratio α_A (Eqn. 4.9).

γ-Ray Exposure

Assuming that the differential γ-ray photon spectrum follows a power law (Eqn. 5.16) with an index of $\gamma = 1.7$ and a normalization $N_0 = 4.0 \cdot 10^{-12}$ cm^{-2} s^{-1} TeV^{-1} deg^{-2}, the γ-ray exposure can be calculated for the 131 observation runs with Eqn. 5.21. In Figure 6.1(b) the exposure is presented. The index and the normalization are taken from the spectral analysis of the of the complete Vela X region which will be discussed in Section 6.3.3. The normalization factor cancels out when the final flux map is calculated, but nevertheless a good estimate of n yields a realistic number of expected γ-ray events. The mean exposure within the circle indicating the extension of Vela X is $\sim$2600 events per deg^2. That is, multiplied by the area of this region, $\sim 10^4$ excess counts are expected. As the flux in the

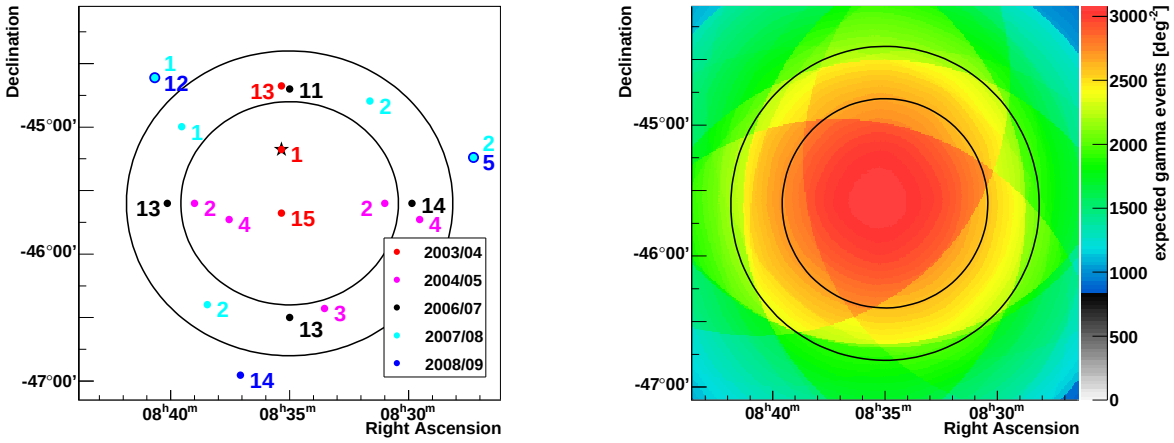

(a) pointing positions of the H.E.S.S. array

(b) exposure map

Figure 6.1: a) The map shows the pointing positions of the observation runs on VelaX. The numbers count the runs taken at the respective observation position. The position of the pulsar is indicated with the black star. The black circles with the radii 0.8° and 1.2° are centered on the TeV flux centroid. b) The γ-ray exposure is determined as the number of expected events for an assumed γ-ray flux.

ring extension is smaller than in the inner region, the number of measured excess counts will be smaller than the estimated exposure in the ring.

Background Run Selection

For the OnOff background model, the background runs are selected using the selection algorithm discussed in Section 4.1.2. Two weighting parameters are used to compensate the dependencies of the background in the zenith angle and the optical efficiency (Tab. 4.3). It is assumed that the dependencies on azimuth angle, number of broken pixels and camera temperature can be neglected by averaging over all pairs of On target and background runs. All background runs fulfill the run quality selection criteria (broken pixels, atmosphere and clouds). To obtain the smallest possible background exposure ratio α_A only background runs with an observation time of 28 min are considered, even if the associated On target runs do not reach the full 28 min of a standard observation run. Thus, the deadtime-corrected observation duration of the On target runs $t_t = 55.39$ h differs slightly from the observation duration of the background runs $t_b = 56.83$ h.

A Lower Energy Threshold

As mentioned already in the previous discussion, a cut on the lower energy is required when the OnOff background model is applied. The threshold should avoid that small deviations in the background rates between On and Off target data propagate to the number of excess

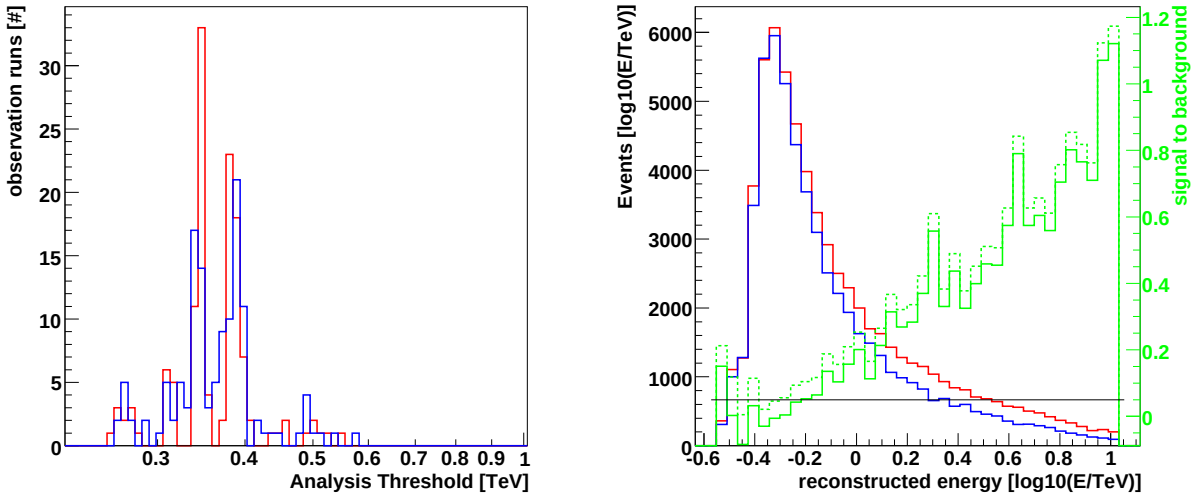

(a) analysis threshold

(b) signal-to-background ratio

Figure 6.2: a) Analysis thresholds for the 131 selected Vela X observations (red) and the associated background runs (blue). b) The event rates are given as a function of energy for the inner test regions in the on target and background runs. The signal-to-background ratio is drawn as green lines – the broken line without an atmospheric correction, the continuous line using the R/R_{est} correction. The black line indicates the 5 % level for the signal-to-background ratio.

counts (Eqn. 4.1) and the flux estimate (Eqn. 5.10). The OnOff model is susceptible to this fluctuation as the background data are observed under different atmospheric conditions and the signal-to-background ratio is relatively small for largely extended γ-ray sources. In the extraction of flux spectra, the threshold will be determined for each run pair. For the generation of flux maps the same threshold is applied for the complete data set (see Sec. 5.2). The classical approach for a lower energy threshold is the analysis threshold t_a, which has been defined as lowest energy where the energy reconstruction bias is smaller than 10 %. Another threshold proposed before is the peak energy of the background rates t_b. For the set of standard event-selection cuts (Eqn. 3.28 and 3.29) which is exclusively used in this Chapter t_b is always smaller than t_a (see Tab. 3.3). The distribution of the analysis threshold is shown in Figure 6.2(a) for the Vela X runs in red and for the associated background runs in blue. A choice of threshold larger than 600 GeV is implied by the distribution.

A second criterion for the threshold is the signal-to-background ratio. In Figure 6.2(b) the events extracted for the inner test region of Vela X are drawn as red line and the events extracted from the corresponding regions in the background runs as blue line. The green lines give the signal-to-background ratio, where the broken line is calculated without any correction on the atmospheric fluctuations and the continuous line makes use of the R/R_{est} correction (Eqn. 4.9). The energy where the signal-to-background ratio falls below 5 % is in the order of 750 GeV. Thus, a lower energy threshold at 750 GeV will be applied in the

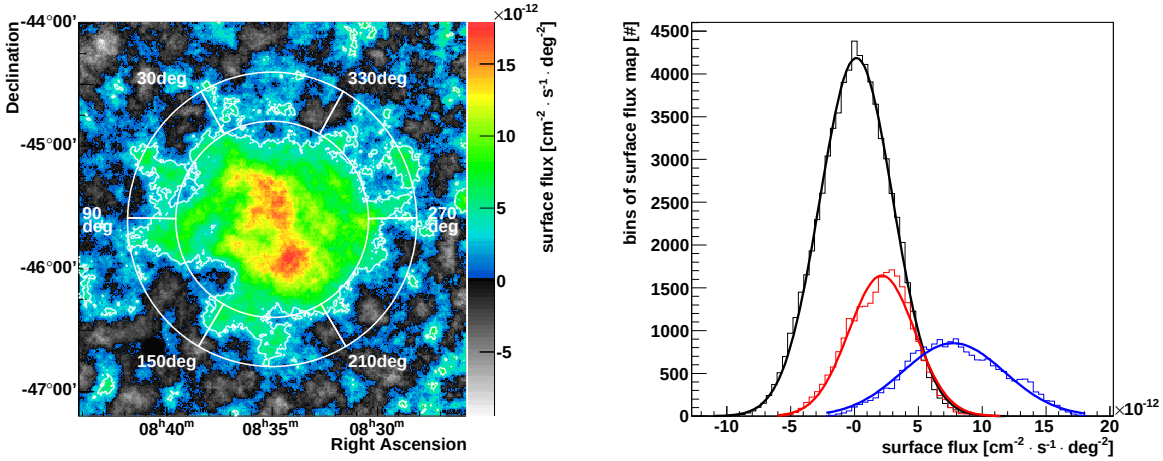

(a) Vela X - surface flux map

(b) surface flux bin distribution

Figure 6.3: a) The surface flux around Vela X is given here as a correlated sky map. A power-law spectrum with an index of 1.7 has been assumed to calculate the γ-ray photon flux. The inner region of the TeV flux from Vela X and the ring extension are drawn as white circles. The region of bins exceeding a significance of 2σ within the oversampling radius $r_o = 0.12°$ is surrounded by a white contour line. b) The surface flux distribution in the bins of the map is shown for the inner region (blue), the ring extension (red) and a region between 1.6° and 2.5° around the TeV centroid which is supposed to be a TeV γ-ray darkfield.

following for the flux estimates in sky maps and profiles.

6.2 Emission from the Ring Extension

The H.E.S.S. publication in 2006 [6] claimed a TeV γ-ray excess within an integration radius of 0.8°. Therein, an excess sky map[2] is included with the comment that the uncorrected differences in the exposure cause an underestimate of the actual flux of 10 % at the edge of the integration region. Here, it will be shown that there is also emission beyond this inner region.

A first hint as to an extended emission can be seen in Figure 6.3(a), where a flux map of the γ-ray flux above 750 GeV is presented. Each bin contains the flux estimate within an oversampling radius of $r_o = 0.12°$. The spectral shape was assumed to follow a power law with an index of 1.7 ($\mathrm{d}N/\mathrm{dE}$ in Eqn. 5.21 and 5.23). A significant argument for the extended emission can be given by counting the γ-ray events and comparing them with the background model. There are 21593 events in the On target runs and 19522 events in the background runs (only taking into account the runs until 2007/08 that are not dedicated

[2]The excess in each bin of an excess map is derived using Formula 4.1. Excess maps neglect gradients in γ-ray exposure over the field of view of the map. Smoothing and choice of the color scale are applied in the some way as describen for flux maps in Section 5.3

Table 6.2: The numbers of On target events N_t and background events N_b are given for the inner test region and ring extension. The background events for the runs pointing to the three positions (NE, NW, S) that allow to use the reflected background method are estimated from the reflected background. The background estimation for the remaining runs uses the OnOff method. The significance for γ-rays was calculated using the formula of Li and Ma (Eqn. 5.2). A lower energy cut at 750 GeV is applied.

region	N_t	N_b	α_A	σ	$\alpha_A \cdot \alpha_{RRE}$	σ_{RRE}
ring refl. NE	1631	1394	1	5.9		
ring refl. NW	764	686	1	2.0		
ring refl. S	1572	1519	1	1.0		
ring refl. sum	3967	3599	1	4.2		
ring OnOff	21593	19522	0.9787	12.4	1.0389	6.3
inner region refl. NE	2118	1474	1	10.8		
inner region refl. NW	983	740	1	5.9		
inner region refl. S	2142	1667	1	7.7		
inner region refl. sum	5243	3881	1	14.3		
inner region OnOff	22972	16976	0.9787	32.2	1.0383	26.3

to the reflected background model). Assuming an exposure ratio of $\alpha_A = 0.9787$ which is the ratio of the deadtime-corrected observation durations, a significance (Eqn. 5.2) of 12.4 is reached. Applying the R/R_{est} correction (Eqn. 4.9) for each run pair, the total exposure ratio is 1.0389 so that the significance yields $\sigma^{cor}_{OnOff} = 6.3$. When the reflected background model is applied to the dedicated data set, the ring contains 3967 and the reflected regions 3599 events, which results in a significance of $\sigma_{rfl} = 4.2$. These event statistics are summarized in Table 6.2.

The detection achieved with the two background models and independent data sets can be compared regarding the significances. Under the common assumption that the TeV γ-ray flux from pulsar wind nebulae is stable within the lifetime cycle of IACTs the significance should increase with the square-root of the exposure. A coarse estimate of the exposure ratio of the 2008/09 dedicated-reflected data set can be derived from Table 6.1. The ratio of the observation durations is 1:3 and the significance for the dedicated-reflected background data extrapolated to the exposure of the OnOff data set is $\sqrt{3}\cdot\sigma_{rfl} = 7.2$, which is in agreement with the OnOff significance using the R/R_{est} corrected OnOff background. The uncorrected OnOff background would imply a much higher significance. The same agreement can be found for the inner test region, so that the R/R_{est} correction is confirmed by the independent reflected background data.

The radial profile of the surface flux is given in Figure 6.4(a). It has been extracted from count and exposure maps (without an additional oversampling), where the surface flux was integrated over concentric rings around the center of the inner test region and the ring extension. The profile shows that the TeV signal in the ring extension belongs to the same source as the signal from the inner region distributed around the central position.

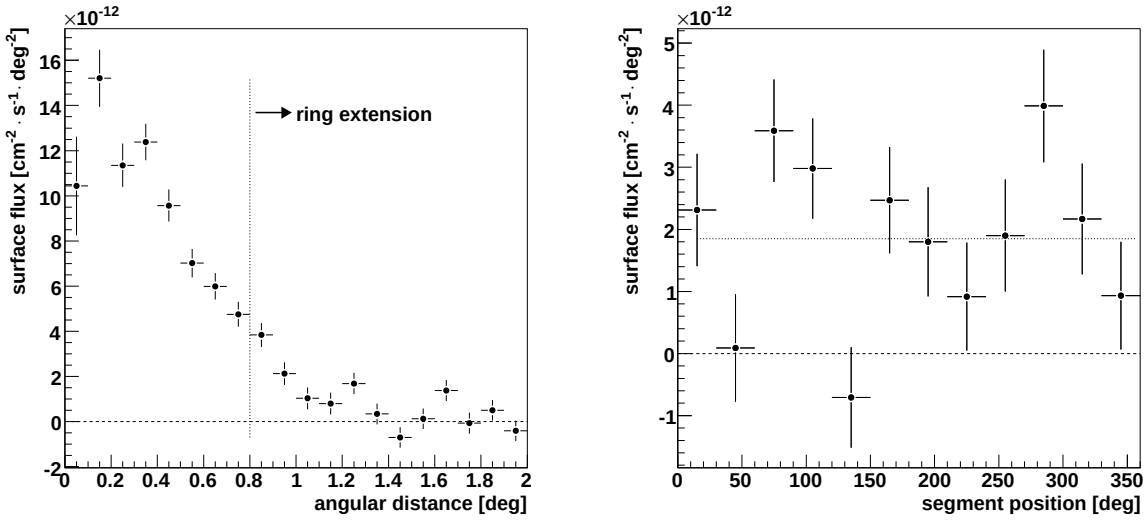

(a) radial profile

(b) azimuthal profile

Figure 6.4: a) The radial surface flux profile has been extracted from concentric rings around the flux centroid. b) The azimuthal profile displays the surface flux in the segments of the ring extension region. The opening angle of each segment is 30°. The horizontal line at $(1.8 \pm 0.3) \cdot 10^{-12}$ cm^{-2} s^{-1} deg^{-2} indicates the fit result for a constant to the azimuthal profile. In both plots, the surface flux is given for γ-rays with a reconstructed energy above 750 GeV.

The signal stretches out to a radius of at least 1.2°. Beyond 1.3°, the data points settle around the zero flux baseline with relatively high fluctuations compared to the estimated error.

Regarding the ring extension in the flux map (Fig. 6.3(a)), there seem to be bright regions within the ring which implies a substructure of the flux distribution of the extension. For a more detailed investigation the ring is split up into 12 segments. The angle defining the position of the segment starts in the north and its orientation is anti-clockwise (see the labels in the sky map). The flux is calculated in each segment using Eqns. 5.20 through 5.24 and is presented in Figure 6.4(b). Using a χ^2 minimization, a constant fit to the data points yields a flux level of $(1.8 \pm 0.3) \cdot 10^{-12}$ cm^{-2} s^{-1} deg^{-2} with a χ^2/dof of 29.2/11. Two of the segments exceed this flux level by more than twice the error estimate, while the flux in two further segments goes below the zero level by the same order. Anyhow in the following, it will be assumed that the flux is contributed homogeneously inside the ring.

The flux map in Figure 6.3 allows the extraction of the flux level for the test region. In the right panel, the flux distributions over the bins of the map are shown. The bins within the inner extraction region (< 0.8 deg around the TeV centroid) are shown in blue, the flux within the ring extension (between the radii 0.8 deg and 1.2 deg around the centroid) in red. The content of the bins is still correlated within the oversampling radius, so that the structure included in the test regions is smoothed almost to Gaussian shape. The mean

surface flux (total flux[3]) above 750 GeV of the inner region is $8.0 \cdot 10^{-12}$ cm^{-2} s^{-1} deg^{-2} ($16.0 \cdot 10^{-12}$ cm^{-2} s^{-1}) and for the extension $2.0 \cdot 10^{-12}$ cm^{-2} s^{-1} deg^{-2} ($5.0 \cdot 10^{-12}$ cm^{-2} s^{-1}). In Table 6.3, the integrated flux above 1 TeV is listed. With the index of 1.7 assumed for the flux map, 20 % of the flux originate from photons between 750 GeV and 1 TeV.

The third flux distribution drawn in Figure 6.3(b) in black has been extracted from the ring with radii 1.6 deg to 2.5 deg around the TeV centroid. Parts of the ring, where it crosses the position of the SNR Vela Junior (Fig. 1.2) and where the γ-ray exposure falls below 20 % of the exposure reached at the centroid, are rejected from the distribution. The ring can be used as darkfield region within the field of view of the Vela X observation runs. However, the flux in this darkfield ring is measured at higher offset angles ψ (incoming direction of the primary particle to the observation direction). The darkfield ring includes 47232 events in the foreground and 48441 events in the background runs, while the surface flux is $0.04 \cdot 10^{-12}$ cm^{-2} s^{-1} deg^{-2}. Using the R/R_{est} correction, a systematic uncertainty of the background estimation of 5 % remains (Sec. 4.4). In contrast to the event statistics for the ring extension (Tab. 6.2), no comparison with a reflected background model is available. The corresponding significance with an R/R_{est} corrected exposure ration of 0.9589 is 2.8. With a signal-to-background ratio of 0.016, the flux estimate is compatible with zero TeV flux from this region. The uncorrected exposure ratio $\alpha_A = 0.9146$ will yield a high deviation from the darkfield with a significance of 9.9 and a signal-to-background ratio of 0.060, that is a further affirmation for the R/R_{est} correction by the corrected darkfield.

6.3 The Differential Photon Spectrum of Vela X

In this Section, the differential γ-ray photon spectrum of Vela X will be presented. The spectral shape is an important way to investigate the processes which generate the γ-rays at their birth region in the PWN. At first, the spectrum will be extracted separately from the inner integration region and the ring extension. The inner integration region can be compared directly to the published spectrum. It will be shown that both spectra possess a consistent spectral shape. At the end, the extraction region for a joined spectrum will be extended up to a radius of 1.2° around the flux centroid. The algorithm to derive the spectra is describen in Section 5.2. The spectra are corrected using the R/R_{est} ratio (Eqn. 4.9). As this is a new approach for correcting atmospheric fluctuations in spectra extracted from H.E.S.S. data, the spectra will be also given in the classical approach where the exposure ratio is given only by the ratio of deadtime-corrected observation duration between On target runs and background runs. The results obtained with the different approaches are listed in Table 6.3.

[3]The size of the inner test region is 2.01 deg^2 and the size of the ring extension is 2.51 deg^2.

Table 6.3: The spectral characteristics either as parameters of a power law with exponential cutoff or as integrated flux (the last column) are listed for different analysis constraints. The upper sector of the table shows the flux which is derived from the inner test region (0.8° around centroid). The ring extension (between radii 0.8° and 1.2°) is the extraction region of the middle sector. At the bottom, the flux is estimated for the complete TeV Vela X (< 1.2°). The integrated flux from CANGAROO-I above a lower bound of 4 TeV is extrapolated for a lower bound of 1 TeV.

method		Norm [10^{-12} cm^{-2} s^{-1} TeV^{-1}]	Index	Cutoff [TeV]	Flux > 1 TeV [10^{-12} cm^{-2} s^{-1}]
HESS 2006	[6]		1.45 ± 0.09	13.8 ± 2.3	12.8 ± 1.7
Cangaroo	[105]				10.6 ± 3.0
Xeff	[42]	12.3 ± 0.7	1.42 ± 0.06	15.3 ± 2.0	16.3 ± 1.5
R/R_{est} cor.	Fig. 6.5(a)	9.6 ± 0.6	1.32 ± 0.09	11.2 ± 1.1	12.8 ± 1.2
classical	Fig. 6.5(a)	13.0 ± 0.6	1.51 ± 0.05	13.4 ± 1.4	15.2 ± 1.1
flux maps	Sec. 6.2				13.1
Xeff	[42]	3.9 ± 0.8	1.42 ± 0.22	13.2 ± 5.3	5.0 ± 1.5
R/R_{est} cor.	Fig. 6.6(a)	2.9 ± 0.7	1.30 ± 0.22	14.1 ± 5.4	4.3 ± 1.2
classical	Fig. 6.6(a)	5.6 ± 0.6	1.55 ± 0.13	16.2 ± 5.0	6.7 ± 1.2
flux maps	Sec. 6.2				4.1
Xeff	[42]	15.5 ± 1.0	1.39 ± 0.06	15.4 ± 2.0	21.4 ± 2.1
R/R_{est} cor.	Fig. 6.7	13.3 ± 0.9	1.33 ± 0.07	12.0 ± 1.4	18.0 ± 2.0
classical	Fig. 6.7	19.5 ± 0.9	1.53 ± 0.05	14.4 ± 1.5	22.7 ± 1.6

6.3.1 Differential Spectrum of the Inner Region

The differential photon spectrum of the inner test region is shown in Figure 6.5(a). The spectral points are calculated using Eqn. 5.10, so that the points give the rate of γ-ray events within equidistant bins normalized by the effective detection area and the observation time. An exponential cutoff power law is used to fit the spectral points. The spectral shape is well described with an index of 1.32 ± 0.06 and a cutoff energy of (11.2 ± 1.4) TeV (Eqn. 5.17). The total γ-ray flux above 1 TeV is $(12.8 \pm 1.2) \cdot 10^{-12}$ cm^{-2} s^{-1}, the χ^2/dof is 18.0/13. The spectral points for the classical approach are drawn in red. The parameters of the fitted exponential cutoff power law are an index of 1.51 ± 0.05 and a cutoff energy of (13.42 ± 1.39) TeV. The total γ-ray flux above 1 TeV is $(15.2 \pm 1.1) \cdot 10^{-12}$ cm^{-2} s^{-1}, the χ^2/dof is 16.8/13.

A first view on the two spectra bares that the R/R_{est} correction affects only the spectrum in the lower energy range, where the signal-to-background ratio is relatively small. For a comparison of both fits with the results reported by the H.E.S.S. collaboration in 2006, confidence levels are derived by scanning the parameter space[4], whereas the method is described in [67]. The confidence levels for each combination of the three fit parameters are shown in Figure 6.5(b) to 6.5(d). A blue marker indicates the 2006 results. The

[4]The implementation TMiniut::Contour within the ROOT toolkit (version 5.16/00) was used.

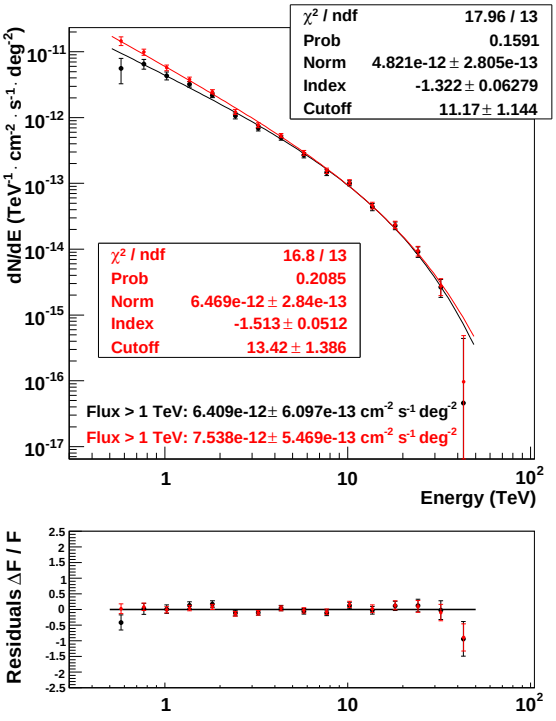

(a) differential photon spectrum

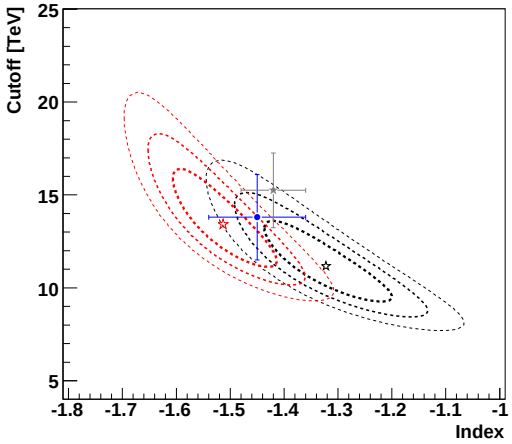

(b) confidence levels in index and cutoff

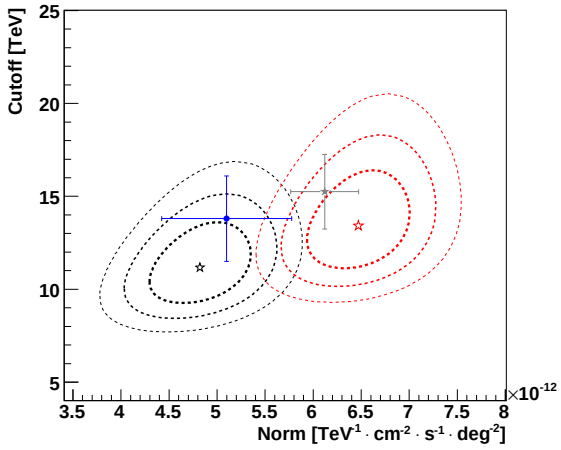

(c) confidence levels in norm and cutoff

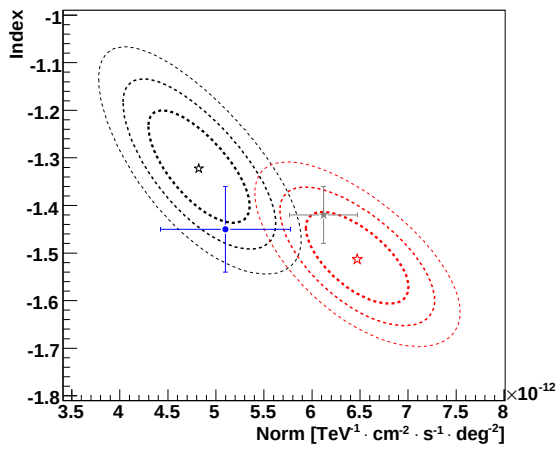

(d) confidence levels in norm and index

Figure 6.5: a) The differential photon spectrum is extracted from the inner test region of Vela X. The photon flux points in black are calculated using the correction on the R/R_{est} ratio, the red points using the classical approach for the exposure ratio. The lower part of the plot shows the relative residuals of the spectral points to the fit result. b-d) The plots show the confidence level at 1σ, 2σ and 3σ each for two of the three fit parameters. The blue points and error crosses represent the reported 2006 spectrum by the H.E.S.S. collaboration [6] and the gray stars gives the results obtained with Xeff selection cuts [42].

blue error bars (as well as the parameter errors in Fig. 6.5(a)) give the distance to the 1σ-confidence level in vertical and horizontal direction. The 2006 results are based on only about a fourth of the total amount of observational data. Furthermore, the so-called hard cuts [7] were employed (including a size cut of $s > 200$ pe) which reject more than a factor of 2 of the γ-ray events and of the background events compared to the standard cuts defined in Eqn. 3.28 and 3.29. Arguing in a non-strict manner, one can claim this result to be statistically independent. The surprising result is that the 2006 fit is consistent within one standard deviation with the R/R_{est} corrected spectrum. However, in the 2006 publication, the discussion of the atmosphere was restricted to the statement that a systematic error of 30 % is expected on the flux normalization, due to uncertainties in the transparency of the atmosphere to Cherenkov light [7]. The run list used for the 2006 analysis was available and if one assumes that the dependency of the post-selected events on the R/R_{est} ratio (Fig. 4.10) behaves in the some way for hard cuts (2006) and standard cuts (this work), an underestimation of the background rate of 10 % to 20 % are expected for the 2006 background run selection. A reason that the underestimation of the background rate is not forwarded to the flux estimate as strong as seen for the standard cuts is that for the signal-to-background ratio is larger.

An independent analysis on the Vela X data set was reported using a more efficient set of event-selection cuts (Xeff) for the separation of γ-ray events from the hadronic background. In the confidence level plots for the fit of an exponential cutoff power law to the γ-ray flux of the inner test region, the Xeff results are drawn as gray stars. The Xeff analysis does not make use of a correction method for atmospheric conditions, so that is not unexpected that the Xeff results are comparable to the uncorrected spectrum (red contours) in the normalization (Fig. 6.5(c) and 6.5(d)). For the flux shape defined by index and cutoff, the Xeff shape is quite similar to spectral fits of the "Hillas Analysis" (this work and H.E.S.S. collaboration 2006), although a minor systematic shift can be seen in the confidence level plot (Fig. 6.5(b)).

A statistical comparison between the R/R_{est} corrected spectrum and the uncorrected spectrum is not possible, as the spectral flux points are based on the same random experiment. Below in Section 6.3.3, a systematic comparison between the R/R_{est} correction spectral shape and the uncorrected one will be presented using a spectrum from the larger test region covering the entire nebula. A discussion of the systematic of the derived spectral shapes is given below (Sec. 6.3.5).

6.3.2 Differential Spectrum of the Ring Extension

We have seen before that a significant γ-ray flux is detected from the ring extension. The flux is strong enough to extract a separate differential photon spectrum from this test region. Again a power law with an exponential cutoff is sufficient to describe the spectral shape. The concluding interpretation regarding the spectral flux shape in the ring extension will additionally make use of the assumption that the a shocked pulsar wind accumulated

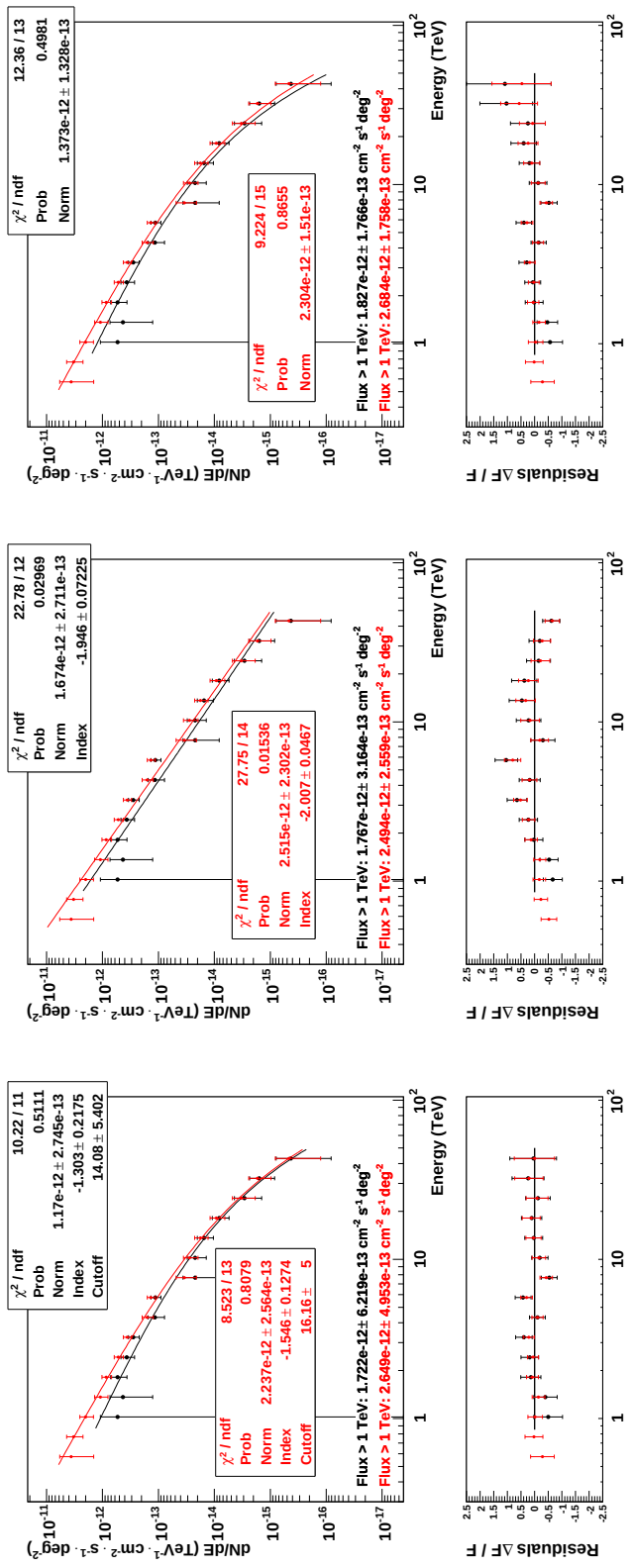

(a) power law with exponential cutoff (b) power law (c) power law with fixed exponential cutoff

Figure 6.6: The differential photon spectrum extracted from the ring extension of Vela X. The flux points in black are calculated using the correction via the R/R_{est} ratio, the red points using the classical approach for the exposure ratio. Relative residuals of the spectral points to the fit result are shown in the lower part of each plot. Different fit functions were used for the three plots: a) a power law with exponential cutoff (Eqn. 5.17), b) a pure power law (Eqn. 5.16) and c) a power law with exponential cutoff where the cutoff and index are fixed to 11.17 TeV, 1.322 for the R/R_{est} fit and 13.42 TeV, 1.513 for the classical approach.

in the nebula bubble is the source of the highly energetic particle plasma that generates the γ-rays. Assuming that the strength and spectral shape of the plasma outflow from the pulsar does not vary too much, the differences in the spectral shape of the ring extension which is further away from the pulsar to the inner test region would be destined by different cooling times, e.g. by synchrotron radiation. Another effect is that the particles with the highest energies exhibits a larger gyro radius, so that they are bound less by a magnetic field and escape faster from the nebula than the low-energy particles. So that, a softer spectral shape in comparison to the inner region is expected for the ring extension.

The spectral flux points from the ring extension are presented in Figure 6.6. The flux points in black are again corrected for atmospheric influences with the R/R_{est} ratio, while the red points show the uncorrected flux estimates. Three different fits were applied to these flux points:

- The first fit is a power law with an exponential cutoff (Eqn. 5.17) which was already used to describe the spectral shape of the inner test region. The three parameters (normalization, index and cutoff energy) are determined as free parameters in the fit. With a χ^2/dof of 10.2/11 the fit (Fig. 6.6(a)) of the R/R_{est} corrected flux points describes the spectral shape very well. It yields an index of 1.30 ± 0.22, a cutoff energy of (14.1 ± 5.4) TeV and a normalization of (2.9 ± 0.7) cm^{-2} s^{-1} TeV^{-1}.

- To obtain an additional cross check for the existence of the cutoff, a pure power law is fitted to the flux points. A look at the spectrum (Fig. 6.6(b)) reveals that the pure power law is disfavored against the fit function including the cutoff. The χ^2/dof is 22.8/12, which is significantly worse than the $\chi^2/dof = 10.2/11$ for the fit with the exponential cutoff.

The remaining question concerning the ring spectrum is, whether a shift of the cutoff to lower energies and a softening of the spectral index can be verified:

- In order to investigate this question, a third fit – again a fit using a power law with cutoff – was performed, with the distinction that this time the cutoff energy and the spectral index were fixed to the corresponding values of the fit for the inner region (cutoff at 11.2 TeV and a spectral index of 1.32, respective 13.4 TeV and 1.51). The fit quality is comparable to the fit with the full set of three free parameters, so that the spectral shape in the ring extension is indistinguishable from the shape in the inner test region. The consistence of the spectral shape in the ring extension with that of the inner test region allows a very important conclusion: the PWN is filled up to the outer radius of 1.2° with the same highly energetic particle plasma and no softening of the TeV spectrum – as argued in the beginning of this Section – is seen up to 30 TeV.

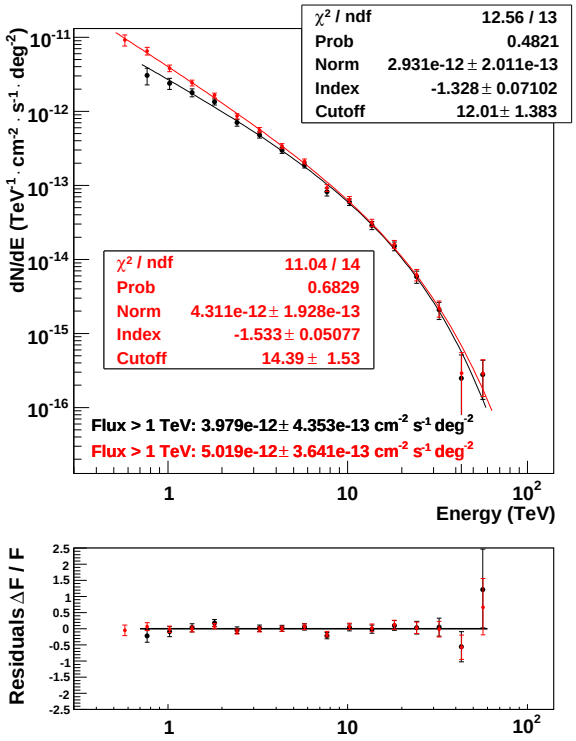

Figure 6.7: The differential photon spectrum is extracted from the entire Vela X (within a radius of 1.2°). An exponential cutoff power law was used to fit the spectra. For a detailed description see caption of Figure 6.5(a).

Table 6.4: The table shows the number of events extracted to the last two spectral bins of the Vela X entire test region N_t, the background model N_b and the resulting excess counts N_{ex}.

Energy Range	N_t	N_b	N_{ex}
37.5 TeV to 50.0 TeV	33	25	7.33
50.0 TeV to 66.7 TeV	16	7	8.86
66.7 TeV to 100 TeV	2	4	−2.08

6.3.3 Differential Spectrum of the Entire Vela X Nebula

As a consequence of the claim for the ring extension spectrum to be consistent with the spectrum of the inner region, the spectral shape of Vela X should be summarized in a combined test region within 1.2° around the flux centroid. In Figure 6.7 the differential spectrum is presented (black) for the full Vela X nebula. The spectral points are again fitted with an exponential cutoff power law which yields an index of 1.33 ± 0.07 and a cutoff energy of (12.0 ± 1.4) TeV. The effective detection area in the sky is 4.52 deg^2 and the total flux above 1 TeV from Vela X is $(18.0 \pm 2.0) \cdot 10^{-12}$ cm^{-2} s^{-1}.

A High Energy Component

The shown data points impress an interesting feature. the penultimate bin (37.5 TeV to 50.0 TeV) goes below the cutoff power law, while the ultimate bin (50.0 TeV to 66.7 TeV)

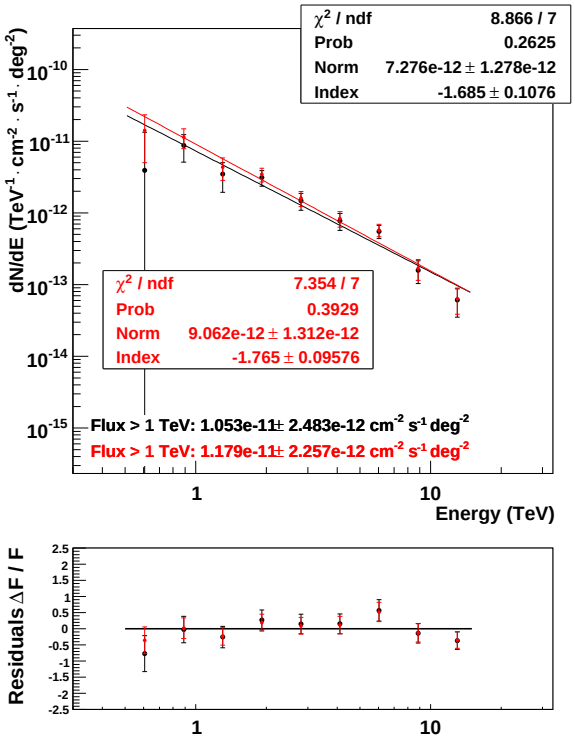

Figure 6.8: The differential photon spectrum is extracted from a test region with a radius of 0.2° around the pulsar. A pure power law is fitted to the flux points. For a detailed description see caption of Figure 6.5(a).

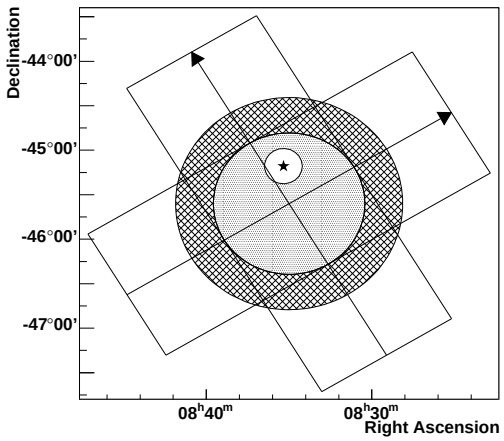

Figure 6.9: The map is a schematic overview of the region around Vela X. The star marks the pulsar PSR B0833-45. The white region with a radius of 0.2° around the pulsar is the test region for the spectrum of the pulsar's nearest surroundings. The dotted area indicates the region 0.8° around the center of the TeV emission. The ring extension is the surrounding cross-hatched ring with an outer radius of 1.2°. The two boxes are used to extract flux profiles with the arrows defining the direction of the profiles.

exceeds the model each by half of the length of the 68.3 % confidence interval indicated by the error bars. A similar behavior was found for the inner test region in the 2006 publication (Fig. 3 in [7]). One should note, that the effect in both cases is not significant and it will be hard to prove it with the sensitivity of the recent IACTs. However, a step in the highest bins is of general interest, as such a flux is not included by the leptonic model introduced before (Sec. 1.3.3) and it would imply an additional PWN component (e.g. a hadronic one or young, recently accelerated leptons). In Table 6.4, the number of events within the test region of the On target data N_t and the number of events in the background data N_b are given for the penultimate bin, the ultimate and for the energy range between 66.7 TeV and 100 TeV. The number of excess counts N_{ex} is derive with Eqn. 4.1. For the energy range beyond 66.7 TeV, no further flux is seen.

6.3.4 The Nearest Surroundings of the Pulsar

There are two questions concerning the γ-ray emission from the direction of the Vela Pulsar (PSR B0833-45). The first one, is it possible to detect TeV γ-ray events from the pulsar

with H.E.S.S., especially is there a detectable pulsed emission? In 2006 the 99.9 % upper limit on the integrated flux from the pulsar above 1 TeV was given as $0.76 \cdot 10^{-12}$ cm^{-2} s^{-1}. The limit was derived within a radius of 0.1° and the corresponding surface flux for the limit is $23.9 \cdot 10^{-15}$ cm^{-2} s^{-1} deg^{-2}. Until now, H.E.S.S. has not detected any further PWN that allows to associate TeV γ-emission with a the central pulsar. A search for pulsed emission with H.E.S.S. is described in [9]. For the Vela Pulsar no pulsed emission above a threshold of 250 GeV has been found. The recent common interpretation is that the spectral energy distribution of the pulsed emission breaks below the energy threshold of the H.E.S.S. telescopes. This hypothesis is supported by the measurement of pulsed emission from the Crab pulsar (PSR B0531+21) with the MAGIC telescope. The hardware trigger of the telescope has been optimized to allow the detection of γ-ray events with a lower energy threshold of 25 GeV. A combination with the results of the satellite-borne γ-ray detectors EGRET (∼1 to 30 MeV) and COMPTEL (∼30 MeV to 10 GeV) [76] yields for the pulsed emission from the Crab a cutoff energy of $17.7 \pm 2.8_{stat} \pm 5.0_{syst}$ GeV in a fit to a power law with exponential cutoff. The H.E.S.S. telescopes will not reach such low energies and it is not expected that other pulsars exhibit pulsed emission up to higher energies.

It was shown that the spectral index of $3 - 10$ keV X-rays is softening ("quite mild") from an index of 1.60 to 1.90 (respectively from 1.50 to 1.66 in a second choice of test regions) near the pulsar against the surrounding regions [86]. X-rays synchrotron and TeV IC emission follows the same power law with an index of $(\alpha + 1)/2$ (Eqn. 1.14), where α is the index of the lepton injected by the termination shock (Eqn. 1.14). This motivates the second question, can such a softening also be seen in the TeV signal? The example, where a similar spectral softening was obtained is the source HESS J1825-137. Within a distance of 0.2° (13.6 pc) a spectral power-law index smaller than 1.9 was found, whereas the index softens to 2.4 at a distance of 0.6° (40.8 pc) and keep almost constant up to the maximal extension of 1.2° (81.6 pc) [11].

In order to search for a comparable softening in the TeV data of Vela X, a spectrum was extracted from a small test region with a radius of 0.2° around the pulsar position. This choice of the radius is a compromise between decreasing exposure area with a smaller radius and an integration over already hardening emitting regions. As the change of the index in X-rays is already finalized within the test region, as the TeV flux is overlaid by flux from the PWN before and behind the pulsar and as it is not possible with the given H.E.S.S. data to separate index difference smaller than 0.1, one does not expect to prove the softening in TeV flux. Likewise, the existence of the energy cutoff cannot be determined within this test region. A power-law fit (shown in Fig. 6.8) in the energy range 0.5 – 15 TeV to the R/R_{est} corrected flux points yields a photon index of 1.68 ± 0.07 and an integrated flux above 1 TeV of $(10.5 \pm 2.5) \cdot 10^{-12}$ cm^{-2} s^{-1} deg^{-2}. Disregarding the energy cutoff of the PWN, the integrated flux above 1 TeV corresponds to about 8.5 % of the total TeV flux from Vela X. The spectrum extracted from the entire Vela X region is fitted with a pure power law in the restricted energy range from 0.5 to 15 TeV (not shown as plot). The obtained index of 1.64 ± 0.04 can now be compared to the index from the

Table 6.5: The left table was presented together with the analysis results of H.E.S.S. observations of the Crab nebula [7]. The right table are adapted for the Vela analysis based on the OnOff background model (see text). Note, that the Data variability in the left table is the variance in the flux for an individual run to the other runs of the Crab data set. In the right table the variance of the complete data set is given. The errors given for the OnOff background correspond to the inner test region. Note that the estimate for the index within OnOff has been read out from the spectral fits and cannot be used to rank he same. The given total uncertainty is the quadratic sum of the listed contributions.

(a) H.E.S.S. publication on the Crab, 2006

Uncertainty	Flux	Index
MC Shower interactions	1 %	
MC Atmospheric sim.	10 %	
Broken pixels	5 %	
Obs. Duration	1 %	
Selection cuts	8 %	0.08
Background est.	1 %	0.01
Data variability	15 %	0.05
Total	20 %	0.09

(b) this work, OnOff, Vela X

Uncertainty	Flux	Index
MC Shower interactions	1 %	
MC Atmospheric sim.	10 %	
Broken pixels	5 %	
Obs. Duration	1 %	
Selection cuts	8 %	0.08
Background est.	15 %	0.1
Data variability	1 %	0.03
Total	25 %	0.13

pulsar test region. As expected, both power laws are comparable, so that no variation of the spectrum can be established.

6.3.5 Systematic Influence on the Extracted Spectra

The H.E.S.S. collaboration has compiled a detailed list of contributions to the systematic error on the flux estimate and the spectral power-law index which can be found in Section 7.3 of Reference [7]. The event reconstruction, γ / hadron separation and evaluation of flux spectra used by the authors is comparable to the analysis describen in Chapter 3 of this work. The major difference is the applied background model, with the original error estimation being based on a background model in the same field of view (in particular the reflected background and the so-called ring background). Here, by contrast, the estimation of the systematic error will be discussed in detail and adapted for the OnOff background model. For simplification, only a the index is regarded, neglecting the cutoff. Anyhow the influence of the R/R_{est} correction is as largest at the low energies with no significance influence on the cutoff. Table 6.5 shows the original and the adapted listing. The main contributions stem from:

Background model In Section 4.4, a systematic misestimate for the number of background events after correcting for the influence of atmospheric fluctuations is estimated to amounted to $\Delta_{Bg} \sim$5 %. That is, these 5 % of all background events will go

into the γ-ray flux determination, so that the propagated systematic error depends on the signal-to-background ratio. The signal-to-background ratio for the inner test region is $r_{sb} = 0.31$ (for the ring extension 0.07) and the resulting contribution to the error estimation of the flux normalization is $\Delta_{Bg} \cdot \frac{1}{r_{sb}} = 0.15$ (ring extension: $\Delta_{Bg} \cdot r_{sb} = 0.74$). The influence of the OnOff background model on the spectral shape becomes apparent in the spectra plots (e.g. Fig. 6.5(a)) between the R/R_{est} corrected and classical data points. From the plots, it can account for a change of the spectral index between 0.1 and 0.2. Unfortunately, this approach is not an independent estimation of the systematic error to compare the corrected with the uncorrected spectra.

MC and Observation Duration No basic changes are necessary regarding the error estimate related to the measurement of the observation duration or to the quality of the MC description of real air showers. However, there is a second measurement of a deadtime-corrected observation duration for each run pair in the OnOff background. The contribution from these second measurements is included in the error estimate attributed background model. The 10 % contribution from the atmospheric model in the MCs will cause a shift of the flux estimate to the complete data set. Minor fractions of this deviation cancel with the muon correction (< 600 m, see Sec. 3.1.3). In contrast to the run-by-run variability (see below), the MC systematics do not depend on the number of runs in the data set. For more details on the influences of atmospheric effects in MC see also [22].

Broken pixels An upper limit on the influence of the number of broken pixels on the flux can simply be estimated by considering that for each broken pixel the size of a shower image is reduced on average by a factor of $\frac{1}{960}$, as there are 960 pixels in the camera. For the Vela X data, there are on average 44 broken pixels, so that the approximation of 5 % is also valid here. A more complex determination of the effect of broken pixels was presented by S. Kopper [72].

Selection cuts The Crab data were analyzed with so-called "hard", "std" (Eqn. 3.28 and 3.29) and "loose" selection cuts [7]. A deviation of 8 % in the flux and 0.08 in the index between these three sets of cuts were found. The largest effect is already considered by the error estimation for the background model. If the selection cuts change also the signal-to-background ratio changes.

Data variability The Vela X analysis does not correct the γ-flux for atmospheric fluctuations[5]. In principle such a correction is possible, if the state of the atmosphere is connected to the energy reconstruction (e.g. see [93]) and does not depend on the background model. A run-by-run RMS of 15 % for the flux measured in the refereed Crab runs has been found. If the γ-ray rate is expected to behave like the background rate, the variation of the Vela data can be estimated using the R/R_{est} ratio. The

[5]Note that here the γ-flux is the issue of interest, not the background.

RMS on the ratio is 15 %. Since the R/R_{est} distribution for Vela X (Tab. 6.1) is situated above 1, so that the post-selected rate will be accounted with a factor of $\sim$0.5 (Eqn. 4.8). Additionally, the aim of the table is to appreciate the systematic error on the whole data, the RMS is divided by the square root of the number of runs (131). The Crab runs are divided into three sets and a variability in the spectral index of 0.05 was found, an index error of 0.03 is transfered to Vela.

In sum, the estimated relative systematic error for the inner test region is 25 % (and 28 % for the entire Vela region). For the ring extension, the relative error rises up to 70 %, although such a high systematic does not endanger the detection of flux in the ring extension. However using analysis frame works without a correction for the atmospheric conditions, large misestimations of the rings flux are expected. If one replaces the data variability by the contribution (2 %) which is expected for the 52 Crab runs the total uncertainty for the Crab analysis is 15 %. The larger uncertainty for the Vela analyses are caused by the OnOff background model.

6.4 The Morphological Structure of Vela X

Based on the result that the entire nebula show a homogeneous flux spectrum the spatial morphology will be determined in the following. Therefor two-dimensional fits on the flux sky map are performed. Broad flux profiles through the centroid will be used to measure the extension of Vela X and to be compared with X-rays and radio observations. Until now, the excess centroid at RA = $08^h35^m00^s$, Dec = $-45°36'00''$ (J2000) reported by the H.E.S.S. collaboration in 2006 was used to analyze the recent data. It will be shown that this position is still a good description for the center of the flux in the complete data set. Different methods will be applied to extract a centroid from TeV flux sky maps. A summary of the different approaches is given in Table 6.6.

6.4.1 Determination of the TeV Flux Centroid

The centroid is determined from a flux map with a bin width of 0.01°. No oversampling has been applied to this map and the flux was estimated using the R/R_{est} correction. The centroid is determined within a test region with a radius of 1.5°. In an interactive approach the center of the test region is chosen as the centroid determined in the previous step. Starting at the position II, the new centroid is found at RA = $08^h34^m56^s$, Dec = $-45°33'57''$ (J2000) which is 0.04° away from position II. To be independent from the choice of the starting position for the center of the test region, various starting positions were tested. All starting positions within 1.5° around position II converge in a consistent centroid. Moreover, if the radius of the test region is decreased down to 0.8°, the binning is broadened or the flux estimate is done without atmosphere corrections a flux centroid within $\sim$0.15° around position II is found.

Table 6.6: Different specifications for the position of the center position (right ascension, declination, J2000), the widths σ_1, σ_2 along the major axes and the angle α between the north and the major axis measured anticlockwise.

method		center position	distance Pos. II	σ_1 [deg]	σ_2 [deg]	α [deg]
position II	[6]	$08^h35^m00^s$, $-45°36'00''$				
2006 best fit center	[6]	$08^h35^m01^s$, $-45°34'40''$	0.02°	0.48 ± 0.03	0.36 ± 0.03	41 ± 7
centroid	Sec. 6.4.1	$08^h34^m56^s$, $-45°33'57''$	0.04°			
one-dimens. Gaussian fit	Sec. 6.4.2	$08^h35^m10^s$, $-45°31'39''$	0.08°	0.42 ± 0.01		
two-dimens. Gaussian fit	Sec. 6.4.2	$08^h34^m57^s$, $-45°36'49''$	0.02°	0.50 ± 0.02	0.34 ± 0.01	38.2 ± 3.1
flux profiles	Sec. 6.4.3			0.53 ± 0.03	0.54 ± 0.04 (σ_b)	30.0 ± 5 (fixed)

6.4.2 Elongated Two-Dimensional Gaussian Model

The most common model for the morphological structure of the TeV γ-ray flux of a source on the sky is a two-dimensional Gaussian function. Since the projection of a three-dimensional Gaussian is again a two-dimensional Gaussian, the model will be an approximation of the three-dimensional structure of the pulsar wind nebula. The Gaussian function will be used in the following notation:

$$g(\vec{x}) \;=\; n_0 \cdot \exp\left(-\frac{1}{2} \cdot (\vec{x}-\vec{c})^T D_\alpha^T \Sigma D_\alpha (\vec{x}-\vec{c})\right) \tag{6.1}$$

The position vectors $\vec{x}$ for the test position and $\vec{c}$ for the center of the Gaussian are derived as solid angle vectors of a spherical coordinate system parallel to the right ascension and declination. Before, the spherical coordinates were simplified by treating them as Cartesian coordinates. Differences in the fit results are negligible, if the Cartesian approximation is used. The 2×2 matrix Σ contains the principal component variances σ_1 and σ_2 along the major axis and semi-major axis of the flux distribution (as squared inverse $\frac{1}{\sigma_i^2}$), where the convention will be used that σ_1 is larger than σ_2. The rotation matrix D_α rotates the connection vector between $\vec{x}$ and the center by the angle α, where α measures the angle anticlockwise between the north (top of the map) and the major axis.

The Gaussian function (Eqn. 6.1) is fitted in a χ^2 minimization to the surface flux map of VelaX. A weighting of the sky map bins in the χ^2 minimization is derived from the systematic error on the flux estimate. Therefor the binning of the surface flux map is chosen to be 0.1° and no oversampling or any other additional smoothing were applied.

The fit is restricted to all bins included in the test region used to determine the spectrum of the full nebula (within a radius of 1.2° around the 2006 position II). The influence of the point spread function (see Fig. 3.11) on the fitted model is marginal and will be neglected.

The results for the full elongated Gaussian with six parameters are $\sigma_1 = (0.50 \pm 0.02)°$, $\sigma_2 = (0.34 \pm 0.01)°$ and angle of the major axis to the north is $\alpha = (38.2 \pm 3.1)°$. The normalization yields $n_0 = (14.5 \pm 0.6) \cdot 10^{-12}$ cm^{-2} s^{-1} deg^{-2} and the χ^2/dof is 658.2/426. The center position is RA = $08^h34^m57^s$, Dec = $-45°36'49''$ (J2000) with a radial statistical error of 0.02° and a displacement of 0.02° with respect to position II. The elongated Gaussian model should be interpreted with caution, as especially the width of the semi-major axis is influenced by TeV excess at the position of the X-ray feature. In Section 6.4.4, evidence in the TeV morphology for the feature which was observed in X-rays and radio observations is discussed. Along the semi-major axis, the elongated Gaussian model will find a width between a narrow component at the position of the feature and a broad component describing the size of the entire PWN.

A further simplification of the Gaussian model is a reduction to one width component by equaling $\sigma_1 = \sigma_2$. The remaining four fit parameters are the normalization constant n_0, the variance σ, right ascension and declination of the center $\vec{c}$. The resulting σ is $(0.42 \pm 0.01)°$ and the normalization is $n_0 = (11.5 \pm 0.6) \cdot 10^{-12}$ cm^{-2} s^{-1} deg^{-2} with a χ^2/dof of 810.5/428. The center position is found at RA = $08^h35^m10^s$, Dec = $-45°31'39''$ (J2000), where the radial statistical error is 0.03°. The displacement with respect to the 2006 position II is 0.08°.

6.4.3 Profiles of the TeV Flux

In previous parts of this work, the jet-like X-ray feature was discussed (Sec. 1.3.2). The flux map (Fig. 6.3(a)) gives a first hint to a TeV counterpart of the X-ray feature. For a more detailed investigation, profiles with a broad width were generated from a flux map. Here, the pure flux profiles are modeled with a Gaussian approximation. In the next paragraph, the profiles are compared to the ROSAT X-rays map (Fig. 1.3) and to radio observations.

The profiles in Figure 6.10 show the γ-ray flux of particles above 750 GeV. The profile in the left panel is extracted along the axis rotated through 30° anticlockwise from the north and through the flux centroid (position II). The width of the profile is 0.8° on each side of the axis, so that the main parts of the PWN are included in the profile. The location of the profile is charted to the overview sky-map in Figure 6.9. In the overview map, the arrow goes from −2.0° to +2.0° in the scale of the profiles. A Gaussian function is fitted to the data points in the range of the ring extension (±1.2°) and yields a width parameter of $\sigma_1 = (0.53 \pm 0.03)°$. This is in good agreement with the value for the width along the major axis from the two-dimensional elongated Gaussian fit. The center of the Gaussian is found at a position 0.07° away from the flux centroid.

In Figure 6.10(b), a second profile at 120° perpendicular to the first profile is shown. This profile is again fitted by a single Gaussian (red line in the figure) with a $\chi^2/dof =$

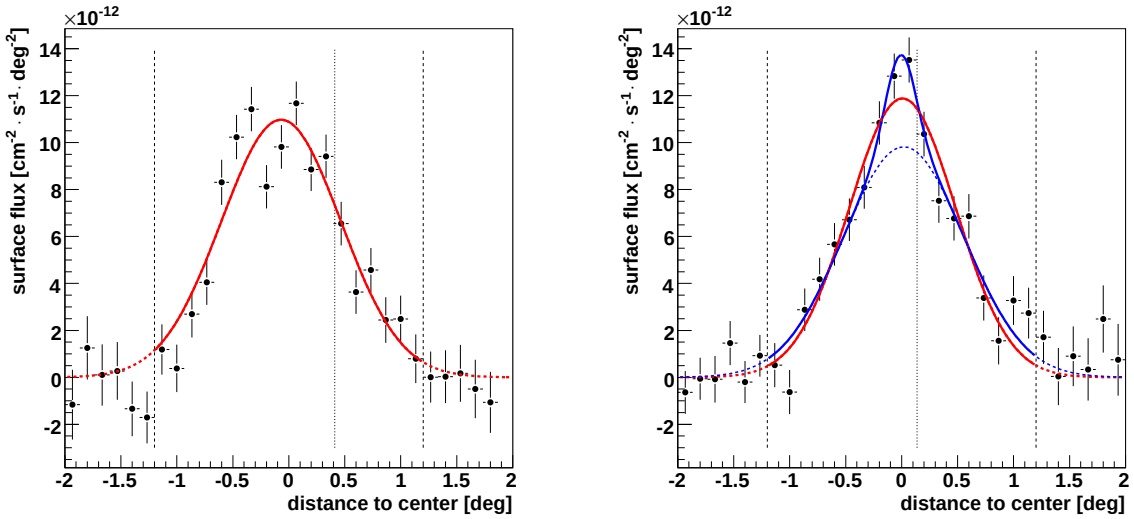

(a) profile axis at 30°

(b) profile axis at 120°

Figure 6.10: a+b) The flux profiles are extracted in ±0.8° wide slices along axes through the flux centroid with an orientation of 30° (respectively 120°) anticlockwise to the north. In both plots, the flux above 750 GeV has been derived assuming a power law with an index of 1.7. The horizontal broken line indicate the extension of the TeV PWN and the dotted lines indicates the projected position of the pulsar. Single Gaussian functions fitted to the profiles are drawn in red. b) Additionally the sum of a broad and a narrow Gaussian component is drawn as blue curve. The broken blue line shows only the broad component.

26.3/15, where the width results in $\sigma_2 = (0.48 \pm 0.02)°$. At the position of the feature – in the middle of the profile – two data points are raised against the remaining profile. A second fit (blue line in the Figure) composed of the sum of two Gaussian functions is applied, in which the sum describes the profile of Vela X by a broad component σ_b for the entire PWN and a narrow component σ_n for the feature. The fit yields $\sigma_b = (0.54 \pm 0.04)°$ and $\sigma_n = (0.13 \pm 0.04)°$ and the centers of both components are found at a distance perpendicular to the axis of the first profile $d_b = (0.02 \pm 0.03)°$ and $d_n = (-0.01 \pm 0.04)°$. With a $\chi^2/dof = 16.8/12$, the two-component model is slightly preferred against the single Gaussian fit. That is, the width of the broad component is comparable to the width of the first profile. The narrow component implies that the particle plasma producing the TeV emission is densified in some kind of a pipe in the middle of the PWN at the position of the X-ray feature. However, the counterpart cannot be clarified finally on the ground of the existing H.E.S.S. data set.

A critical point is the choice of the angle of 120° (respectively the perpendicular first profile at 30°) for the orientation of the profile axis. This angle has been chosen in the internal discussion of the Vela X results within the H.E.S.S. collaboration and might be biased by the fact that at this orientation the narrow component can best be seen. If the orientation angle is varied in a range between 115° and 125° the narrow component is still

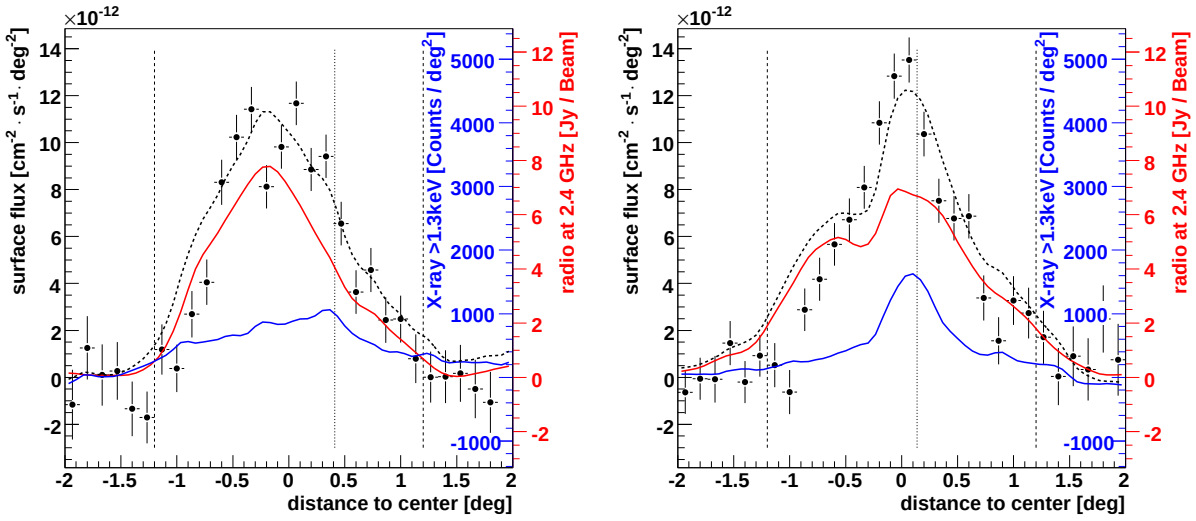

(a) axis at 30°

(b) axis at 120°

Figure 6.11: The plots show the same TeV flux profiles as in Figure 6.10. The profiles are compared to profiles from X-rays (above 1.3 keV) and radio (at 2.4 GHz) observations drawn as blue and red curves. A model for the TeV profile composed of the X-rays and radio curves is presented as broken black line.

found by the fit. For angles down to 110° and up to 130° the raise of the central data points is still observable, but the fit does not find the narrow component.

6.4.4 Comparison of the TeV Profiles with X-Rays and Radio

In the previous Section, flux profiles were used to determine the spatial extension of the TeV PWN. Here, a comparison of the profiles with a X-rays map $m_x(\vec{x})$ and a radio map $m_r(\vec{x})$ are presented. The favored leptonic model (Sec. 1.3.3) implies that the spatial morphology of the X-ray and TeV emission should match each other, as the emission is generated from the same leptonic plasma in synchrotron and Inverse Compton processes. This argumentation only works, as long as the magnetic field strength B is homogeneous throughout the emission region, such that the synchrotron flux is proportional to B^2. The radio signal is in principle independent of the X-ray / TeV morphology. Thus rather simple picture of a 1:1 relation between X-ray and TeV has already been broken as TeV emission is detected in the ring extension (Sec. 1.3.3).

The X-rays map m_x counting events above 1.3 keV has been obtained with the ROSAT satellite and was shown before in Figure 1.3(c). A background level of 400 X-rays counts per deg^2 is found in the region beyond Vela X (gray box in Fig. 1.3(b)) and is removed from the X-ray data. The origin of the X-rays background was not investigated further. Apart from contributions from so-called non X-ray background from the detector itself,

the X-rays emission in the gray box can be connected to the Vela SNR. The Vela Pulsar is a strong point-like source and is also removed from m_x. To simulate the wider PSF of H.E.S.S., the ROSAT data were smoothed with a Gaussian width of 0.07°. Two radio observations of VelaX were presented before in Figure 1.4(b). Here, the data from the galactic scan carried out with the Parkes telescope [45] will be used as radio map m_r. The Parkes telescope was operated at 2.4 GHz with a receiver band width of 145 MHz [44]. The half power beam width of the final radio map is 0.17°, which is slightly broader than the H.E.S.S. PSF. Apart from the strong signal around the central position of the PWN, the radio data include an additional feature in the eastern part of the ring extension. In Figure 6.11, profiles of the X-ray (blue) and the radio map (red) are presented, beside the already discussed TeV flux points (Fig. 6.10). The shape of the X-ray profile depicts the central narrow TeV component (seen in the 120° profile). Hence, the putative narrow component can be a counterpart of the X-ray feature. In the 30° profile along the X-ray feature, the X-ray emission forms a ramp outgoing from the pulsar to the south. This form is not found in the TeV profile. On the other hand, the radio profile reflects the shape of the 30° TeV profile. For the 120° profile, the situation looks a bit more complicated. The radio shape reflects the TeV flux points in the west of the pulsar ($> 0.2°$ in the profile). The eastern part of the radio profile is dominated by the additional excess mentioned before. Unfortunately, a description of a radio counterpart for the X-ray feature suffers from the larger PSF of the radio observation, so that a counterpart cannot by identified in the profile.

A simple model for the TeV flux is drawn as broken lines in Figure 6.11. The model S_m is a linear combination of the radio nebula $m_r(\vec{x})$ and the X-ray map $m_x(\vec{x})$. Due to the B^2 dependence of the synchrotron radiation, the model only works, if the magnetic field strength is constant. In contrast to the two component Gaussian fit discussed before, the two-dimensional model is independent of the choice for the profile orientation angle.

$$S_m(\vec{x}) \;=\; a \cdot m_x(\vec{x}) + b \cdot m_r(\vec{x}) \tag{6.2}$$

where a and b are the linear coefficients. S_m is fitted to the coarse-binned and non-oversampled surface flux map introduced in Section 6.4.2 with a χ^2 minimization. The region east of the line at a right ascension of $08^h37^m36^s$, where the additional radio feature occurs, is excluded from the two-dimensional fit. The resulting coefficients are $a = 1.16 \cdot 10^{-12}$ cm^{-2} s^{-1} deg^{-2} (Jy/Beam)$^{-1}$ and $b = 2.71 \cdot 10^{-15}$ cm^{-2} s^{-1} xcounts^{-1}.

As a result of the comparison with of the TeV data with X-ray and radio observations, three suggestions can be made. The TeV profile can be fitted with a two-component Gaussian function as alternative to a single Gaussian, in which the size and position of the additional component is consistent with X-ray feature. The first suggestion is that, if the narrow component exists[6], it is a counterpart of the X-ray feature. Second, the spatial

[6]If one consults the χ^2/dof of the single- and double-component fit to the 120° profile as an indicator for the required exposure on Vela X to verify the existence of the second component with a factor of $(\chi^2/dof)_{double}/(\chi^2/dof)_{single} = 3$, an observation time of ∼400 h with the H.E.S.S. telescopes is required.

distribution of the leptons producing the X-rays / TeV emission fills approximately the same volume as the lepton distribution generating the radio signal in the region beyond the X-ray feature. The third suggestion is that the magnetic field strength is not constant within the nebula. Regarding the slight falling edge of the 120° X-ray profile (Fig. 6.11(b), $-1.2°$ to $-0.2°$ and $0.4°$ to $1.2°$), a variation by a factor of $\sim$3 in the field strength (resulting in a factor of 10 in the flux ratio between X-rays and TeV γ-rays) can be inferred. However, this estimate is very coarse, especially the determination of the background level in the X-ray map ("gray box") can change the ratio between TeV and X-ray flux dramatically and therefore also the estimate for the variation of the magnetic field strength. The last suggestion for the magnetic field to be arranged along the X-ray feature, is also supported by the measurements of the magnetic field projected to out two-dimensional view of the sky by Milne (Fig. 1.8), where a strong field was found parallel to the X-ray feature and smaller field strengths in the outer sectors of the PWN.

6.5 Summarizing the Analysis Results on Vela X

A detailed view of the results extracted from 60 h observational data on the TeV PWN HESS J0835–455 is presented in the past Chapter. The results of the TeV spectral flux distribution and the extension measurement are included in the Tables 6.3 and 6.6. In this closing summary, the analysis results considering the R/R_{est} correction for different atmospheric transmissibility (Eqn. 4.9) are preferred. A couple of particular questions concerning the characteristics of the Vela X in the TeV range has been listed in Section 1.4, which will be picked up in the following.

Extension of the Vela X nebula TeV emission was found in the region of the radio PWN. This extends definitely the former association with the X-rays emission region. The extended emission is supported by the radial profile and the event counts in a ring with the radii 0.8° to 1.2° around the flux centroid were presented. An azimuthal profile of the ring shows no outstanding variations in the TeV flux.

Nature of the jet The fact that the TeV nebula is as extended as the radio nebula implies, that TeV emission is not restricted to the "Cocoon" region around the jet-like X-ray feature. On the other hand, evidences for a TeV counterpart of the feature were presented. A possible explanation for the nature of feature is a strong magnetic field along a cylinder with a length of about 1° and a width (in TeV) in the order of the H.E.S.S. PSF. The magnetic field confines the lepton plasma perpendicular to the field orientation and causes synchrotron emission, so that both the TeV and the X-ray flux are accounted for.

TeV spectrum of Vela X The differential photon spectrum exhibits a clear power law with an exponential cutoff. Such a spectral shape is the typical signature of TeV γ-rays generated in Inverse Compton scattering. No variations of the spectrum were

found. In particular, the ring extension emits a flux shape indistinguishable from that of the inner test region of Vela X. The final parametrization (Eqn. 5.17) for the spectral shape yields an index of $\gamma = 1.33 \pm 0.07$ and a cutoff energy of $E_{cut} = (12.0 \pm 1.4)$ TeV. This parametrization is consistent with the shape given for the inner test region by the H.E.S.S. collaboration in 2006.

Additional spectral component above 50 TeV The flux estimate from 50.0 TeV to 66.7 TeV seems to exceed the cutoff power law, although this excess is not significant. The case for an additional spectral feature seems not to be justified. No γ-rays flux was found above 66.7 TeV.

Energy-dependent morphology A search for a TeV γ-rays emitting plasma component directly next to the pulsar that recently was accelerated in the pulsar wind termination shock did not show any hints for such a component. It was argued before, that a harden of the spectrum in the region next to the pulsar cannot be resolved with the H.E.S.S. data.

The main and robust new result of this work is the firm detection of emission form the ring extension. No spectral variations either in the ring extension nor in the pulsar's surroundings were found and the spectral flux shape follows a power law with exponential cutoff. That is, a leptonic nebula plasma as origin of the TeV γ-rays is strongly supported, with the γ-rays being generated in IC scattering on the CMB (see Sec. 1.3.3).

Chapter 7

Conclusions

In this work, the standard analysis – the so-called Hillas analysis – was applied to observational TeV γ-rays data taken with the H.E.S.S. Imaging Atmospheric Cherenkov Telescope (IACT) array on the pulsar wind nebula (PWN) Vela X (in TeV HESS J0835–455). For the extraction of the γ-ray signal an assumption of the background level is needed, therefor the OnOff background model is applied to the Vela X data. The OnOff model uses observations without any TeV γ-rays sources in the field of view, which are taken under similar conditions are selected as background data. No planned ("dedicated") background observations have been taken for the Vela X observation campaigns. For this reason, the background data were selected from the H.E.S.S. archival data.

A detailed study of the characteristics of the background was performed to allow a reliable estimation of systematic errors of the OnOff background model. The well-known dependencies of the background rates on the angle between the observation direction of the telescopes and the zenith angle has been quantified. Further more, background dependencies on the azimuth angle of the observation direction, on the optical efficiency of the telescopes, on the mean number of broken pixels in the cameras and on the mean camera temperature were established with a relative accuracy of a few percent. Therefor the entire H.E.S.S. observational data of the last six years were used. Surprisingly, no dependency of the background rate on the night sky background light were found. This result can be important, in further investigations of night sky bright fields of views like the region around the galactic center. In this thesis, it is shown for the "OnOff"-model, that apart from the zenith angle and parameters describing the atmospheric conditions, no improvement of the estimated background rates could be achieved, if the mentioned background dependencies (on the azimuth angle, broken pixels and camera temperature) are considered for the implementation of the γ-rays analysis. As the atmosphere is part of the IACT detection process, variations (optical density and refraction) in the atmosphere will influence the properties of the detected γ-rays as well as the characteristics of the background. A new technique (R/R_{est} correction) using the stereoscopic hardware trigger rate of the IACT array (without applying any selection cuts to separate γ-rays from background events) is proposed to counterbalance misestimations of the background rate due

to variations of the atmosphere between the Vela X data observed in the summer term and the background data observed during the remaining year. As a second approach, a traceable selection algorithm to find background runs for the OnOff model using the hardware trigger rate and thus a parameter reflecting the atmospheric conditions as selection criterion was presented. Both methods have been tested on darkfields without any known TeV γ-rays sources. Relative uncertainties in the background rate of the accumulated data (20 – 100 h observation time per darkfield) were reduced by both techniques from 20 % to 5 %.

The analysis of the H.E.S.S. data on Vela X was performed with the OnOff background model and the R/R_{est} correction. Thereby, the emission from the ring extension and the R/R_{est} correction were cross-checked by a further approach using the more common reflected background model. For this purpose, additional observations which permit to apply the reflected background model were performed in the scope of this work. Overall, the results correspond to the results published by the H.E.S.S. collaboration in 2006 and based on one fourth of the recent data set. In contrast to the former interpretation of 2006 regarding the spatial extension of Vela X, the TeV PWN can now be associated with the $3^\circ \times 2^\circ$ radio nebula. For the spectral analysis, the H.E.S.S. collaboration suggested an inner integration region with a radius 0.8°. For the first time, TeV γ-rays emission was found in a ring extension with radii between 0.8° and 1.2° around the inner test region. The spectral shape of the TeV photon flux from Vela X follows an outstandingly hard power law with an exponential cutoff. No spectral variations were found within Vela X, in particular no detectable variations between the inner test and ring region.

The most common models for PWNe predict that the nebula plasma consists of leptons (more specific: electrons and positrons). The plasma particles are accelerated at a termination shock of a wind conducting energy away from the central pulsar. Within the nebula, the particles accelerated to the highest energies are cooled down faster than slower particles. Explaining the TeV flux with Inverse Compton upscattering of cosmic microwave photons on the lepton population, the exponential cutoff spectrum of the detected γ-rays flux can be explained. The absence of spectral variation implies that the plasma is dominated by the accumulation of ("relic") particles over several thousand years instead of the ongoing injection of new plasma by the pulsar wind. It was suggested for a futurity approach that the TeV flux generated in Inverse Compton scattering can be used as tracer for the density of the plasma. The X-rays flux arises as synchrotron emission and is proportional to the square of the magnetic field strength and plasma density, so that the morphology of the magnetic field can be determined. The modeling of the full set of Vela X observations should connect to the recent results of this work. As an example of a pulsar wind nebula driven by a middle-aged pulsar, Vela X can contribute to a general model of the evolution of pulsar wind nebulae.

Schlussfolgerung

Die vorliegende Arbeit beschäftigt sich mit der Datenanalyse von TeV-Gammastrahlungsbeobachtungen des Pulsarwindnebels Vela X (als H.E.S.S.-Quelle: HESS J0835–455), die mit dem H.E.S.S. Experiment aufgenommen wurden. Die Daten wurden mit der Standardanalyse, der sogenannten Hillasanalyse durchgeführt. Aus diesem Grund ist eine Abschätzung der Untergrundrate nötig, wobei in dieser Arbeit das "OnOff"-Untergrundmodell verwendet wird. Die Rekonstruktionstechnik weist eine hohe Rate an Untergrundereignissen auf, welche durch das "OnOff"-Untergrundmodel abgeschätzt wird. Für das "OnOff"-Modell werden Daten mit vergleichbaren Beobachtungsbedingungen ohne bekannte TeV-Gammastrahlungsquelle als Untergrunddaten verwendet. Während der Vela X Beobachtungskampagnen wurde der Untergrund nicht mit zeitnahen ("dedizierten") Beobachtungen vermessen, so dass die Untergrunddaten dem H.E.S.S. Datenarchiv entnommen sind.

Eine detaillierte Studien der Eigenschaften von Untergrundereignissen wurde durchgeführt, um die systematischen Unsicherheiten des "OnOff"-Untergrundmodells verlässlich abschätzen zu können. Die qualitativ bekannte Abhängigkeit der Untergrundrate vom Winkel zwischen dem Zenith und der Beobachtungsrichtung der Teleskope wurde quantifiziert. Desweiteren wurden entsprechende Abhängigkeiten vom Azimuthwinkel der Beobachtungsrichtung, der optischen Effizienz der Teleskope, der mittleren Anzahl defekter Pixel in den Teleskop-Kameras und der mittleren Temperatur in den Kameras mit einer relativen Genauigkeit von wenigen Prozent nachgewiesen, wozu die gesamten H.E.S.S.-Beobachtungsdaten der letzten sechs Jahre verwendet wurden. Entgegen vorheriger Vermutungen konnte keine Abhängigkeit der Untergrundrate vom Nachthimmelsleuchten festgestellt werden. Diese fehlende Abhängigkeit kann bei zukünfigen Untersuchungen von Himmelsregionen mit starkem Nachthimmelsleuchten von Bedeutung sein, wie beispielsweise für die Region um das galaktische Zentrum. Die Einbindung der gefundenen Abhängigkeiten der Untergrundrate in das "OnOff"-Modell führt, abgesehen von der Zenithwinkelabhängigkeit und der Abhängigkeit von Parametern, welche die atmosphärischen Bedingungen beschreiben, zu keinen feststellbaren Verbesserungen der Untergrundabschätzung. Die Atmosphäre ist Bestandteil des Detektionsprozesses der Tscherenkow-Teleskope, so dass Variationen in der Atmosphäre (optische Dichte und Refraktion) die Eigenschaften der detektierten Gammaereignisse ebenso wie der Untergrundereignisse beeinflussen. Eine neue Methode (R/R_{est} Verhältnis) unter Benutzung der kombinierten Hardware-Triggerrate der vier Teleskope (ohne zusätzliche Schnitte zur Trennung von Gamma- und Untergrundereignissen) wird vorgeschlagen, um diese Fehleinschätzungen der Untergrundrate zwischen den Beobachtung von Vela X, die im Sommer stattfinden müssen und den Beobachtungen die zur Untergrundabschätzung verwendet werden, auszugleichen. Als Alternative wird ein Auswahlalgorithmus vorgestellt, der die "OnOff"-Untergrunddaten anhand der Triggerraten und damit vergleichbaren atmosphärischen Bedingungen auswählt. Beide Methoden sind an Dunkelfeldern (darkfield, blank sky) ohne enthaltene TeV-Gammastrahlungsquelle getestet worden. Relative Unsicherheiten in den Untergrundrate reduzieren sich bei der Anwendung der beiden Methoden in den Dunkelfeldern (20 – 100 h Beobachtungszeit pro

Dunkelfeld) von 20 % auf 5 %.

Die H.E.S.S.-Datenanalyse für Vela X wurde mit dem "OnOff"-Modell und der R/R_{est} Korrekturmethode durchgeführt. Zusätzliche Beobachtungen von Vela X, die den gespiegelten Untergrund erlauben, wurden im Rahmen dieser Arbeit durchgeführt. In den wichtigsten Punkten entsprechen die Analyseergebnisse denen, die 2006 von der H.E.S.S. Kollaboration auf der Grundlage eines Viertels des hier vergestellten Datensatzes veröffentlicht wurden. Das Spektrum des TeV-Photonenfluss von Vela X folgt einen aussergewöhnlich hartem Potenzgesetz mit einem exponentiellen Abbruch. Im Gegensatz zur Interpretation aus der 2006 Publikation wird eine Ausdehnung der TeV-Gammastrahlungsquelle in der gleichen Größenordnung festgestellt, wie in Radiobeobachtungen ($3° \times 2°$) gemessen wurde. Es konnte erstmals TeV-Gammastrahlung aus einer Ringregion (zwischen den Raumwinkelradien zwischen 0.8° und 1.2°) um die bisherige innere Integrationsregion (Raumwinkelradius bis 0.8°) nachgewiesen werden. Diese vergrößerte Intergrationsregion und die R/R_{est} Korrekturmethode konnte mit einer zweiten Methode zur Abschätzung der Untergrundrate, dem gespiegelten Untergrund ("reflected background"), bestätigt werden. Spektrale Variationen der Gammastrahlung für verschiedene Integrationsregionen innerhalb von Vela X konnten nicht festgestellt werden. Insbesondere sind keine Unterschiede zwischen der inneren Testregion und der Ringerweiterung gefunden worden.

Die gängigsten Modelle für Pulsarwindnebel gehen davon, dass das Nebelplasma aus Leptonen (genauer: Elektronen und Positronen) besteht, wobei die Plasmateilchen in einem "Termination Shock" des Pulsarwindes, der Energie vom zentralen Pulsar abtransportiert, beschleunigt und in den Nebel injiziert werden. Berücksichtigt man, dass hochenergetische Teilchen im Nebel schneller kühlen als langsame Teilchen und dass TeV-Photonen durch Inverse Compton-Streuung der Plasmaleptonen an Photonen der kosmischen Mikrowellenstrahlung hervorgebracht werden, kann das beobachtete Potenzgesetze mit exponentiellen Abbruch erklärt werden. Aus dem Fehlen von Variationen des Spektrums innerhalb des Nebel kann geschlossen werden, dass das Plasma durch alte, über mehrere tausend Jahre akkumulierte Teilchen dominiert wird. Die fortlaufende Injektion neuen Plasmas durch den Pulsar Wind spielt für die Form des gemessenen Spektrums keine Rolle. Durch die vorgeschlagene Inverse Compton-Streuung kann in zuküftigen Untersuchung die räumliche Verteilung der TeV-Strahlung als Messgröße für die Dichte das Nebelplasma genutzt werden. Der Röntgenfluss entsteht als Synchrotron-Emission und ist proportial zur Plasmadichte und zum Quadrat der magnetischen Feldstärke, so dass das die räumliche Verteilung des magnetischen Feldes bestimmt werden kann. Vela X kann als Beispiel für einen Pulsarwindnebel mittleren Alters zu einem allgemeinen Modell der Evolution von Pulsarwindnebel beitragen.

Attachments

Vela X Run List

The archival run numbers of the 131 H.E.S.S. observation runs on Vela X are listed here. The run numbers in the brackets are the selected background runs.

18417 (20715), 18536 (20915), 18569 (20758), 18575 (20713), 18577 (20711), 18601 (20339), 18694 (20736), 19133 (21995), 19134 (19747), 19172 (20714), 19174 (20916), 19175 (20515), 19199 (20275), 19917 (21831), 20046 (21834), 20047 (20281), 20101 (21818), 20102 (20937), 20103 (20918), 20104 (19274), 20123 (20738), 20126 (20735), 20127 (21820), 20128 (20917), 20142 (20712), 20163 (21851), 23821 (23647), 24142 (26846), 24890 (23639), 24893 (27043), 24925 (23085), 24948 (23617), 24972 (25392), 25002 (23061), 25024 (27075), 25317 (23636), 25318 (35900), 25337 (22961), 25338 (28831), 25387 (26877), 25388 (23141), 36688 (36805), 36689 (33455), 36702 (27924), 36703 (29042), 36704 (29176), 36705 (48976), 36706 (28095), 36727 (36779), 36728 (32405), 36730 (36605), 36731 (40130), 36732 (33514), 36733 (28978), 36748 (32972), 36749 (36652), 36750 (45918), 36751 (33360), 36752 (40319), 36753 (28989), 36754 (32971), 36773 (33104), 36774 (27858), 36775 (29096), 36776 (32408), 37126 (33100), 37147 (38338), 37148 (33129), 37149 (36620), 37160 (35955), 37161 (34938), 37164 (32997), 37165 (44145), 37183 (36698), 37184 (29279), 37185 (46668), 37186 (46667), 37187 (32493), 37210 (36666), 37211 (36634), 37212 (38220), 37213 (38132), 37214 (44846), 37239 (31753), 37240 (36724), 37241 (36087), 37242 (38310), 37243 (28967), 37244 (45154), 37245 (27014), 37266 (33099), 37291 (36697), 43812 (46610), 43833 (46457), 43834 (48291), 43957 (55400), 44036 (46649), 44149 (47924), 44150 (46456), 44151 (51580), 49320 (53909), 49560 (47123), 49580 (52470), 49581 (54035), 49582 (43652), 49601 (46602), 49603 (40937), 49626 (46243), 49630 (47983), 49632 (47922), 49672 (52055), 49673 (50326), 49695 (50132), 49696 (42282), 49697 (52576), 49698 (47982), 49720 (42304), 49724 (51612), 49739 (51446), 49776 (51388), 49777 (52721), 49795 (54054), 49812 (46994), 49813 (47923), 49814 (51550), 49815 (54620), 49831 (52405), 49850 (54745), 50339 (46515), 50341 (50070), 50353 (46702)

Bibliography

[1] Abdo, A. A., Ackermann, M., Ajello, M., et al. 2010, ApJ, 713, 146

[2] Achterberg, A., Gallant, Y. A., Kirk, J. G., & Guthmann, A. W. 2001, MNRAS, 328, 393

[3] Aharonian, F., Akhperjanian, A. G., Aye, K., et al. 2004, A&A, 425, L13

[4] Aharonian, F., Akhperjanian, A. G., Aye, K., et al. 2005, A&A, 430, 865

[5] Aharonian, F., Akhperjanian, A. G., Aye, K., et al. 2004, Astroparticle Physics, 22, 109

[6] Aharonian, F., Akhperjanian, A. G., Bazer-Bachi, A. R., et al. 2006, A&A, 448, L43

[7] Aharonian, F., Akhperjanian, A. G., Bazer-Bachi, A. R., et al. 2006, A&A, 457, 899

[8] Aharonian, F., Akhperjanian, A. G., Bazer-Bachi, A. R., et al. 2006, A&A, 449, 223

[9] Aharonian, F., Akhperjanian, A. G., Bazer-Bachi, A. R., et al. 2007, A&A, 466, 543

[10] Aharonian, F., Akhperjanian, A. G., Bazer-Bachi, A. R., et al. 2007, ApJ, 661, 236

[11] Aharonian, F., Akhperjanian, A. G., Bazer-Bachi, A. R., et al. 2006, A&A, 460, 365

[12] Aharonian, F. A., Hofmann, W., Konopelko, A. K., & Völk, H. J. 1997, Astroparticle Physics, 6, 343

[13] Akerlof, C. W., Cawley, M. F., Chantell, M., et al. 1991, ApJ, 377, L97

[14] Albert, J., Aliu, E., Anderhub, H., et al. 2008, ApJ, 674, 1037

[15] Alvarez, H., Aparici, J., May, J., & Reich, P. 2001, A&A, 372, 636

[16] Arons, J. 2002, in Astronomical Society of the Pacific Conference Series, Vol. 271, Neutron Stars in Supernova Remnants, ed. P. O. Slane & B. M. Gaensler, 71–+

[17] Aschenbach, B. 1998, Nature, 396, 141

[18] Aschenbach, B., Egger, R., & Trümper, J. 1995, Nature, 373, 587

[19] Bell, A. R. 1978, MNRAS, 182, 147

[20] Berge, D. 2006, PhD thesis, Combined Faculties for the Natural Sciences and for Mathematics of the Ruperto-Carola University of Heidelberg

[21] Berge, D., Funk, S., & Hinton, J. 2007, A&A, 466, 1219

[22] Bernlöhr, K. 2000, Astroparticle Physics, 12, 255

[23] Bernlöhr, K. 2001, H.E.S.S. internal note

[24] Bernlöhr, K. 2005, H.E.S.S. internal note

[25] Bernlöhr, K., Carrol, O., Cornils, R., et al. 2003, Astroparticle Physics, 20, 111

[26] Bethe, H. & Heitler, W. 1934, Royal Society of London Proceedings Series A, 146, 83

[27] Blondin, J. M., Chevalier, R. A., & Frierson, D. M. 2001, ApJ, 563, 806

[28] Blumenthal, G. R. & Gould, R. J. 1970, Reviews of Modern Physics, 42, 237

[29] Bock, D., Turtle, A. J., & Green, A. J. 1998, AJ, 116, 1886

[30] Bolz, O. 2004, PhD thesis, Ruprecht-Karls Universität Heidelberg

[31] Bulian, N., Daum, A., Hermann, G., et al. 1998, Astroparticle Physics, 8, 223

[32] Burke, D. L. 1987, Neutrino Counting in e^+e^-1 Annihilation, Slac-Pub-4284

[33] Caraveo, P. A., De Luca, A., Mignani, R. P., & Bignami, G. F. 2001, ApJ, 561, 930

[34] Collins, I. G. W., Claspy, W. P., & Martin, J. C. 1999, PASP, 111, 871

[35] Cornils, R., Gillessen, S., Jung, I., et al. 2003, Astroparticle Physics, 20, 129

[36] Davies, J. M. & Cotton, E. S. 1957, Journal of Solar Energy Science and Engineering, 1, 16

[37] de Jager, O. C., Harding, A. K., Sreekumar, P., & Strickman, M. 1996, A&AS, 120, C441+

[38] de Jager, O. C., Slane, P. O., & LaMassa, S. 2008, ApJ, 689, L125

[39] Dodson, R., Legge, D., Reynolds, J. E., & McCulloch, P. M. 2003, ApJ, 596, 1137

[40] Dorner, D., Nilsson, K., & Bretz, T. 2009, A&A, 493, 721

[41] Dubner, G. M., Green, A. J., Goss, W. M., Bock, D., & Giacani, E. 1998, AJ, 116, 813

[42] Dubois, F. 2009, PhD thesis, Université de Savoie

[43] Dubois, F., Glück, B., de Jager, O. C., et al. 2009, in International Cosmic Ray Conference, Online Proceedings, http://icrc2009.uni.lodz.pl/proc/pdf/icrc1056.pdf

[44] Duncan, A. R., Haynes, R. F., Jones, K. L., & Stewart, R. T. 1997, MNRAS, 291, 279

[45] Duncan, A. R., Stewart, R. T., Haynes, R. F., & Jones, K. L. 1995, MNRAS, 277, 36

[46] Ferreira, S. E. S. & de Jager, O. C. 2008, A&A, 478, 17

[47] Frail, D. A., Bietenholz, M. F., Markwardt, C. B., & Oegelman, H. 1997, ApJ, 475, 224

[48] Funk, S. 2005, PhD thesis, Naturwissenschaftlich-Mathematische Gesamtfakultät der Ruprecht-Karls Universität of Heidelberg

[49] Funk, S., Hermann, G., Hinton, J., et al. 2004, Astroparticle Physics, 22, 285

[50] Gaensler, B. M. & Slane, P. O. 2006, ARA&A, 44, 17

[51] Gelfand, J. D., Slane, P. O., & Zhang, W. 2009, ApJ, 703, 2051

[52] Gvaramadze, V. 1999, A&A, 352, 712

[53] Hales, A. S., Casassus, S., Alvarez, H., et al. 2004, ApJ, 613, 977

[54] Hauser, M., Möllenhoff, C., Pühlhofer, G., et al. 2004, Astronomische Nachrichten, 325, 659

[55] Hauser, M., Wagner, S. J., & Hagen, H. 2008, in American Institute of Physics Conference Series, Vol. 1085, American Institute of Physics Conference Series, ed. F. A. Aharonian, W. Hofmann, & F. Rieger, 696–697

[56] Heck, D., Knapp, J., Capdevielle, J. N., Schatz, G., & Thouw, T. 1998, CORSIKA: A Monte Carlo Code to Simulate Extensive Air Showers., Wissenschaftliche Berichte 6019, Forschungszentrum Karlsruhe

[57] HEGRA Collaboration, Konopelko, A., Hemberger, M., et al. 1999, Astroparticle Physics, 10, 275

[58] Helfand, D. J., Gotthelf, E. V., & Halpern, J. P. 2001, ApJ, 556, 380

[59] Hermsen, W. 2010, personal communication

[60] Hillas, A. M. 1985, in International Cosmic Ray Conference, Vol. 3, International Cosmic Ray Conference, ed. F. C. Jones, 445–448

[61] Hinton, J. A. & Hofmann, W. 2009, ARA&A, 47, 523

[62] Hofmann, W., Jung, I., Konopelko, A., et al. 1999, Astroparticle Physics, 12, 135

[63] Holder, J. 2008, in American Institute of Physics Conference Series, Vol. 1085, American Institute of Physics Conference Series, ed. F. A. Aharonian, W. Hofmann, & F. Rieger, 742–745

[64] Holder, J., Atkins, R. W., Badran, H. M., et al. 2006, Astroparticle Physics, 25, 391

[65] Hoppe, S. 2008, PhD thesis, Combined Faculties for the Natural Sciences and for Mathematics of the Ruperto-Carola University of Heidelberg

[66] Horns, D., Aharonian, F., Hoffmann, A., & Santangelo, A. 2008, in The Multi-Messenger Approach to High-Energy Gamma-Ray Sources, ed. J. M. Paredes, O. Reimer, & D. F. Torres (Springer Netherlands), 189–195, 10.1007/978-1-4020-6118-9_29

[67] James, F. 1981, Determining the statistical Significance of experimental Results., Tech. Rep. DD/81/02 and CERN Report 81-03, CERN

[68] Jun, B. 1998, ApJ, 499, 282

[69] Jun, B., Norman, M. L., & Stone, J. M. 1995, ApJ, 453, 332

[70] Kellogg, E., Tananbaum, H., Harnden, J. F. R., et al. 1973, ApJ, 183, 935

[71] Koch, A. & Kohnle, A. 2001, H.E.S.S. internal note

[72] Kopper, S. J. 2009, Systematische Studien zur Datenqualität bei H.E.S.S., Diploma Thesis, Erlangen Centre for Astroparticle Physics, Friedrich-Alexander-Universität Erlangen-Nürnberg

[73] Krawczynski, H. 2000, H.E.S.S. internal note

[74] Krawczynski, H., Carter-Lewis, D. A., Duke, C., et al. 2006, Astroparticle Physics, 25, 380

[75] Krawczynski, H., Hofmann, W., Korgel, W., Panter, M., & Rowell, G. 2000, H.E.S.S. internal note

[76] Kuiper, L., Hermsen, W., Cusumano, G., et al. 2001, A&A, 378, 918

[77] Lafferty, G. D. & Wyatt, T. R. 1995, Nuclear Instruments and Methods in Physics Research A, 355, 541

[78] Le Gallou, R., Nolan, S. J., Masterson, C., & Spangler, D. 2005, H.E.S.S. internal note

[79] Lebohec, S. & Holder, J. 2003, Astroparticle Physics, 19, 221

[80] Li, T. & Ma, Y. 1983, ApJ, 272, 317

[81] Longair, M. S. 1992, High enery astrophysics, Vol. 1, Particles, photons and their detection, 2nd edn. (Cambridge University Press)

[82] Longair, M. S. 1994, High enery astrophysics, Vol. 2, Stars, the Galaxy and the interstellar medium, 2nd edn. (Cambridge University Press)

[83] Lyne, A. G. & Lorimer, D. R. 1994, Nature, 369, 127

[84] Lyne, A. G., Pritchard, R. S., Graham-Smith, F., & Camilo, F. 1996, Nature, 381, 497

[85] Lyne, A. G., Pritchard, R. S., & Smith, F. G. 1988, MNRAS, 233, 667

[86] Mangano, V., Massaro, E., Bocchino, F., Mineo, T., & Cusumano, G. 2005, A&A, 436, 917

[87] Markwardt, C. B. & Ögelman, H. 1995, Nature, 375, 40

[88] Markwardt, C. B. & "Ogelman, H. B. 1997, ApJ, 480, L13+

[89] Matthews, J. 2005, Astroparticle Physics, 22, 387

[90] McKee, C. F. 1974, ApJ, 188, 335

[91] Milne, D. K. 1995, MNRAS, 277, 1435

[92] Nakamura, K., Hagiwara, K., Hikasa, K., et al. 2010, J. Phys. G, 37

[93] Nolan, S. J., Pühlhofer, G., & Rulten, C. B. 2010, Astroparticle Physics, 34, 304

[94] Pacini, F. 1968, Nature, 219, 145

[95] Pacini, F. & Salvati, M. 1973, ApJ, 186, 249

[96] Pellizzoni, A., Trois, A., Tavani, M., et al. 2010, Science, 327, 663

[97] Reynolds, S. P. & Chevalier, R. A. 1984, ApJ, 278, 630

[98] Rishbeth, H. 1958, Australian Journal of Physics, 11, 550

[99] Rowell, G., Krawczynski, H., Hofmann, W., Korgel, W., & Panter, M. 2000, H.E.S.S. internal note

[100] Spitkovsky, A. 2008, ApJ, 682, L5

[101] Tanimori, T., Sakurazawa, K., Dazeley, S. A., et al. 1998, ApJ, 492, L33+

[102] Weekes, T. C., Cawley, M. F., Fegan, D. J., et al. 1989, ApJ, 342, 379

[103] Weisskopf, M. C., Brinkman, B., Canizares, C., et al. 2002, PASP, 114, 1

[104] Woltjer, L. 1972, ARA&A, 10, 129

[105] Yoshikoshi, T., Mori, M., Edwards, P. G., et al. 2009, ApJ, 702, 631

[106] Zhang, L., Chen, S. B., & Fang, J. 2008, ApJ, 676, 1210